Direct numerical simulation of an aerofoil at high angle of attack and its control

Marco Edoardo Rosti

PhD in Aeronautical Engineering

City, University of London

School of Mathematics, Computer Science & Engineering

Department of Mechanical Engineering & Aeronautics

September 2016

Abstract

Detailed analysis of the flow around a NACA0020 aerofoil at moderate low chord Reynolds number ($Re_c = 2\times10^4$) in completely stalled conditions has been carried out by means of Direct Numerical Simulations. The stalled condition is either a steady configuration at a fixed angle of attack ($\alpha = 20^o$) or it is reached via a ramp-up manoeuvre, increasing the angle of attack from 0^o to 20^o. Concerning this last case, new insights on the vorticity dynamics leading to the lift overshoot, lift crisis and the damped oscillatory cycle that gradually matches the steady condition, are discussed using a number of post-processing techniques. These include a detailed analysis of the flow ensemble average statistics and coherent structures identification that has been carried out using the $\mathcal{Q}$-criterion and the Finite-Time Lyapunov Exponent technique.

Based on the fundamental knowledge achieved in studying the static and the dynamic stall, we introduced a biomimetic passive control technique to mitigate the aerodynamic performance degradation typical of such flow conditions. In particular, the envisaged control technique has been inspired by the dorsal feathers that are used by almost all birds to adapt their wing characteristics to delay stall or to moderate its adverse effects (e.g., during landing or sudden increase in angle of attack due to gusts). Some of the feathers are believed to pop up as a consequence of flow separation and to interact with the flow producing beneficial modifications of the unsteady vorticity field. The adoption of self adaptive flaplets in aircrafts, inspired by birds feathers, requires the understanding of the physical mechanisms leading to their aerodynamic benefits and the determination of the characteristics of optimal flaps including their size, positioning and ideal fabrication material.

In this framework, we have used numerical simulation to study the effects of this passive control technique in both steady and dynamic stall. In particular, for the static case, we have defined an optimal condition as the one that delivers the highest lift coefficient C_L, preserving or improving the aerodynamic efficiency $E = C_L/C_D$. To achieve a condition close to optimality we started by considering a simplified scenario, to determine the main characteristics of the flap (i.e., variations of its length, position and natural frequency). Later on, a detailed direct numerical simulation analysis is used to understand the origin of the aerodynamic benefits introduced by the pop-up of the optimal flaplet. It is found that an op-

timal flap can deliver a mean lift increase of about 20% on a NACA0020 aerofoil at an incidence of 20^o degrees. The analysis of direct numerical simulation data of the flow field around the aerofoil equipped with the optimal flap allowed to elucidate the main mechanism that promotes the aerodynamic improvements. In particular, it is found that the flaplet movement, induced by the transit of a large recirculation bubble on the aerofoil suction side, displaces the trailing edge vortices further downstream, away from the wing. The downstream displacement of the trailing edge generated vortices, limits the downforce generated by those vortices also regularising the shedding cycle that appears to be much more organised when the flaplet is activated.

A similar study has also been carried out for the dynamic case. We have analysed the effects produced by the presence of an elastically mounted flap on the transient behaviour of the flow fields. For a specific ramp-up manoeuvre characterised by a reduced frequency slower the shedding one, it is found that it is possible to design flaps that limit the severity of the dynamic stall breakdown. In particular, it is possible to increase the value of the lift overshoot and to smooth its abrupt decay in time. A detailed analysis on the modification of the unsteady vorticity field due to the flap-flow interaction during the ramp-up motion is also provided to explain the physical mechanism that lead to more benign aerodynamic response.

Key Words

Direct Numerical Simulation - Aerodynamic - Static Stall - Dynamic Stall - Passive Control - Biomimetic - Hairy Flap

Contents

Chapter 1

Introduction

Stall is a phenomenon that arises on aerofoils at high angle of attack and is responsible of a dramatic decrease in their aerodynamic performance (i.e., decrease of the lift and increase of the drag). This degradation is mainly due to the flow separation on the wing surface characterised by the appearance of large recirculating regions. A stalled condition can be obtained either by keeping the angle of attack fixed beyond a certain value (static stall), or by increasing its value in time beyond the value of the static stall angle (dynamic stall). Researchers have long been looking for new ways of controlling the flow separation on aerofoils at high angle of attack. Recently, particular attention has been given to devices inspired by nature. In particular, it has been observed that birds can overcome certain flight critical conditions, by popping up some of their feathers when flow separation starts to develop on the upper side of their wing [10, 12, 21] (see Figure (1.1)). It is believed that the feathers lift-up limits backflow also preventing an abrupt breakdown of the lift force typical of dynamic stall. With the aim of reproducing this effect, Schatz et al. [84] have shown that a self-activated spanwise flap positioned near the trailing edge of an aerofoil can enhance lift by more than 10% (at a Reynolds number of $Re_c = U_\infty c/\nu = 1 - 2 \times 10^6$). In a similar experiment, Schluter [85] has also demonstrated that lift-breakdown is less severe when such flap is used. Wang and Schluter [95] have extended the analysis to a three dimensional wings basically confirming the aforementioned effects. Differently from other authors, Kernstine et al. [50] found that the increase in lift can also be achieved with a flap mounted in the first half of the aerofoil, closer to the leading edge. Venkataraman and Bottaro [92] performed a numerical study of the effect of hairy coatings on an NACA0012 aerofoil (aircraft wings developed by the National Advisory Committee for Aeronautics) at low Reynolds number $Re_c = 1100$ and high angle of attack $\alpha = 70^o$, and found a set of coating parameters able to deliver an increase in lift ($\simeq 9\%$). Finally, the effectiveness of fixed versus free-moving flaps has been studied by Johnston and Gopalarathnam [46]. They found that also fixed flaps can deliver an improvement in both lift and drag at an angle of attack. However, the improvements diminish when the flaps

FIGURE 1.1: (a) Frontal and (b) side view of a falcon with popped-up feathers (taken from the measurement campaign documented in Ponitz et al. [76]).

are used for higher incidence values.

More recently, Bruecker and Weidner [17] used hairy flaps (i.e., flaps with very small thickness) to control the dynamic stall of a wing at moderate Reynolds number ($Re_c = 77000$), observing a delay of the dynamic stall. The authors claim that this delay is achieved by the action of the flap that reduces the backflow, and is beneficial for the shear layer roll-up process. They also suggest that the onset of non-linear growth in the shear layer is delayed by a mode-locking of the fundamental flow instability mode with the motion of the flaps.

Beneficial aerodynamic performance were also obtained using flexible covert mounted on a circular cylinder. Specifically, Favier et al. [32] conducted a numerical investigation into a hairy coating applied to a two-dimensional circular cylinder at a Reynolds number of $Re_D = 200$. Their results show that the coating through the interaction with the flow is able to reduce both the mean drag (by $\simeq 15\%$) and the lift fluctuations (by $\simeq 44\%$). Similar results were obtained at much higher Reynolds numbers in experiments involving a cylinder equipped with flexible flaps on its lee side (the flaps were not very different from the ones considered in the present study [56]). As final examples of the aerodynamic benefits that can be obtained exploiting the interaction between slender hairy appendages with a fluid flow, it is also worth mentioning the net lift force that can be generated by using a single passive filament hinged on the rear of a bluff body (the generated lift is a consequence the wake symmetry breaking [5]) and the modifications that flexible hairy coatings can induce in near-wall turbulence [16, 49].

1.1 Outline

The outline of the thesis is as follows. In Chapter (2) we present the numerical formulation, the baseline problem setup employed in this work, and the initial validation campaign. Chapter (3) covers the discussion of the results obtained when

considering the flow over a NACA0020 aerofoil at high angle of attack, firstly by discussing the fully-separated flow at a static angle of attack, and later on by analysing the flow during a ramp-up motion. In Chapter (4) we discuss how the flow over the aerofoil in a static stall condition can be modified by the presence of a flap elastically hinged on the suction side of the aerofoil. Initially, we will illustrate the results of a preliminary two-dimensional parametric campaign that we have carried out to roughly identify the optimal configuration and location of the flaplet. Then, the results and the interpretation of the flow fields generated by a full direct numerical simulations are offered also by comparing the characteristics of the fields obtained with and without flaplet. Chapter (5) contains the discussion of the effect of the flaplet during an unsteady ramp-up manoeuvre where different optimality conditions are specified. Finally, some conclusions will be drawn at the end of the thesis in Chapter (6).

The results presented in this thesis have been published or submitted to various archival journals and presented at international conferences.

- M. E. Rosti, M. Omidyeganeh, and A. Pinelli. *Direct numerical simulation of the flow around an aerofoil in ramp-up motion.* Physics of Fluids, 28(2), 2016;
- M. E. Rosti, L. Kamps, C. Bruecker, M. Omidyeganeh, and A. Pinelli. *The PELskin project - part V - Towards the control of the flow around aerofoils at high angle of attack using a self-activated deployable flap.* Meccanica, under review;
- M. E. Rosti, M. Omidyeganeh, and A. Pinelli. *Passive control of the flow around an aerofoil using a flexible, self adaptive flaplet.* Journal of Fluid Mechanics, under review;
- M. E. Rosti, M. Omidyeganeh, and A. Pinelli. *Passive control of the flow around unsteady aerofoils using a self-activated deployable flap.* Journal of Turbulence, under review.

- M. E. Rosti, M. Omidyeganeh, and A. Pinelli. *Study of flow around NACA0020 aerofoil with hairy flaps during ramp-up motion.* EDRFCM, Cambridge, March 2015;
- A. Pinelli, M. Omidyeganeh, and M. E. Rosti. *Control of dynamic stall by elastically mounted flaps.* JJ70, Salamanca, September 2015;
- M. E. Rosti, M. Omidyeganeh, and A. Pinelli. *Investigation and control of dynamic stall of an aerofoil ramp up motion.* APS - DFD Meeting, Boston, November 2015;

- A. Pinelli, M. Omidyeganeh, and M. E. Rosti. *Flow manipulation based on passive and localised fluid structure interactions.* ETMM11, Palermo, September 2016 (invited talk);

- M. E. Rosti, M. Omidyeganeh, and A. Pinelli. *Passive control of an aerofoil with flexible flap.* EFMC11, Seville, September 2016.

Chapter 2

Methodology

In the present thesis, we will consider incompressible two or three-dimensional unsteady flow fields. In an inertial, Cartesian frame of reference the momentum and mass conservation equations for an incompressible flow read as

$$\frac{\partial u_i}{\partial t} + \frac{\partial u_i u_j}{\partial x_j} = -\frac{\partial p}{\partial x_i} + \frac{1}{Re}\frac{\partial^2 u_i}{\partial x_j \partial x_j} + f_i, \tag{2.1}$$

$$\frac{\partial u_i}{\partial x_i} = 0. \tag{2.2}$$

where u_i is the i-th velocity component, p is the pressure, f_i a volume force, and Re is the Reynolds number. In Equation (2.1) and Equation (2.2) the equations have been made non-dimensional by choosing a reference length and velocity scales, U^* and L^*, and introducing the corresponding Reynolds number $Re = \rho U^* L^*/\mu$, where ρ and μ are the density and dynamic viscosity of the fluid. The given equations are closed by defining associated boundary and initial conditions delivering a well posed problem.

2.1 Finite volume method

An approximate numerical solution of Equation (2.1) and Equation (2.2) is reached using the Finite Volume Method. An exhaustive treatment on this methodology can be found in the book by Ferziger and Peric [33]. Here for the sake of completeness we shall just give a basic introduction. The incompressible Navier-Stokes equations (Equation (2.1) and Equation (2.2)) are initially integrated over an arbitrary control volume V, obtaining their integral forms:

$$\frac{\partial}{\partial t}\int_V u_i \, dV + \int_S u_i u_j n_j \, dS = -\int_V \frac{\partial p}{\partial x_i} \, dV + \int_S \tau_{ij} n_j \, dS + \int_V f_i \, dV, \tag{2.3}$$

$$\int_S u_i n_i dS = 0. \tag{2.4}$$

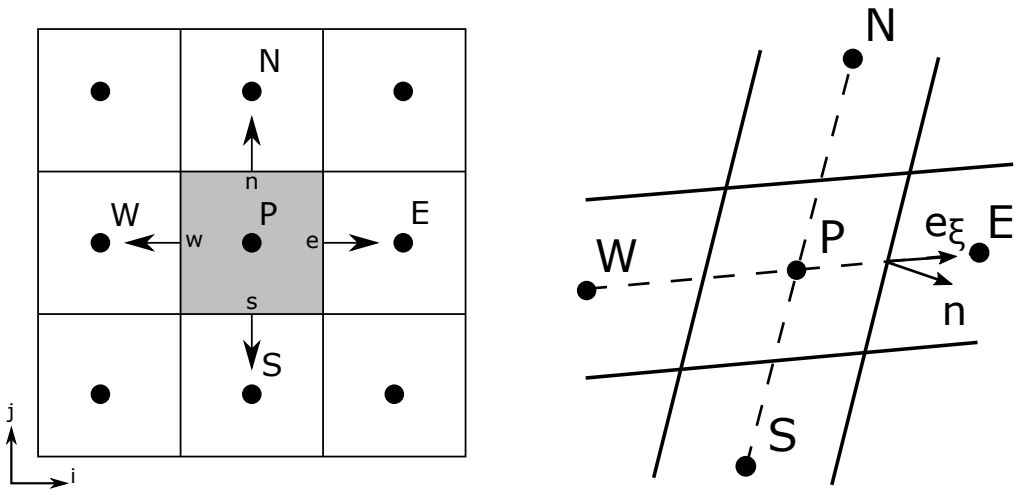

FIGURE 2.1: (a) A typical CV and the notation used. (b) A typical CV with a skewed grid.

Equation (2.3) refers to the i-th Cartesian component. In Equation (2.3) and Equation (2.4) S is the surface that bounds V, n_i is the i^{th} component of the outward normal vector to S, and τ_{ij} is the viscous stress tensor

$$\tau_{ij} = \frac{1}{Re}\left(\frac{\partial u_i}{\partial x_j} + \frac{\partial u_j}{\partial x_i}\right). \tag{2.5}$$

To obtain the previous equations we have used the Gauss theorem

$$\int_V \frac{\partial F_i}{\partial x_i}\, dV = \int_S F_i n_i\, dS \tag{2.6}$$

applied to a generic differentiable vector field F_i.

To obtain a numerical approximation to the solution of Equation (2.3) and Equation (2.4), the domain is subdivided into a finite number of contiguous, non-overlapping Control Volumes (CVs), and the conservation equations are applied to each CV, see Figure (2.1a). The method is conservative by construction, as long as the surface integrals are the same for the CVs sharing a boundary. At the centroid of each CV, we define a computational node where all the averages of the computational variables are (u_i and p) are formally assigned. Using this colocated approach, the number of coefficients and data to be computed and stored is minimized, and the programming is simplified. The colocated approach has also other significant advantages when dealing with complicated domains, or when the boundary conditions have discontinuities. However, this approach may lead to some difficulties with the pressure-velocity coupling and the occurrence of spurious oscillations in the pressure field (see Section (2.1.1)).

In order to numerically solve our equations, we have to introduce a numerical approximation for the surface and volume integrals. Since in $3D$ each cell has a cuboidal shape, the net flux through a CV boundary is the sum of the contributions over six faces

$$\int_S f dS = \sum_k \int_{S_k} f dS, \tag{2.7}$$

where f is any component of a flux vector in the direction normal to the face (e.g., the normal convective or viscous flux in the momentum equations, $\int_S u_i u_j n_j \, dS$ and $\int_S \tau_{ij} n_j \, dS$, respectively). Note that, for an incompressible fluid with constant viscosity, the viscous flux reduces to

$$\int_S \tau_{ij} n_j \, dS = \frac{1}{Re} \int_S \frac{\partial u_i}{\partial x_j} n_j dS. \tag{2.8}$$

The surface integral is approximated using the mid-point rule, leading to an approximation of second-order accuracy. In this quadrature, the integral is approximated as the product of the integrand at the cell-face center and the corresponding surface area. As an example the flux on the east face of a rectangular cell would reads as:

$$F_e = \int_{S_e} f dS \approx f_e S_e. \tag{2.9}$$

Equation (2.9) requires the values of the variables at the face centre. To obtain these values, we use a linear interpolation between the two nearest nodes, f_E and f_P. For example, at location e we have

$$f_e = f_E \lambda_e + f_P (1 - \lambda_e), \tag{2.10}$$

where the linear interpolation factor λ_e is defined as

$$\lambda_e = \frac{x_e - x_P}{x_E - x_P}. \tag{2.11}$$

This method is also second-order accurate and on a Cartesian mesh would correspond to the central-difference approximation of the first derivative in a finite difference framework. The assumption of a linear variation between points P and E, provides also a simple method to approximate the derivative,

$$\left(\frac{\partial f}{\partial x} \right)_e \approx \frac{f_E - f_P}{x_E - x_P}. \tag{2.12}$$

Some terms also require integration over a CV. To compute the integral up to second-order accuracy, the mid point rule is extended as

$$Q_P = \int_V q dV \approx q_P V_P. \tag{2.13}$$

Since all variables are available at the CV center, no interpolation is required.

We are now able to write the full spatial approximations of Equation (2.3) and Equation (2.4). The volume integrals, corresponding to the unsteady, pressure and forcing terms, can be easily computed applying Equation (2.13). The convective flux F^c is computed by assuming that the mass flux $\dot{m}$ is already known using the midpoint rule approximation

$$F_e^c = \int_{S_e} u\boldsymbol{u} \cdot \boldsymbol{n}\, dS \approx \dot{m}_e u_e, \tag{2.14}$$

here, again for the sake of simplicity, we have considered only the x component of the velocity field, $\dot{m}_e$ being the mass flux on the e face, computed as

$$\dot{m}_e = \int_{S_e} u_j n_j\, dS \approx (\boldsymbol{u} \cdot \boldsymbol{n})_e\, S_e. \tag{2.15}$$

In order to compute the diffusive flux F^d

$$F_e^d = \int_{S_e} \frac{1}{Re} \frac{\partial u}{\partial x_j} n_j\, dS \approx \frac{1}{Re} (\boldsymbol{\nabla} u \cdot \boldsymbol{n})_e\, S_e, \tag{2.16}$$

the gradient of u at the cell face center is needed. First, we approximate the derivative at the CV center by the average value over the cell

$$\left(\frac{\partial u}{\partial x_i}\right)_P \approx \frac{\int_V \frac{\partial u}{\partial x_i}\, dV}{V_P}, \tag{2.17}$$

then, we apply the Gauss theorem to the numerator

$$\int_V \frac{\partial u}{\partial x_i}\, dV = \int_S u\boldsymbol{e}_i \cdot \boldsymbol{n}\, dS \approx \sum_c u_c S_c^i \text{ for } c = e, n, w, s, b, t, \tag{2.18}$$

where $\boldsymbol{e}_i$ is the unit vector in the i-th direction. Finally, the derivative can be computed as

$$\left(\frac{\partial u}{\partial x_i}\right)_P \approx \frac{\sum_c u_c S_c^i}{V_P}. \tag{2.19}$$

Using interpolated cell face values to compute the derivative may generate an oscillatory solution. To solve this problem we use the so-called deferred correction method [11] as proposed by Muzaferija [69], where an additional term is added which is the difference between the correct and approximated flux. The diffusive flux is corrected as follows

$$F_e^d = F_e^d{}_{\text{impl}} + \left[F_e^d{}_{\text{expl}} - F_e^d{}_{\text{impl}}\right]^{\text{old}}, \tag{2.20}$$

where "old" means a value from the previous iteration or time step, and "expl" or "impl" means that the term is treated explicitly or implicitly, respectively.

When the line connecting nodes P and E is orthogonal to the cell face, the derivative with respect to $\boldsymbol{n}$ can be approximated by a derivative with respect to the coordinate $\boldsymbol{e}_\xi$ along that line, and the implicit flux is written with a second order accurate approximation as

$$F_e^d{}_{\text{impl}} = \frac{1}{Re} S_e \left(\frac{\partial u}{\partial \xi} \right)_e . \tag{2.21}$$

When the grid is non-orthogonal, the deferred correction term must contain the difference between the gradient in the $\boldsymbol{n}$ and $\boldsymbol{e}_\xi$ directions (see Figure (2.1b)). So, the diffusive flux can be written as

$$F_e^d = \frac{1}{Re} S_e \left(\frac{\partial u}{\partial \xi} \right)_e + \frac{1}{Re} S_e \left[\left(\frac{\partial u}{\partial n} \right)_e - \left(\frac{\partial u}{\partial \xi} \right)_e \right]^{\text{old}} , \tag{2.22}$$

where the first term on the right hand side is the one treated implicitly, while the second one is the deferred correction, which is calculated using interpolated cell center gradients, resulting in the following expression for the diffusive fluxes

$$F_e^d = \frac{1}{Re} S_e \frac{u_E - u_P}{L_{P,E}} + \frac{1}{Re} S_e \left(\boldsymbol{\nabla} u \right)_e^{\text{old}} \cdot \left(\boldsymbol{n} - \boldsymbol{e}_\xi \right) . \tag{2.23}$$

If the line connecting nodes P and E is orthogonal to the cell face, the deferred correction term is null as expected. Note that, this correction does not affect the second-order accuracy of the method.

2.1.1 Time discretisation

The numerical solution of the incompressible Navier-Stokes equations is complicated by the lack of an independent equation for the pressure. In fact, the continuity equation does not have an explicit time derivative applied to the pressure or to the density variable. Indeed, in incompressible flows, the continuity equation is just a kinematic constraint on the velocity field, rather than a dynamic equation. One way to solve this problem is to rely on the fractional step method. This technique was firstly developed by Chorin [25] and later on modified and improved by several other authors. The results obtained in the thesis rely on a modified version of the method originally proposed by Kim and Moin [52]. The algorithm is based on the Hodge's decomposition of the velocity field into a solenoidal and an irrotational part, and consists of two stages: the prediction step, where the momentum equation is solved without satisfying the continuity equation, and the correction step, where the previous solution is corrected by projecting the velocity field onto a divergence-free field.

We can write the numerical discretization of the incompressible Navier-Stokes equations concisely as follows

$$\frac{\boldsymbol{u}^* - \boldsymbol{u}^n}{\Delta t} = -\mathcal{N}_l \left(\boldsymbol{u}^n, \boldsymbol{u}^{n-1} \right) + \frac{1}{Re} \mathcal{L} \left(\boldsymbol{u}^*, \boldsymbol{u}^n \right) - \mathcal{G} \left(\phi^n \right) , \tag{2.24}$$

$$\frac{\boldsymbol{u}^{n+1} - \boldsymbol{u}^*}{\Delta t} = -\mathcal{G}\left(\phi^{n+1}\right), \tag{2.25}$$

with the constraint

$$\mathcal{D}\left(\boldsymbol{u}^{n+1}\right) = 0. \tag{2.26}$$

$\boldsymbol{u}^*$ is the predicted velocity field, $\boldsymbol{u}^n$ the solenoidal velocity field at time n, Δt the time step, $\mathcal{N}_l$, $\mathcal{G}$, $\mathcal{D}$ and $\mathcal{L}$ are the discrete non-linear, gradient, divergence and Laplacian operators, respectively, and ϕ is the projection variable. Note that, the operators include coefficients that are specific to the selected time scheme. The variable ϕ^{n+1} to be used in the projection (Equation (2.25)) can be found by solving a Poisson equation for ϕ, obtained by applying the divergence operator to Equation (2.25), which gives

$$\mathcal{L}\phi^{n+1} = \frac{1}{\Delta t}\mathcal{D}\left(\boldsymbol{u}^*\right), \tag{2.27}$$

with the boundary condition

$$\frac{\partial \phi^{n+1}}{\partial n} = 0, \tag{2.28}$$

with $\boldsymbol{n}$ being the outward normal vector. So, the sequence to solve the incompressible Navier-Stokes equations by a fractional step method consist of a prediction step (Equation (2.24)), a Poisson equation (Equation (2.27)), and a final correction step (Equation (2.25)). Computationally speaking, the most expensive step is the one related with the solution of the Poisson pressure equation. However, when the span-wise direction is homogeneous, periodic boundary conditions can be assumed and a $3D$ Poisson equation can be transformed into a series of two-dimensional Helmholtz equations in wave number space via a Discrete Fast Fourier transform (FFT). In particular, assuming z to be the periodic direction, ϕ is transformed in the wave number space using the discrete anti-transform

$$\phi\left(x, y, z\right) = \sum_{l=0}^{N-1} \hat{\phi}_l\left(x, y\right) exp\left(ilz\right), \tag{2.29}$$

where $\hat{\phi}_l$ is the l^{th} Fourier coefficient of ϕ and N is the number of modes considered (i.e., $l = 0, \ldots, N-1$). Using the orthogonality property of the Fourier system, we obtain a set of decoupled Helmholtz equations

$$\frac{\partial^2 \hat{\phi}_l}{\partial x^2} + \frac{\partial^2 \hat{\phi}_l}{\partial y^2} - k_l \hat{\phi}_l = \hat{r}_l, \tag{2.30}$$

where k_l is the modified wave number and $\hat{r}_l$ is the Fourier transform of the right hand side of Equation (2.27). Further details can be found in [20].

When a colocated arrangement of variables on a numerical grid is used, the divergence term of Equation (2.27) requires the values of the velocities at cell faces that can be obtained by linear interpolation. As a consequence, the Poisson

equation needs to be discretised on a grid which is coarser than the one used for the predicted variables. The mismatch in the number of discrete values makes the kernel of the pressure operator non trivial giving rise to pressure spurious modes. To eliminate those modes we use a method originally proposed by Rhie and Chow [77]. Initially, we solve the momentum equation as usual, and then (before solving the Possion equation) the mass fluxes obtained with the interpolated velocity are corrected by subtracting the difference between the pressure gradient and the interpolated gradient at the cell face location obtained at the previous time step

$$\dot{m}_e = (\boldsymbol{u} \cdot \boldsymbol{n})_e S_e - \Delta t S_e \left[(p_E - p_P) - \boldsymbol{\nabla} p \cdot \boldsymbol{e}_\xi \right]^{\text{old}} . \tag{2.31}$$

This method automatically detects the oscillations and smooths them out.

2.1.2 Numerical implementation

The discrete counterparts of Equation (2.3) and Equation (2.4) have been implemented in a well-established curvilinear finite volume code [71, 72, 81] written in `Fortran 77`. As previously mentioned, the code approximates the fluxes using a second-order central formulation (Figure (2.2a)), and the Rhie and Chow method [77] to avoid pressure oscillations. The equations are advanced in time by a second-order semi-implicit fractional-step procedure [52], where the implicit Crank-Nicolson scheme is used for the wall normal diffusive terms, and the explicit Adams-Bashforth scheme is employed for all the other terms. The Poisson pressure equation obtained when using a pressure correction method to enforce the solenoidal condition on the velocity field is transformed into a series of two-dimensional Helmholtz equations in wave number space via Fast Fourier transform (FFT) in the spanwise direction. Each of the resultant elliptic $2D$ problem is then solved using a preconditioned Krylov method (`PETSc` library [6]). In particular, for the problem at hand, we have found the iterative Biconjugate Gradient Stabilized (BiCGStab) method with an algebraic multigrid preconditioner (boomerAMG) [42] to behave quite efficiently. The code is parallelized

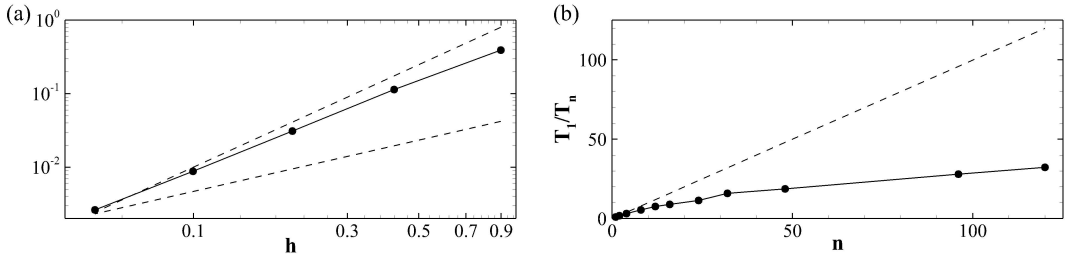

FIGURE 2.2: (a) Spatial accuracy of the finite volume code. The dashed lines represents the first and second order accuracy, while the solid line is the accuracy of our finite volume code. (b) Scalability of the finite volume code. The dashed line represents the reference linear value, while the solid one is the speed-up of our code.

using the domain decomposition technique and the `MPI` message passing library. Figure (2.2b) shows the scalability of the code, defined as the ratio between the time needed to perform one time-step with one processor T_1 divided by the time using n processors T_n. The test was performed with a 3D C-grid around an aerofoil with $480 \times 206 \times 96$ points in the x, y and z directions respectively. A validation of the baseline code using a classical turbulent flow is given in the next section.

2.1.3 Turbulent channel flow

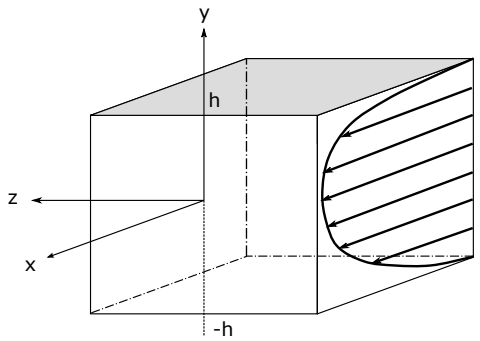

FIGURE 2.3: Sketch of the channel geometry.

We consider the flow of an incompressible viscous fluid through a channel with impermeable walls, as sketched in fig 2.3. We introduce the Cartesian coordinate system shown in figure 2.3, where x, y and z denote the stream-wise, wall-normal and span-wise coordinates, while u, v and w denote the respective components of the velocity vector field. The lower and upper walls are located at $y = -h$ and $y = h$, respectively. At the walls, we impose the no-penetration and no-slip conditions. It is assumed that the fully developed turbulent channel flow is homogeneous in the stream-wise and span-wise directions, so that periodic boundary conditions can be used in these directions. To make the problem dimensionless, we define as a characteristic length L^* one-half the channel

$$L^\star = h, \tag{2.32}$$

and as characteristic velocity $U^\star$ the bulk velocity

$$U^\star = U_b = \frac{1}{2h}\int_{-h}^{h} U dy, \tag{2.33}$$

where $U(y)$ is the mean velocity profile. With this choice, the Reynolds number is defined as

$$Re_b = \frac{U_b h}{\nu}, \tag{2.34}$$

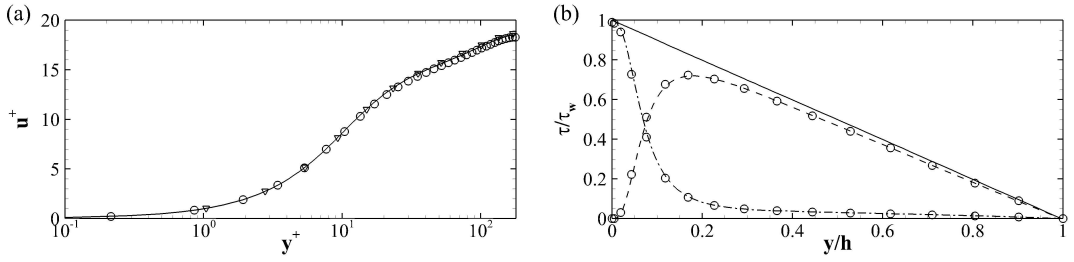

FIGURE 2.4: (a) Mean velocity profile in wall units. (b) The total shear stress (solid line), decomposed in the viscous stress (dash-dotted line) and Reynolds shear stress (dashed line) obtained from from simulation. The circles in both the plots are used for the results by Kim, Moin and Moser [53], while the triangles in the fist plot are used for our result on a coarser grid.

where ν is the kinematic viscosity defined as $\nu = \mu/\rho$. The bulk Reynolds number Re_b is fixed to 2800, and the computation is carried out on a grid of $256\times192\times192$ points, in the x, y and z directions respectively. The computational domain size is set to $2\pi h \times 2h \times \pi h$ in the x, y ans z directions. With the mentioned grid, the resolution turns out to be $\Delta x^+ \approx 5$ in wall units in the stream-wise direction, $\Delta z^+ \approx 3$ in the span-wise direction, and with a minimum Δy^+ in the wall-normal direction which is less than 1.

The wall units, indicated by the superscript " $^+$ ", are measured in terms of the dimensionless viscous length δ_ν, which is defined as follows

$$\delta_\nu = \frac{1}{u_\tau Re}, \tag{2.35}$$

where u_τ is the dimensionless friction velocity. Note that we use the viscous length and the friction velocity as reference length scale and velocity scale, respectively, in the near-wall regions. For a turbulent channel flow with solid walls, the friction velocity is defined as follows

$$u_\tau = \sqrt{\frac{1}{Re}\left.\frac{d\overline{u}}{dy}\right|_{y=-1}}, \tag{2.36}$$

where $\overline{u}$ is the mean velocity, $y/h = -1$ is the location of the wall, and the " $^-$ " indicates the average over both time and homogeneous directions, x and z. The Reynolds number based on the friction velocity u_τ and the channel semi-height is called friction Reynolds number Re_τ, and is defined as $Re_\tau = u_\tau h/\nu$. In our case, the friction Reynolds number is $Re_\tau = 180$.

Figure (2.4a) shows the mean velocity profiles $u^+ = u/u_\tau$ versus the logarithm of the distance from the wall $\tilde{y} = y - 1$ expressed in wall-units. The solid line is used for the results of our simulation, while the circles for the reference values of Kim, Moin and Moser [53]. In the same figure, the black triangles correspond

to the results of another simulation, on a grid with half points in each direction, which is used to assess the grid convergence of the results. The agreement is very good, even if our friction velocity is slightly underestimated.

The total shear stress τ, defined as the sum of the Reynolds shear stress $\overline{u'v'}$ with the viscous stress

$$\tau = \frac{1}{Re}\frac{d\overline{u}}{dy} - \overline{u'v'}. \tag{2.37}$$

is given in Figure (2.4b), compared with the results by Kim, Moin and Moser [53]. As for the mean velocity profile, the agreement between our simulation and the reference data is very good.

The next section will introduce the immersed boundary method which is the technique that has been chosen to deal with the presence of complex and/or moving portions of the boundary.

2.2 Immersed Boundary Method

The Immersed Boundary Method (IBM) is a numerical technique used to simulate flow fields past bodies that do not necessarily conform with the computational grid. The pioneer of this numerical technique has been Charles Peskin that back in the seventies was able to simulate the flow of blood inside a heart [73]. As mentioned, the main feature of this method is that the numerical grid does not need to conform to the geometry of the object, which is replaced by a body force distribution $\boldsymbol{f}$ that mimic the effect of the body on the fluid by restoring the desired velocity boundary values on its immersed surface. The main advantage of the IBM is the simplification of the grid generation task. In fact, grid topology and its quality are not determined by the complexity of the geometry. The advantage of the IBM becomes quite clear for flows with moving boundaries, where the process of generating a new grid at each time step is avoided, since the grid can be kept stationary and non-deforming. A drawback of the approach is that the grid lines are not aligned with the body surface, so in order to obtain the required resolution, higher number of grid points may be required. Many IBMs have been proposed in the past. The main difference between the methods is related with the way in which the Immersed Boundary force is computed. IBMs can be grouped in two main categories, the continuous and discrete forcing ones. In the first approach the forcing is incorporated into the continuous equations before discretization, whereas in the second approach the forcing is introduced after the equations are discretized. The method that we will use belongs to the first group, and is termed as Reproducing Kernel Particle Method (RKPM) and was developed by Pinelli et al. [61, 62, 74].

Next, we explain how the equations are modified to take into account the presence of an immersed body when using the RKPM approach. Firstly, the surface Γ of the immersed surface delimiting the body is discretized using N

markers, called Lagrangian points $\boldsymbol{X}$. The latters, in general do not correspond with the grid nodes $\boldsymbol{x}$. To advance in time the Navier-Stokes equations, a simple prediction step (Equation (2.24)) is performed, without taking into account the immersed object. The obtained velocity field $\boldsymbol{u}^*$ is then interpolated (with an interpolator operator $\mathcal{I}$) onto the embedded geometry Γ,

$$\boldsymbol{U}^* = \mathcal{I}\left(\boldsymbol{u}^*\right). \tag{2.38}$$

The values of $\boldsymbol{U}^*$ are used to determine a distribution of singular forces along Γ that restore the prescribed boundary values $\boldsymbol{U}^\Gamma$ as

$$\boldsymbol{F}^* = \frac{\boldsymbol{U}^\Gamma - \boldsymbol{U}^*}{\Delta t}. \tag{2.39}$$

The force field defined over Γ is then transformed into a body force distribution applied to the fluid grid using a convolution operator $\mathcal{C}$

$$\boldsymbol{f}^* = \mathcal{C}\left(\boldsymbol{F}^*\right). \tag{2.40}$$

The momentum conservation equation is then solved again with the computed volume force field added as a source term

$$\frac{\boldsymbol{u}^* - \boldsymbol{u}^n}{\Delta t} = -\mathcal{N}_l\left(\boldsymbol{u}^n, \boldsymbol{u}^{n-1}\right) + \frac{1}{Re}\mathcal{L}\left(\boldsymbol{u}^*, \boldsymbol{u}^n\right) - \mathcal{G}\left(\phi^n\right) + \boldsymbol{f}^*. \tag{2.41}$$

Finally, the time advancement step can be completed with the usual solution of the pressure Poisson equation and the projection step. The given procedure is common to a number of IB methods. The step that define the present method concern the way in which the operators $\mathcal{I}$ and $\mathcal{C}$ are built.

2.2.1 Interpolation and convolution

We use the Reproducing Kernel Particle Method (RKPM) [61, 62, 101, 74] to define interpolation and spreading operators. In this method the approximation $f_a\left(x\right)$ of the value of a given smooth function at point $x \in \Omega$ can be expressed as a kernel approximation

$$f_a\left(x\right) = \int_\Omega w_\delta\left(x - s\right) f\left(s\right) ds, \tag{2.42}$$

where w_δ is a non-negative kernel function of compact support, and the subscript indicates that the kernel depends on a parameter δ, called dilation parameter, which determines the dimension of the support Ω_I. So, w_δ is non-zero only in a sub-domain Ω_I of Ω and zero elsewhere. A discrete approximation of the kernel function was proposed by Roma et al. [79] (see Figure (2.5a))

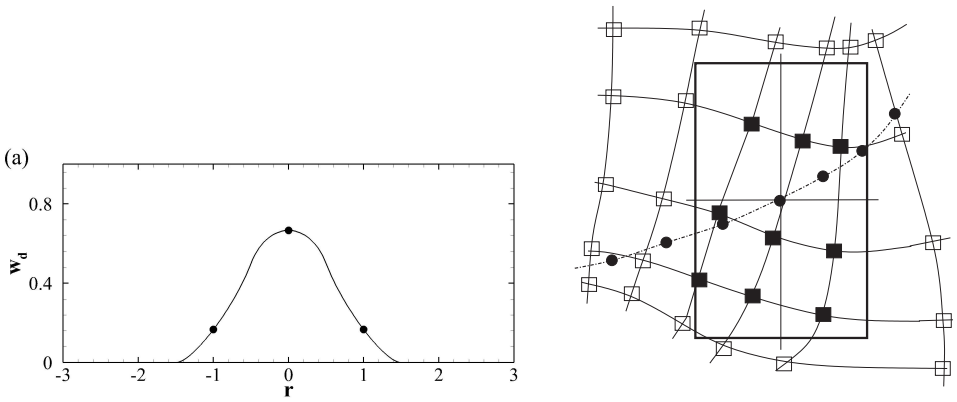

FIGURE 2.5: (a) Kernel function proposed by Roma et al. [79]. (b) The black rectangle is the cage around one of the Lagrangian points, shown as dots. The squares represents grid points, and the black ones are the grid points falling within the cage.

$$w_\delta(r) = \begin{cases} \frac{1}{6}\left(5 - 3|r| - \sqrt{-3\left(1-|r|\right)^2 + 1}\right), & \text{if } 0.5 \leq |r| \leq 1.5, \\ \frac{1}{3}\left(1 + \sqrt{-3r^2+1}\right), & \text{if } 0.0 \leq |r| \leq 1.5, \\ 0, & \text{otherwise,} \end{cases} \tag{2.43}$$

where $r = (x-s)/\delta$. This approximation of w_δ satisfies the following properties

1. $w_\delta(r)$ is continuous;
2. $w_\delta(r) = 0$ if $|r| > 1.5$;
3. $\sum_l w_\delta(r-l) = 1$;
4. $\sum_l (r-l)\, w_\delta(r-l) = 0$;
5. $\sum_l [w_\delta(r-l)]^2 = 1/2$.

In the the last three properties, the sums are performed $\forall l \in \mathbb{N}$, and are satisfied $\forall r \in \mathbb{R}$. For example, for $r = 0.0$, the function w_d is not null for $l = -1, 0, 1$ where it is equal to $\frac{1}{6}, \frac{2}{3}, \frac{1}{6}$ (see the dots in Figure (2.5a)). Since the previous properties involve the natural number l, they can be satisfied by a function interpolated using Equation (2.42) and Equation (2.43) only if the nodes are equispaced. To extend this approach to a non-uniform nodes distribution, following Liu et al. [62] and Pinelli et al. [74], we use a modified window function $\widetilde{w}_\delta$, defined as

$$\widetilde{w}_\delta(x-s) = \sum_{i=0}^{n} b_i (x-s)^i\, w_\delta(x-s), \tag{2.44}$$

where b_i are $n+1$ coefficients determined by imposing the continuous equivalent of properties 3 and 4, which are

$$\widetilde{m}_i(x) = \int_\Omega (x-s)^i\, \widetilde{w}_\delta(x-s)\, ds = \delta_{i0} \text{ for } i = 0, 1, \ldots, n \tag{2.45}$$

where δ_{ij} is the Kronecker's delta. Note that, these conditions imply the exact representation of the elements of the canonical polynomial base $\{1, x, x^2, \ldots\}$. The number n is the higher order of the polynomial that we want to represent exactly. For example, $n = 2$ would lead to an exact representation of all polynomials of degree up to 2. Substituting Equation (2.44) into Equation (2.45), we obtain

$$\widetilde{m}_i(x) = \int_\Omega (x-s)^i \widetilde{w}_\delta(x-s)\, ds = \sum_{j=0}^{n} b_j m_{i+j}(x) = \delta_{i0}, \tag{2.46}$$

for $i = 0, 1, \ldots, n$, where we have defined

$$m_i(x) = \int_\Omega (x-s)^i w_\delta(x-s)\, ds. \tag{2.47}$$

The above equations form a symmetric linear system $M\vec{b} = \vec{e}_1$, where the right hand side $\vec{e}_1$ is a vector, whose elements are all zeros, except the first one which is equal to 1. From the solution of this linear system (Equation (2.46)) we can obtain the coefficients b_i, and, finally, we can write the corrected window function (here given for $n = 2$) as

$$\widetilde{w}_\delta(x-s) = \left[b_o + (x-s)\, b_1 + (x-s)^2 b_2\right] w_\delta(x-s). \tag{2.48}$$

The procedure can be extended to higher dimensions, defining the window function as a Cartesian product of the $1D$ kernels. In $2D$, it becomes

$$w_{\delta,\eta}(x-s, y-t) = w_\delta(x-s)\, w_\eta(y-t) \tag{2.49}$$

and in $3D$

$$w_{\delta,\eta,\sigma}(x-s, y-t, z-v) = w_\delta(x-s)\, w_\eta(y-t)\, w_\sigma(z-v), \tag{2.50}$$

where δ, η and σ are the dilatation parameters in the coordinates directions. The linear systems to find the coefficients $b_{i,j}$ and $b_{i,j,k}$ are obtained from the following conditions

$$\widetilde{m}_{i,j} = \int_\Omega (x-s)^i (y-t)^j \widetilde{w}_{\delta,\eta} ds = \delta_{l0} \text{ for } i, j = 0, 1, \ldots, n, \tag{2.51}$$

in $2D$, where $l = i + j$ and $i + j \leq n$, and

$$\widetilde{m}_{i,j,k} = \int_\Omega (x-s)^i (y-t)^j (z-t)^k \widetilde{w}_{\delta,\eta,\sigma} ds = \delta_{l0} \text{ for } i, j, k = 0, 1, \ldots, n, \tag{2.52}$$

in $3D$, where $l = i + j + k$ and $i + j + k \leq n$. So, the corrected window functions in $2D$ and $3D$ are

$$\begin{aligned} \widetilde{w}_{\delta,\eta}(x-s, y-t) = [&b_{0,0} + (x-s)\, b_{1,0} + (y-t)\, b_{0,1} + \\ &(x-s)(y-t)\, b_{1,1} + (x-s)^2 b_{2,0} + (y-t)^2 b_{0,2}] \times \\ &w_{\delta,\eta}(x-s, y-t), \end{aligned} \tag{2.53}$$

and

$$\begin{aligned}\widetilde{w}_{\delta,\eta,\sigma}\left(x-s,y-t,z-v\right)=&\left[b_{0,0,0}+\left(x-s\right)b_{1,0,0}+\left(y-t\right)b_{0,1,0}+\left(z-v\right)b_{0,0,1}+\right.\\&\left(x-s\right)\left(y-t\right)b_{1,1,0}+\left(y-t\right)\left(z-v\right)b_{0,1,1}+\left(z-v\right)\left(x-s\right)b_{1,0,1}+\\&\left.\left(x-s\right)^{2}b_{2,0,0}+\left(y-t\right)^{2}b_{0,2,0}+\left(z-v\right)^{2}b_{0,0,2}\right]\times\\&w_{\delta,\eta,\sigma}\left(x-s,y-t,z-v\right),\end{aligned}\tag{2.54}$$

respectively.

Finally, we briefly describe the implementation of the IB based on RKPM. Around each Lagrangian node $\boldsymbol{X}$ we define a cage that contains at least three nodes of the underlying mesh in each direction, as shown in Figure (2.5b), whose edges measure 3δ, 3η and 3σ in x, y and z, respectively. After finding the set of mesh nodes that fall within the cage, the terms of the moment matrix (Equation (2.52)) can be numerically evaluated to assemble the local window function, using the mid-point quadrature rule. The coefficients $\vec{b}$ of the correction polynomials are found by solving the symmetric linear system $M\vec{b}=\vec{e}_1$ for each Lagrangian points. Due to the very low values that the window function may take at the nodes close to the boundary of the cage, the moment matrix may become ill conditioned. This problem is avoided by rescaling the linear system, and solving the equivalent one $HMH^{-1}\vec{b}=\vec{e}_1$, where the diagonal matrix H has the inverse of the dilation factors in the main diagonal. In $3D$ H is

$$H=\operatorname{diag}\left(1,\frac{1}{\delta},\frac{1}{\eta},\frac{1}{\sigma},\frac{1}{\delta\eta},\frac{1}{\eta\sigma},\frac{1}{\delta\sigma},\frac{1}{\delta^{2}},\frac{1}{\eta^{2}},\frac{1}{\sigma^{2}}\right).\tag{2.55}$$

Once the coefficients b have been found, the window function $\widetilde{w}_{\delta,\eta,\sigma}$ can be used for the interpolation (Equation (2.38)) and spreading (Equation (2.38)) operations. In particular, the discrete interpolation, using a mid point rule becomes

$$U_l=\mathcal{I}\left(u_{i,j,k}\right)=\sum_{i,j,k\in\Omega_I}u_{i,j,k}\tilde{w}_{\delta,\eta,\sigma}\left(x_{i,j,k}-X_l\right)\Delta V_{i,j,k},\tag{2.56}$$

while the spreading operation reads

$$f_{i,j,k}=\mathcal{C}\left(F_l\right)=\sum_{l=1}^{N}F_l\tilde{w}_{\delta,\eta,\sigma}\left(x_{i,j,k}-X_l\right)\epsilon_l,\tag{2.57}$$

where ϵ_l is a characteristic volume related to the local dilation coefficients of the window function. To determine the correct value of ϵ, first, we consider the value of the force on the Lagrangian points, obtained by interpolation

$$F_l=\sum_{i,j,k\in\Omega_I}f_{i,j,k}\tilde{w}_{\delta,\eta,\sigma}\left(x_{i,j,k}-X_l\right)\Delta V_{i,j,k},\tag{2.58}$$

then, we replace $f_{i,j,k}$ with Equation (2.57)

$$F_l = \sum_{i,j,k \in \Omega_I} \left[\sum_{l=1}^{N} F_m \tilde{w}_{\delta,\eta,\sigma} \left(x_{i,j,k} - X_m \right) \epsilon_m \right] \tilde{w}_{\delta,\eta,\sigma} \left(x_{i,j,k} - X_l \right) \Delta V_{i,j,k}. \tag{2.59}$$

Equation (2.59) can be written using a matrix notation as

$$A \mathrm{diag} \left(\vec{\epsilon} \right) \vec{F} = \vec{F}. \tag{2.60}$$

By requiring that $\vec{\epsilon}$ is independent of the actual force distribution, we obtain the constraint $\det \left[A \, \mathrm{diag} \left(\vec{\epsilon} \right) \right] = 0$, whose solution is found by solving

$$A \vec{\epsilon} = \vec{1}, \tag{2.61}$$

where $\vec{1}$ is a vector, whose elements are all ones. As shown by Pinelli et al. [74], the conditioning of the matrix A depends on the ratios between the distances of the Lagrangian nodes and the local grid size. When the Lagrangian spacing is approximately equal to the local grid size (or slightly higher), the linear system for $\vec{\epsilon}$ is well conditioned and is easily solved.

2.2.2 Flow around a cylinder

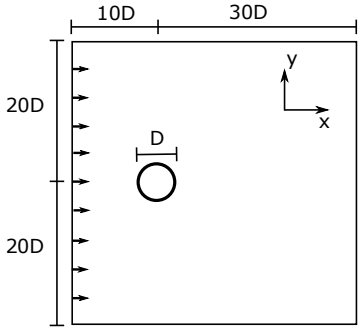

FIGURE 2.6: Sketch of the computational domain around a cylinder.

To validate the RKPM immersed boundary implementation, we consider the flow of an incompressible viscous fluid around a circular cylinder, as sketched in Figure (2.6). We introduce the Cartesian coordinate system shown in Figure (2.6), where x and y denote the stream-wise and normal coordinates, while u and v denote the respective components of the velocity vector field. On the lower and upper surfaces, we impose the free-slip condition, while the no-penetration and no-slip conditions are imposed on the body surface. Uniform velocity in the

stream-wise direction U_∞ is imposed at the inlet of the domain, while a convective outlet condition is imposed at the outlet. To make the problem dimensionless, we use as a characteristic length L^* the cylinder diameter

$$L^* = D, \tag{2.62}$$

and as characteristic velocity U^* the free-stream velocity

$$U^* = U_\infty. \tag{2.63}$$

Consistently, the Reynolds number is defined as

$$Re_D = \frac{U_\infty D}{\nu}. \tag{2.64}$$

The diameter Reynolds number is fixed to $Re_D = 100$, and the computation is

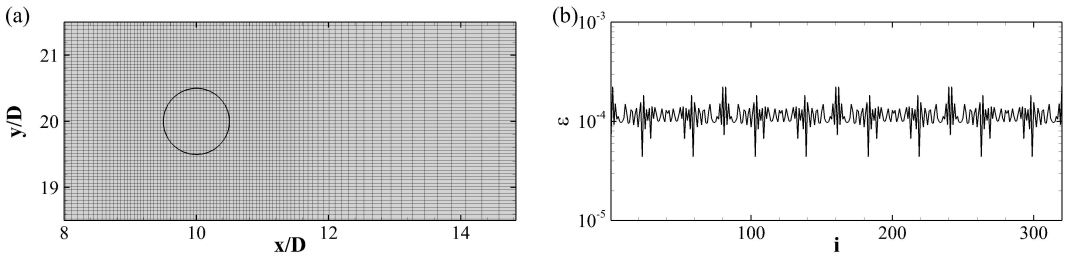

FIGURE 2.7: (a) Grid in the proximity of the cylinder (nodes are plotted with a skip index of 5). (b) The values of ϵ for every Lagrangian points.

carried out on a grid of 696×696 points, covering a computational domain of $40D \times 40D$. The center of the cylinder is located at $(10D, 20D)$, and its surface is discretised with 320 equispaced Lagrangian points. The grid has an uniform spacing of 0.001 in the cylinder region, and stretches towards the boundaries of the domain. Note that, grid points are present also inside the cylinder, as shown in Figure (2.7b). Figure (2.7b) reports the values of ϵ for all the Lagrangian points. Note that, the square root of the average value 0.00011 is approximately equal to the mesh size.

Figure (2.8a) shows the instantaneous span-wise vorticity ω_z fields around the cylinder. At this Reynolds number, the wake of the cylinder is characterised by a von Karman vortex street typical of bluff bodies. Vortices of opposite sign are shed from the cylinder periodically, at a Strouhal number equal to $S_t = f_s D/U_\infty = 0.17$, which is close to the experimental value of $S_t = 0.165$ reported by Williamson [97]. The value was obtained by the spectrum of the instantaneous lift coefficient value, whose time history is reported in Figure (2.8b) with a solid line together with the drag coefficient shown with a dashed line. The mean lift and drag coefficients are $C_L = 0.0$ and $C_D = 1.38$, respectively, with

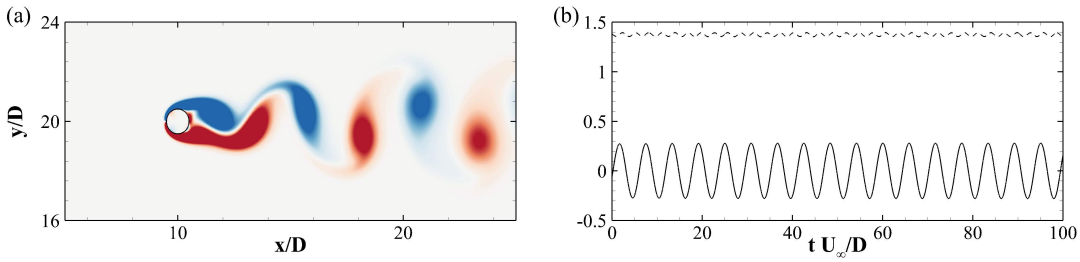

FIGURE 2.8: (a) Contours of the span-wise vorticity ω_z. (b) Evolution of the lift C_L (blue) and drag coefficients C_D (red) over time.

TABLE 2.1: Aerodynamic coefficients for the cases analysed. The data from the first row are taken from Guilmineau and Queutey [37].

Case	N	C_L^{max}	C_D
Ref [37]	–	0.36	1.35
Cyl-1	102	0.32	1.46
Cyl-2	144	0.33	1.45
Cyl-3	240	0.34	1.45
Cyl-4	288	0.34	1.41
Cyl-5	320	0.35	1.38
Cyl-6	350	0.35	1.38

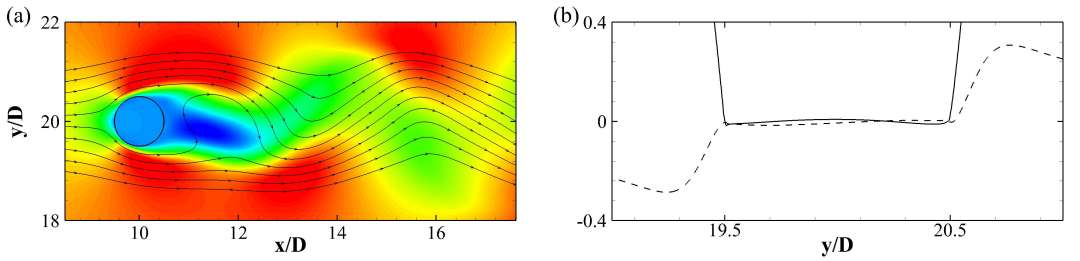

FIGURE 2.9: (a) Contours of the stream-wise velocity u. (b) u (solid line) and v (dashed line) velocity profiles, coloured in red and blue, respectively, at $x = 10D$.

the maximum absolute lift value equal to $C_L^{max} = 0.35$. These results are in good agreement with the one obtained by Guilmineau and Queutey [37] who found a mean drag coefficient $C_D = 1.35$, and a maximum lift equal to $C_L^{max} = 0.36$. Table (2.1) reports the mean drag coefficients C_D and the maximum instantaneous lift coefficients C_L^{max} obtained from various simulations, changing the number of Lagrangian points used to represent the cylinder surface. We notice that the cases with 320 and 350 points have the same values, thus indicating that 320 points is enough to correctly represent the solid cylinder at this Reynolds number.

Figure (2.9a) shows the instantaneous x-component of the velocity field around

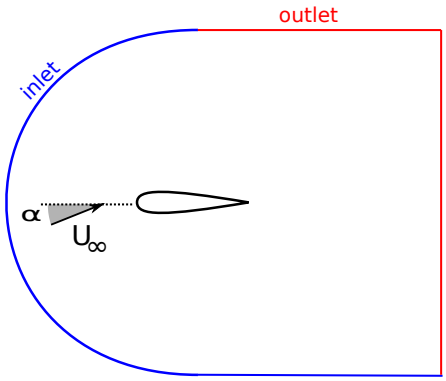

FIGURE 2.10: Sketch of the computational domain.

the cylinder. In Figure (2.9b) the u and v velocity profiles on a vertical line passing through the centre of the cylinder at $x = 10D$ are reported using solid and dashed lines, respectively. Both the velocity components have values close to 0 at the cylinder boundary, and small but non zero values inside the cylinder, a typical situation encountered when using IB methods.

2.3 Flow around aerofoils

We now briefly describe the numerical set-up that has been used as a common ground to simulate the flow around an infinite NACA0020 wing. In particular, we will introduce the grid system, the boundary conditions, and the technique used to keep into account the aerofoil rotation. This section finalizes with the description of a test case used to validate the numerical implementation used for the DNS of the flow around aerofoils.

2.3.1 Numerical set-up

We now consider an incompressible three-dimensional unsteady flow field around a straight wing with an infinite span-wise dimension z (x_3). The computational domain is shown in Figure (2.10). The coordinate system is Cartesian with the x and y axis (x_1 and x_2) denoting the directions parallel and normal to the aerofoil chord, respectively. Also, u, v and w (u_1, u_2 and u_3) denote the correspondent components of the velocity vector field parallel and normal to the chord, and along the span. The Reynolds number $Re_c = U_\infty c/\nu$ is based on the chord length of the aerofoil c and the approaching free-stream velocity magnitude U_∞. We use U_∞ and c as the velocity and length scales for normalisation throughout the rest of the thesis.

The flow domain around the aerofoil is meshed using a body fitted C grid arrangement, as in Figure (2.10). The grid system for the three dimensional case

is obtained by repeating the baseline $2D$ grid uniformly in the spanwise direction. With this arrangement, the external surface that bounds the computational domain, contains both the inlet and the outlet (see Figure (2.10)). To determine which portion of the boundary in all parallel x-y planes is either an inlet or an outlet, at each time step a local spanwise average of the fluid velocity is evaluated in a tiny region close to the boundary. When the averaged flow direction points outward, the corresponding portion of the boundary is assumed to be an outlet, and is treated using a convective boundary condition. Conversely, if the flow direction is directed inward, the corresponding boundary surface is considered to be an inlet, and a Dirichlet type condition based on an irrotational approximation is employed. In particular, the values to be assigned to the velocity on the Dirichlet portions of the boundary are determined by solving a companion potential equation discretised via a Hess-Smith panel method [43].

Finally the remaining boundary conditions are imposed by enforcing: impermeability and no slip conditions on the aerofoil wall, periodic conditions on the planes bounding the domain in the spanwise direction, and continuity of the flow variables through the symmetry plane generated by the C-grid shape downstream of the trailing edge.

2.3.2 Aerofoil rotation

When considering an aerofoil undergoing a time variation in its angle of incidence, one can consider a frame of reference mounted on the aerofoil. In particular, the frame shown in 2.10, is a non-inertial one, which rotates around the z-axis, having its centre of rotation located at a quarter of the chord ($x^o = 0.25c$). We define the angle of rotation between the two reference axis as $\theta = -\alpha$. The Navier-Stokes equations (Equation (2.1) and Equation (2.2)) in a non-inertial frame of reference are modified as follows,

$$\frac{\partial u_i}{\partial t} + \frac{\partial u_i u_j}{\partial x_j} = -\frac{\partial p}{\partial x_i} + \frac{1}{Re}\frac{\partial^2 u_i}{\partial x_j \partial x_j} + \left(\ddot{\theta} I^{\theta}_{ij} x_j + 2\dot{\theta} I^{\theta}_{ij} u_j + \dot{\theta}^2 x_i\right), \tag{2.65}$$

$$\frac{\partial u_i}{\partial x_i} = 0. \tag{2.66}$$

where all the variables are evaluated in the non-inertial frame of reference, and the terms in the brackets are the inertial forces. In particular, the three terms are the Euler, the Coriolis, and the centrifugal forces, respectively. I^{θ} is an auxiliary matrix defined as

$$I^{\theta} = \begin{bmatrix} 0 & 1 & 0 \\ -1 & 0 & 0 \\ 0 & 0 & 1 \end{bmatrix}. \tag{2.67}$$

The boundary condition are modified as well. In particular, a Dirichlet condition becomes

$$u_i = R^{\theta}_{ij} v_j + \dot{\theta} I^{\theta}_{ij} x_j, \tag{2.68}$$

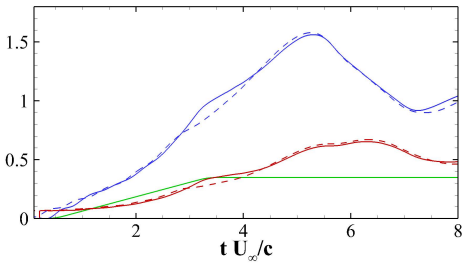

FIGURE 2.11: Lift C_L (blue) and drag C_D (red) coefficients as a function of time. The solid line is used for the case with inertial forces, while the dashed line for the case without. The green line represents the time variation of the angle of attack.

where v_i is the Dirichlet value for the velocity in the inertial frame, and R^θ is the rotation matrix

$$R^\theta_{ij} = \begin{bmatrix} \cos(\theta) & \sin(\theta) & 0 \\ -\sin(\theta) & \cos(\theta) & 0 \\ 0 & 0 & 1 \end{bmatrix}, \tag{2.69}$$

while the Neumann condition for the Poisson equation remains unchanged. To avoid numerical oscillations the function $\theta = \theta(t)$ has been made continuous up to its second derivative, thus, we use a ramp function with smoothed start and finish.

An alternative, simplified approach to represent the time variation of the angle of attack is to modify the Dirichlet inlet conditions in time. At each time step, the velocity components are modified to keep into account the change in the direction of the freestream velocity vector. This method does not reproduce standard wind tunnel experiments where the aerofoil is rotated around a revolution axis. However, for low values of $\dot{\theta}$ and $\ddot{\theta}$, the two approaches lead to similar results in terms of integral quantities, with some discrepancy in the shape and evolution of the wake (see Wong et al. [98]). In the ramp-up manoeuvre that will be analysed, we will consider $\dot{\theta}$ as a constant except in short periods of time at the beginning and at the end of the manoeuvre, when $\ddot{\theta}$ is adjusted to enforce a smooth time variation of θ. In Figure (2.11), we compare the lift and drag time history using the two described approaches, using a value of $\dot{\theta}c/U_\infty = 0.12$. In the graph, the solid lines are used for the solution of the Navier-Stokes equations written in a non-inertial frame of reference, while the dashed lines are for the one obtained by simply varying the angle of attack by imposing the boundary condition at the far-field consistent with the instantaneous direction of the velocity vector at infinity. We can notice that the two cases are quite similar, with both showing the lift overshoot and its breakdown typical of dynamic stall (this behaviour will be discussed in the next chapters of the thesis). In view of the marginal difference in the results obtained using the two approaches, we have decided to carry out all the unsteady simulations using an inertial frame of reference and varying the inlet conditions. This approach allows simpler considerations and computations.

TABLE 2.2: Aerodynamic coefficients, separation and reattachment points for a NACA0012 at $\alpha = 5^o$ and $\alpha = 8^o$ ($Re_c = 50000$). The first two rows values are from Lehmkuhl et al. [59], the second two correspond to our predictions.

Case	α	C_L	C_D	x_s/c	x_r/c
Val-5-Ref	5^o	0.57	0.029	0.065	0.57
Val-8-Ref	8^o	0.76	0.050	0.024	0.32
Val-5	5^o	0.57	0.028	0.100	0.57
Val-8	8^o	0.73	0.049	0.032	0.30

2.3.3 Flow around an aerofoil: validation

The baseline code used for this thesis has been extensively validated for various turbulent flows in the past [70, 71, 72]. However, to further corroborate the predictive capabilities of the code in aeronautical contexts, we report a specific validation of the flow over a NACA0012 aerofoil. We compare our numerical results with the ones obtained by Lehmkuhl et al. [59] and by Rodriguez et al. [78]. In particular, we have considered the aerofoil at a chord Reynolds number $Re_c = 5 \times 10^4$, and at angles of attack $\alpha = 5^o$ and $\alpha = 8^o$. The simulation domain has been set up and discretised as previously described. We have used a grid of $2545 \times 490 \times 48$ points in the x_1, x_2 and x_3 directions, with a reduced spanwise extent of the domain (set to $0.2c$, as in [78]).

The comparison with the reference data turns out to be quite satisfactory. In particular, Figure (2.12a) shows the pressure coefficient distribution over the aerofoil surface at the two angles of attack obtained in the present simulations versus the ones given in [59]. At both angles of attack all the predictions show the presence of a separation bubble on the suction side of the aerofoil, resulting in a plateau in the pressure coefficient. At $\alpha = 5^o$ the flow separates at $x_s \approx 0.10c$ and reattaches at $x_r \approx 0.57c$, while at $\alpha = 8^o$ the separation occurs at $x_s \approx 0.03c$ and the reattachment at $x_r \approx 0.30c$. A quantitative comparison with the results

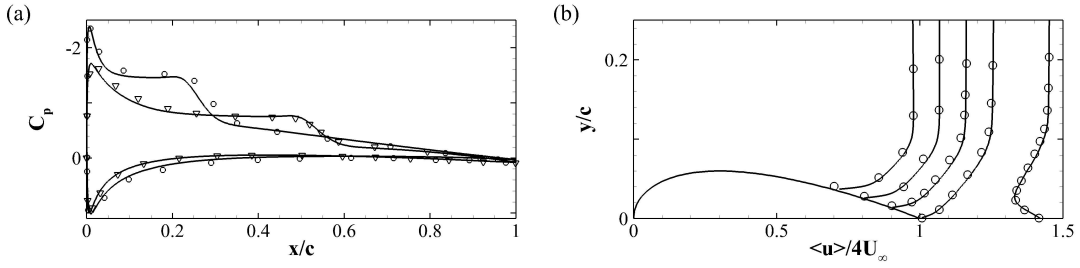

FIGURE 2.12: (a) Distribution of the mean pressure coefficient over the NACA 0012 aerofoil at 5^o (triangle) and 8^o (circle). (b) Mean x-velocity profiles at 8^o. The profiles are at $x/c = 0.7$, 0.8, 0.9, 1.0, and 1.2. In both figures, the solid lines are from the actual simulations, while symbols are used for the results from Lehmkuhl et al. [59].

by Lehmkuhl et al. [59] is given in Table (2.2). In general, we find an overall good agreement with the reference results, with a slightly retarded separation predicted by our simulations. Figure (2.12b) shows the mean x-velocity profiles in the vicinity of the trailing-edge and in the near wake region at $\alpha = 8^o$. Again, good agreement with the results from the reference is observed.

Chapter 3

Flow around an aerofoil in static and dynamic stall

3.1 Introduction

The flow around aerofoil at high angle of attack in full stalled condition is a problem of great interest in aerodynamics and fluid-dynamics, since it involves separation of the flow from the leading edge, transition to turbulence in the separated shear layer and the shedding of vortices in the wake, the latter being responsible of strong fluctuation in the lift and drag. The static stall of aerofoil can be classified into three basic types [48, 65]: i) trailing-edge stall, when the separation starts from the trailing edge and moves forward with increasing angle of attack, ii) leading-edge stall, which results from the burst of laminar separation bubble, and iii) thin-aerofoil stall, characterised by flow separation at the leading edge with reattachment in a point which moves progressively downstream with increasing angle of attack. Note that, the aerofoil stall type depends on several variables (Reynolds number, surface roughness or free-stream turbulence), therefore, its stall type may change when flow conditions are changed. Broeren and Bragg [15] showed that the most severe unsteady effects are those encountered in the thin-aerofoil and trailing-edge stall type.

Dynamic stall is an unsteady phenomenon that appears on lifting objects in response to time variations of the angle of attack. A classical example is the flow over aerofoils undergoing large amplitude pitching motions that can lead to dramatic changes in the aerodynamic loads and thus to potentially catastrophic technological consequences. Because of its dramatic impact on several applications, a considerable number of researches have extensively studied these phenomena in the past [38, 63, 64, 67, 68, 17]. Indeed, dynamic stall can affect the performance and operational limits of many engineering and aeronautical applications, such as helicopters, highly manoeuvrable aircraft and wind turbines. The aim of dynamic stall research varies for each application. For example, while

on the helicopter blades the objective is mainly to inhibit the formation of the dynamic stall vortex, on fixed wing aircraft, the idea could be to sustain the lift overshoot generated by the dynamic stall vortex formation to enhance the manoeuvrability.

So far, experimental works have mainly focused on unsteady flows over two-dimensional aerofoils undergoing prescribed pitching motions [38, 28, 29, 30, 31, 63, 64, 57, 67, 68]. Most of these works [38, 28, 29, 30, 31, 63, 64] have also investigated the influence on the aerodynamic response of various parameters, such as aerofoil geometry, Reynolds and Mach numbers, oscillation amplitude and frequency. Halfman et al. [38] created a combined experimental and theoretical method able to predict the effect of the dynamic stall on the aerodynamic load. This approach was further developed by Ericsson and Reding [28, 29, 30, 31]. McCroskey [63, 64] described the main physical features of the phenomenon and classified the dynamic stall into two categories: light and deep stall, the former being characterised by a loss of lift and an increase in drag which are of the same magnitude as the one associated with the classical static stall, and by a size of the separated region in the order of the aerofoil thickness. Conversely, deep stall is characterised by a lift overshoot, due to the passage of a large scale vortex over the suction side of the aerofoil, followed by a lift breakdown associated with the vortex detachment. Deep stall is also characterised by a separated region with a size in the order of the aerofoil chord. Shih et al. [87], using particle image velocimetry visualisations, suggested that the main stall vortex is induced by the early boundary layer separation near the leading-edge of the aerofoil, and that full stall occurs when the boundary layer detaches completely from the aerofoil. Acharya and Metwally [2] have highlighted the presence of two pressure peaks in the forward portion of the aerofoil. The first suction peak grows in magnitude as the aerofoil pitches up, while the second one corresponds to the dynamic stall vortex and moves downstream.

High fidelity numerical simulations of dynamic stall in configuration of aeronautical interest are particularly expensive due to the broad range of time and space scales involved in the phenomenon: the unsteady variations of the angle of attack becomes slower and slower compared to the fastest turbulence time scale as the Reynolds number is increased. For this reasons Direct and Large Eddy Simulations (DNS and LES) are confined to low/intermediate Reynolds numbers while higher Reynolds Simulations are normally dealt with Reynolds-Averaged Navier-Stokes simulations (RANS). However, conventional turbulence models are known to fail in producing reliable solutions in such complex, out of equilibrium conditions: unsteady, recirculating and locally transitional flow.

A complete review on the numerical simulations of dynamic stall [83, 99, 91, 7, 96, 26, 34] can be found in the work of Ekaterinaris and Platzer [27]. One of the major outcomes of this survey is a list of research topics that required further advancements for achieving reliable predictions. Several other works have highlighted the difficulties that RANS calculations encounter when dealing with

dynamic stall. In particular, Wang et al. [96] used two variants of the $k-\omega$ model, the standard and the SST one, to simulate the flow at moderate high Reynolds number $Re_c = 10^5$. From a comparison with experimental results, they noticed that the models can not precisely capture the size and position of the dynamic stall vortex. Moreover, the quality of the predictions of the models deteriorate as the angle of attack increases. Dumlupinar and Murthy [26] further investigated the performances of various turbulence models and pointed out that different turbulence closures predict a broad range of different behaviours even in the light stall case.

Although several experimental and numerical studies have contributed in elucidating the main physical mechanism that come into play on the flow behaviour when the angle of attack undergoes a dynamic change, to our knowledge the only high fidelity numerical simulations (i.e., DNS or resolved LES) which have been carried out so far are the implicit Large Eddy Simulations of a pitching aerofoil undertaken by Visbal [93, 94]. Those simulations can be considered to be a pioneering work aimed towards a more detailed understanding of the physical mechanisms that determine the dynamic stall vortex creation and its detachment. The understanding of this basic phenomenon would enable to devise new strategies and devices to control the changes in the aerodynamic loads. In this work, for the very first time we aim at performing a direct numerical simulation of the transitional flow around an aerofoil in ramp-up motion. In a companion simulation we also study the flow in a fully separated condition (at the same maximum angle of attack) to establish a baseline benchmark case to allow a cross comparison between the aerodynamic behaviour in a static and dynamic stalled condition.

3.2 Set-up

The aerofoil that has been selected for the present study is a symmetric NACA0020. All the simulations have been undertaken by fixing the Reynolds number based on the magnitude of the freestream velocity and the chord length to 20000. The angle of attack is kept at 20^o in the static case, and varies according to a ramp function in the dynamic case. In the latter, the angle of attack is varied at a constant rate equal to $\dot{\alpha} = 0.12U_\infty/c$ until a maximum incidence of 20^o is achieved.

We now give more details on the grid system. The mesh in Figure (3.1) has been generated in the xy-plane with particular care to its orthogonality and stretching features using the commercial software Pointwise [75], with hyperbolic PDE extrusion methods. The resulting grid has a minimum included angle (83.19^o) exactly matching the geometrical constraint of the trailing edge, see Figure (3.1), while the average grid included angle in all the domain is equal to 89.97. In the wall normal direction, the grid is almost uniform from the aerofoil surface up to 3 chords in order to capture all the separated region and the wake

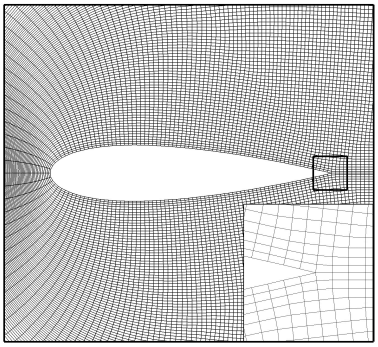

FIGURE 3.1: Grid in the proximity of the aerofoil (nodes are plotted with a skip index of six). The inserted figure is an enlargement of the area surrounding the trailing edge.

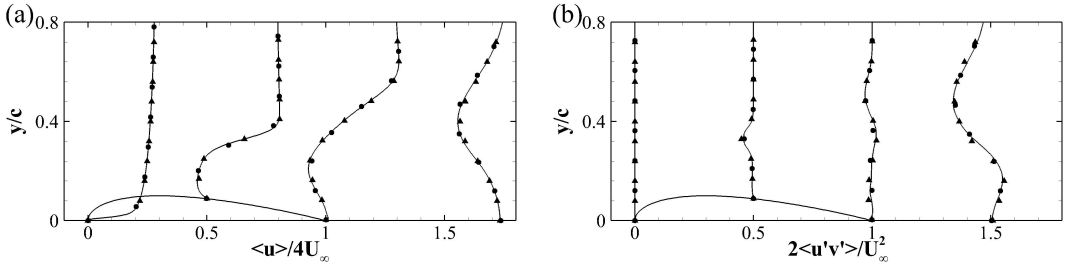

FIGURE 3.2: Mean streamwise velocity $< u >$ (a) and shear component of the Reynolds sress tensor $< u'v' >$ (b) profiles over the wing and in the near wake. The solid lines are used for the reference grid, the circles and the triangles for the coarse and fine grids, respectively.

at high Reynolds number. Further away from the surface, it is coarsened with an increasing stretching factor, which maximum is located near the external boundary where it is equal to 1.03. In the direction parallel to the aerofoil, the grid is uniform over the wing and very slightly stretched (1.001) in the wake region. A buffer layer with higher stretching factor (1.015) is used near the outlet to suppress reflections. The three dimensional mesh is then obtained by repeating the two dimension grid in the spanwise direction with uniform spacing.

The grid density has been tuned by considering a number of preliminary two and three dimensional simulations. The former allowed us to establish the grid spacing requirements in the laminar portion of the flow featuring separation and convective instabilities. The latter was used to determine the grid resolution requirements in the turbulent flow regions. Through these preliminary simulations, undertaken at various incidence angles, we have found that a grid with $2785 \times 626 \times 97$ nodes in the x_1, x_2 and x_3 direction ($-2c < x_1 < 8c$, $-7c < x_2 < 7c$, and $0 < x_3 < 0.9c$), respectively, delivered a sound resolution

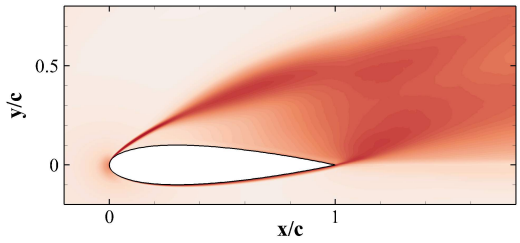

FIGURE 3.3: Contours of the ratio between the grid size h and the Kolmogorov length scale η. Contour levels go from 0 (white) to 1.2 (red).

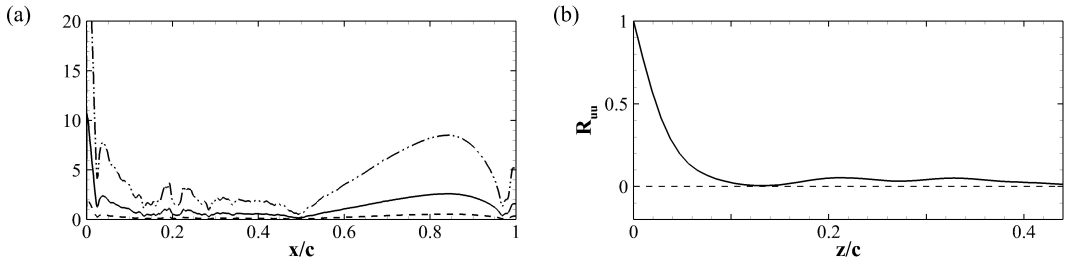

FIGURE 3.4: (a) Mesh resolution at the wall. The resolution in the x, y and z directions are shown with a solid, dashed and dash-dotted line, respectively. (b) Span-wise two-point correlation of the u velocity component in the near wake region.

compromise throughout the whole incidence range. We also made sure that, in terms of local wall units the corresponding mesh resolution verifies $\Delta x^+ < 3.0$, $\Delta y^+ < 0.5$ and $\Delta z^+ < 7.5$ where the superscript $+$ indicates values made non-dimensional using the viscous length ν/u_τ and the friction velocity $u_\tau = \sqrt{\tau_w/\rho}$ (see Figure (3.4a)). The grid dependency of the results has been evaluated by considering the first and second order statistics. In particular, we have tested a coarser and a finer grid obtained by decreasing and increasing by 30% the number of grid points in all the three directions, and the comparison between the three cases is shown in Figure (3.2). The comparison between the medium and finer grid showed no significant differences.

The quality of the grid resolution used in the present computations has been also assessed by means of a posteriori analysis of the zones off the wall. To do this, the grid size $h \approx \sqrt[3]{V}$ has been compared to the Kolmogorov length scale η, obtained from the dissipation rate ϵ as,

$$\eta = \left(\frac{\nu^3}{\epsilon}\right)^{\frac{1}{4}}, \tag{3.1}$$

where the turbulent kinetic energy dissipation rate can be evaluated as

$$\epsilon = 2\nu < \mathcal{S}'_{ij}\mathcal{S}'_{ij} >, \tag{3.2}$$

being $\mathcal{S}'_{ij}$ the fluctuation rate of strain tensor. Figure (3.3) shows the contour of the ratio h/η close to the aerofoil, which is in the order of one in the whole recirculating region, i.e., $h \approx \mathcal{O}(\eta)$. So, the grid spacing should be fine enough to resolve the smallest flow scales at the selected Reynolds number.

Finally, concerning the spanwise size of the domain, its adequacy to contain the largest scales of the flow has been determined by comparing the spanwise two-point correlation at various xy coordinates. The two-point correlation is defined as follows

$$R_{ii}(\boldsymbol{x}, \boldsymbol{r}) = \frac{\overline{u'_i(\boldsymbol{x}) u'_i(\boldsymbol{x}+\boldsymbol{r})}}{\overline{u'^2_i(\boldsymbol{x})}}, \tag{3.3}$$

where the bar denotes average over time and homogeneous direction z. The computed two-point correlation, shown in Figure (3.4b), becomes negligible when approaching $0.13c$, less than half of the domain size ($0.45c$), which guarantees a good decorrelation between the periodic end planes.

3.3 Static high angle of attack

3.3.1 Flow statistics

We now consider the flow over the NACA 0020 aerofoil at an angle of incidence of 20^o. The flow statistics have been collected during $100c/U_\infty$ time units after the initial transient. Averaging in the spanwise homogeneous direction and over 100 external time units (based on c and U_∞) was largely sufficient to produce statistically steady results. The mean x-velocity component is shown in Figure (3.5a), together with the pressure coefficient C_p (Figure (3.5b)) and the friction coefficient C_f (Figure (3.5c)). From the mean velocity iso contours in Figure (3.5a), it clearly appears that the aerofoil is in a fully stalled condition with a large recirculation zone present on the whole suction side. The separation bubble occupies a volume of $0.5c$ in the y-direction and $0.3c$ in the x-direction behind the trailing edge, where a secondary recirculation appears. The primary recirculation zone generates a plateau in the pressure coefficient (Figure (3.5b)) which extends on the whole suction side after a small suction peak near the leading edge, while the reduced pressure region at the trailing edge is due to the secondary recirculation. Another smaller recirculation bubble is visible at $0.25c$ centred in proximity of the location of the aerofoil maximum thickness. The presence of this separation bubble, extending from $x = 0.15c$ to $x = 0.50c$, can also be educed from the friction coefficient distribution (Figure (3.5c)). Figure (3.5a) also shows u-velocity profiles in 3 different positions along the chord (at the leading edge $x = 0.0c$, at the mid chord $x = 0.5c$, and at the trailing edge $x = 1.0c$) and further downstream in a location within the wake ($x = 1.5c$). The given profiles show that at the leading edge, the flow is attached and the boundary layer starts developing with a strong adverse pressure gradient (Figure (3.5b)) that results into separation of

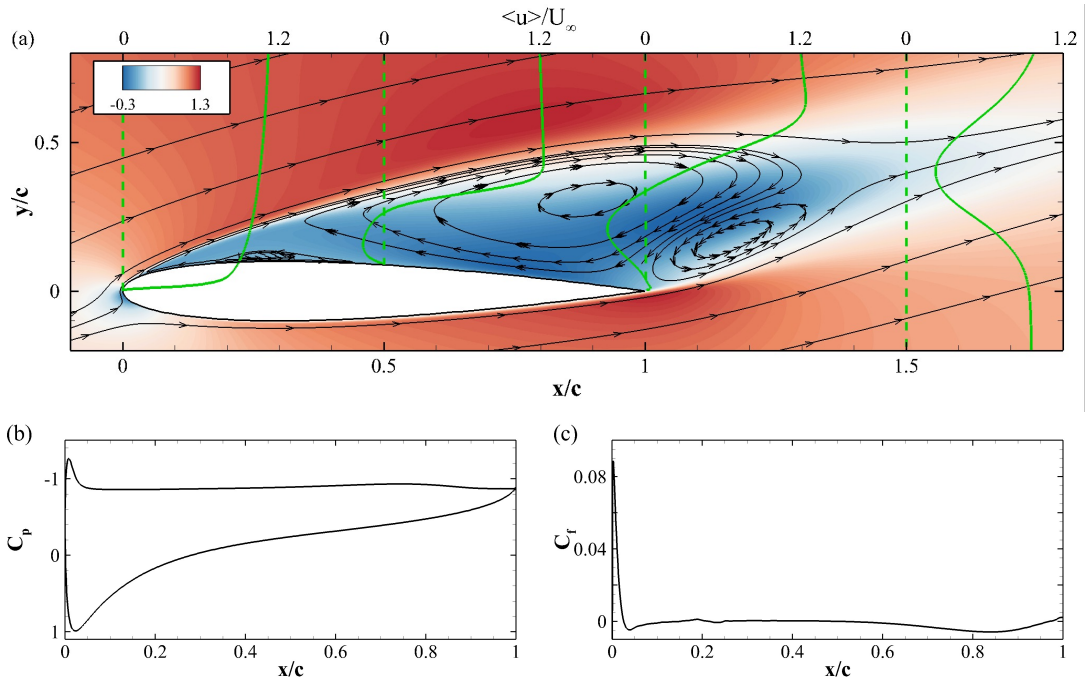

FIGURE 3.5: (a) Contours of mean flow x velocity and streamlines, (b) pressure and (c) friction coefficient of NACA 0020 aerofoil at an angle of attack $\alpha = 20^o$ and with a Reynolds number $Re_c = 2 \times 10^4$.

the flow at $x = 0.025c$; at mid chord the flow is reversed near the aerofoil and, after attaining a maximum negative velocity value at $y = 0.15c$, it grows until reaching zero value at $y = 0.26c$; at the trailing edge, the x-velocity component becomes zero at $y = 0.04c$ after having formed a tiny shear layer with positive velocity, and further away from the aerofoil it reaches the value $-0.29U_\infty$ (close to the absolute minimum in the whole domain) at $y = 0.21c$, to recover again a zero value at $y = 0.33c$. Finally, the last profile shows the velocity profile within the wake, featuring a characteristic defect shape and a positive minimum value $0.22U_\infty$ reached at $y = 0.40c$.

Figure (3.6) shows the diagonal $u_t'u_t'$ (Figure (3.6a)) and off diagonal $u_t'u_n'$ (Figure (3.6b)) components of the Reynolds stress tensor, where u_t and u_n are the fluctuating velocity components tangent and normal to the free-stream velocity direction, respectively. High values of the stresses are present in the wake behind the aerofoil, and in other two regions: within a tiny shear layer originating from the leading edge which bounds the clockwise recirculating region, and behind the trailing edge where the anti-clockwise recirculation takes place. All the Reynolds stresses vanish at the wall due to the no-slip condition and far from the aerofoil surface where the flow is laminar. One can also notice that the approaching flow is laminar, as shown by the 0 values of the stresses profile at the leading edge. At $x = 0.5c$ the stresses have low intensities in the recirculating region near the

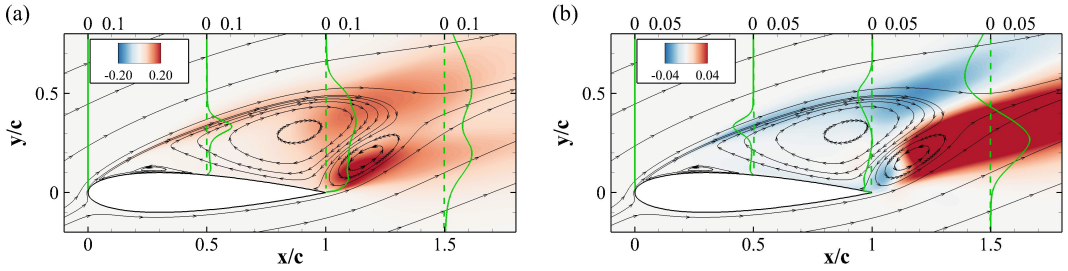

FIGURE 3.6: (a) Contours of tangent $< u_t' u_t' > /U_\infty^2$ (b) and shear $< u_t' u_n' > /U_\infty^2$ components of the Reynolds stress tensor. Mean flow streamlines and some profiles are also shown.

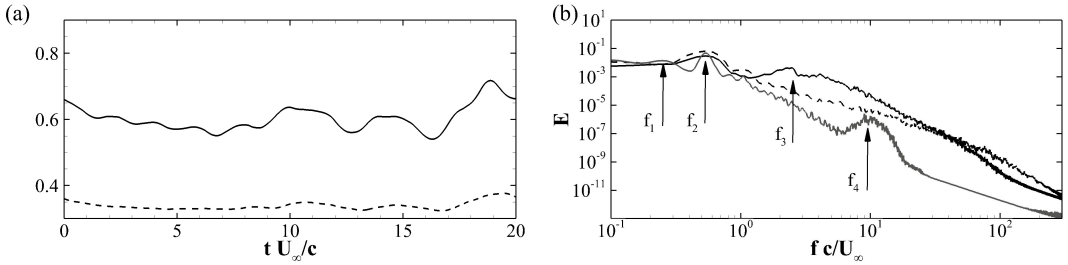

FIGURE 3.7: (a) Lift C_L (solid line) and drag C_D (dashed line) coefficients as a function of time. (b) Spectra of the time autocorrelation of the u velocity component at points P01 (gray solid line), P02 (black solid line) and P03 (dashed line).

wall, and then form a peak located at $y = 0.12c$. In the wake behind the trailing edge the Reynolds stresses have two peaks located at $y = 0.26c$ and $0.59c$, the first peak having a higher intensity than the second. The high stress intensity in the wake zone is mainly due to the flow separation taking place at the trailing edge of the aerofoil, with a smaller contribution from the shear layer formed at the leading edge. Both these regions are responsible to shed vorticity of opposite sign in the wake, carrying different contributions in terms of intensities and thus breaking the symmetry of the wake.

Figure (3.7a) shows the lift and drag coefficients as a function of time. These distributions have been obtained by integrating the pressure and shear stress at the wall. Their mean values are $C_L = 0.64$ and $C_D = 0.35$, respectively. These values, compared with the ones reported by Skillen et al. [88], obtained via a large eddy simulation of the flow around a similar aerofoil at same incidence but at higher Reynolds number, show small discrepancies with slightly higher lift (3%) and drag (6%) coefficients. From the figure, it is also possible to notice the presence of a dominant frequency. This frequency corresponds to the shedding of vortices in the wake, and its non dimensional value in terms of Strouhal number is $St = f_s c/U_\infty \approx 0.534$. An alternative Strouhal number based on the windward length $c\sin(\alpha)$ gives a value of $St' = f_s c \sin(\alpha)/U_\infty = 0.183$. This value falls

within the range $0.175 - 0.185$ in agreement with the results of Knisely [55] that also showed that the Strouhal number tends to become independent of the shape of the bluff object when the angle of attack is increased. To further investigate the unsteady nature of the flow field and in particular aiming at tracing the footprint of the vortex generation process originating from the shear layer instability at the leading edge we have computed the spectrum of the time autocorrelation at three different locations (Figure (3.7b)) (P01, P02 and P03). The first one (P01) is located in the shear layer close to the leading edge at $x = 0.10c$, $y = 0.10c$, the second one (P02) in the shear layer near the midchord at $x = 0.40c$, $y = 0.28c$, and the last (P03) near the trailing edge at $x = 1.05c$, $y = 0.08c$. All the spectra show a peak at $St = 0.534$ which is the reported principal wake shedding frequency (f_2). In the shear layer near the leading edge (P01), we observed a peak at lower frequency $f_1 = 0.25U_\infty/c$, corresponding to approximately half the shedding frequency and related to a low frequency flapping motion of the shear layer [78, 54, 23, 22, 44]. In the same spectrum a third peak is present at $f_4 = 9.75U_\infty/c$ corresponding to the vortex generation due to the leading edge KH shear layer instability. Another smooth peak at frequency $f_3 = 2.52U_\infty/c$ is present in the spectrum corresponding to the midchord location (P02). This frequency is lower than f_4 due to the merging of vortices which grows in size. An analogous trend can be observed in Rodriguez et al. [78].

3.3.2 Flow structure

More details on the emerging coherent structures, their interactions and the wake formation process, have been educed using the $\mathcal{Q}$-criterion proposed by Hunt et al. [45]. This technique allocates a vortex to all spatial regions that verify the condition

$$\mathcal{Q} = \frac{1}{2}\left(|\boldsymbol{\Omega}|^2 - |\boldsymbol{S}|^2\right) > 0, \tag{3.4}$$

where $\boldsymbol{S} = \frac{1}{2}\left(\boldsymbol{\nabla u} + \boldsymbol{\nabla u}^T\right)$ is the rate of strain tensor and $\boldsymbol{\Omega} = \frac{1}{2}\left(\boldsymbol{\nabla u} - \boldsymbol{\nabla u}^T\right)$ is the vorticity tensor. Instantaneous $\mathcal{Q}$ iso-surfaces are shown in Figure (3.8a). From this figure, the principal flow features are easily observed: the laminar flow separates at the leading edge, forming a shear layer that rolls up into Kelvin-Helmholtz (KH) vortices [18, 19, 100, 89, 1]; this instability, locally, triggers the flow transition to turbulence; further downstream a turbulent separated region appears to be characterized by fine texture small-scales structures, which eventually merge into coherent larger structures; finally behind the aerofoil, a large turbulent wake is formed, whose shape is similar to a von Karman vortex street typical of bluff bodies, as clearly shown in Figure (3.8b). However, in contrast to classical vortex shedding process showing an alternately series of vortices of opposite sign and equal strength, here the wake is highly asymmetric presenting vortices of uneven strength. As already mentioned, the loss of symmetry and the irregularity of the vortices pattern is related to the interaction between the two

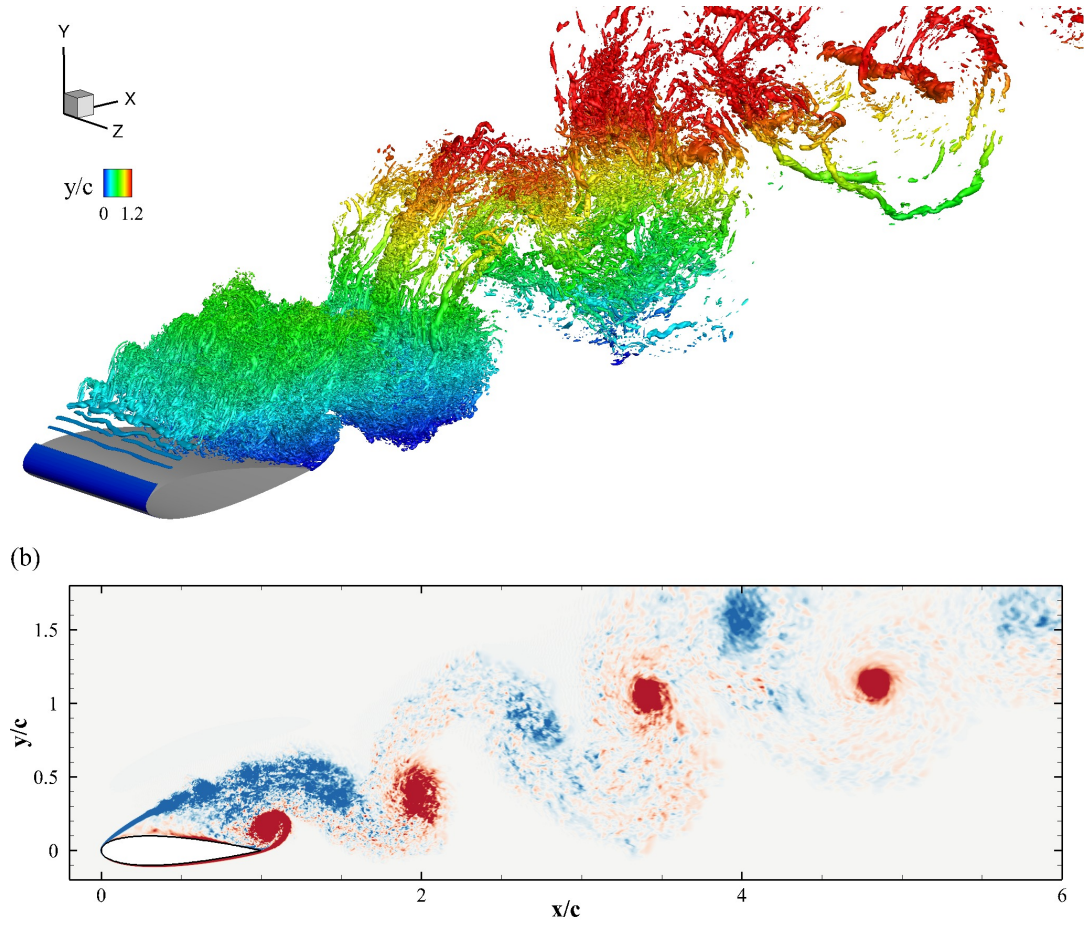

FIGURE 3.8: (a) Visualisation of instantaneous vorticity field by means of $\mathcal{Q}$-isosurfaces ($\mathcal{Q} = 150U_\infty^2/c^2$) coloured by the y-coordinate (distance from centreline). (b) Instantaneous contour plot of the spanwise component of the vorticity ω_z, averaged in the homogeneous z-direction. Blue negative vorticity, red positive ($\pm 7U_\infty/c$).

vortex generating mechanisms (see Breuer and Jovicic [14, 13]): the vortices roll up under the action of the KH leading edge shear layer instability and the street of vortices characterising the wake behind the trailing edge. From Figure (3.8a) shows also the presence of braid-like vortices between each shedding rollers.

Within the Eulerian coherent structures educing techniques, the $\mathcal{Q}$-criterion is probably the most popular one. Even though it enjoys the Galilean invariance property, it has other shortcomings that are typical of Eulerian methods: it lacks objectivity (i.e., not independent of frame rotations), it is based on the numerical evaluation of gradients that may introduce further noise and it requires the empirical specification of a threshold value. On the other hand, methods that are based on a Lagrangian formulation overcome those weaknesses. In particular, one of the most popular Lagrangian approaches is based on computing the Finite-

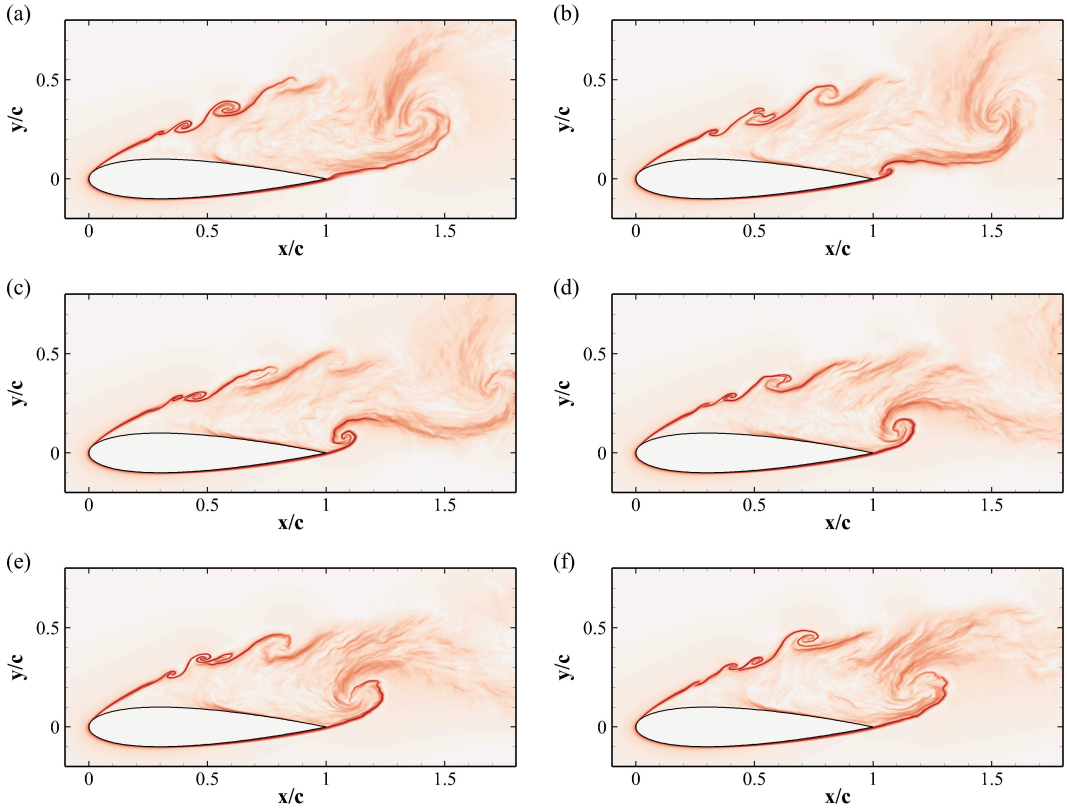

FIGURE 3.9: Instantaneous contour plot of the FTLE σ^T (defined in (3.6)) during a shedding period. Snapshots have been sampled at 6 time instantaneous snapshots by an increment $\Delta T \approx 0.35c/U_\infty$. Darker colours are associated with most unstable LCS. The contour levels go from 0 (white) to $7U_\infty/c$ (red).

Time Lyapunov Exponents (FTLE) (see Haller [39] and Shadden et al. [86]). The FTLE $\sigma^T(\boldsymbol{x}, t)$ is a scalar function of space and time which measures the rate of separation of neighbouring particle trajectories initialised within a small ball centred at $\boldsymbol{x}$ at time t. More precisely, if $\boldsymbol{x}(t, \boldsymbol{x}_0, t_0)$ denotes the position of a particle at time t that originated from position $\boldsymbol{x}_0$ at time t_0, a measure of particles separation rate can be related to the largest singular value of the Cauchy-Green deformation tensor computed over a finite time interval $[t_0, t_0 + T]$

$$\Delta = \frac{\partial \boldsymbol{x}(t_0 + T, \boldsymbol{x}_0, t_0)}{\partial \boldsymbol{x}_0}. \tag{3.5}$$

Once the largest singular value $\lambda_{max}(\Delta)$ is found, the FTLE over the time interval $[t_0, t_0 + T]$ is defined as

$$\sigma^T(\boldsymbol{x}, t) = \frac{1}{T} ln \sqrt{\lambda_{max}(\Delta)}, \tag{3.6}$$

One can use both positive and negative integration times to evince either attracting Lagrangian Coherent Structures (LCS, unstable manifolds) with nega-

tive integration time $T < 0$, or repelling LCS (stable manifolds) characterised by positive integration time $T > 0$ [40]. LCS are therefore used to classify regions in the flow undergoing different dynamical conditions. In particular, the recirculating regions are identified by their association with unstable LCS. Figure (3.9) shows contours of the FTLE, where the coherent structures are associated to local extrema of σ^T. The six different instantaneous snapshots considered in the figure cover a full shedding period $\Delta t = 1.75c/U_\infty$ (see Figure (3.7a)). Figure (3.9a) corresponds to the beginning of the shedding cycle, with no vortex at the trailing edge, and the leading edge shear layer rolling up under the action of a Kelvin-Helmholtz instability. Later on (Figure (3.9b)), also the trailing edge shear layer undergoes a KH instability rolling up and inducing the generation of a trailing edge vortex. In the following instantaneous snapshots, the trailing edge vortex increases in size (Figure (3.9c-d)), interfering with the leading edge KH instability also affecting the thickness and the location of the shear layer. This interaction continues until the trailing edge vortex is fully established and detaches from the aerofoil (Figure (3.9e)). As the trailing edge vortex is convected downstream (Figure (3.9f)), the leading edge shear layer is no more drawn into the separated region, and the undisturbed KH instability process associated with the leading edge induced shear layer is recovered. Ultimately, this cyclic interaction between the leading and trailing shear layers is the responsible of the asymmetry in the wake pattern. At the trailing edge, vortices generated by the flow separation from the aerofoil surface are shed into the wake, while the small scale vortices generated by the Kelvin-Helmholtz instability of the shear layer at the leading edge are periodically either trapped in the recirculating bubble or shed into the wake also increasing their size via a pairing process.

3.4 High angle of attack: ramp-up transient

We now consider the evolution of the flow field around the aerofoil during a ramp-up motion. As already mentioned, in this manoeuvre the angle of attack follows a ramp function in time with an initial linear increase followed by a steady value of the angle. In particular, the angle of attack is varied linearly from 0^o to 20^o with a reduced frequency of $k = \dot{\alpha} = 0.12U_\infty/c$. These values have been selected because matching the experimental conditions of Brucker and Weidner [17] (the reduced frequency is also very close to the one of Mulleners and Raffel [67]). All the simulations have been obtained using snapshots from a fully developed zero degree angle of attack flow conditions. Because of the intrinsic unsteady nature of the flow field, time averaged statistics can no more be defined, and only averages in the homogeneous z-direction can be used. Convergence of the flow statistical quantities has been enhanced by also introducing ensemble averages obtained from different initial conditions. In particular, we have considered ten realisations obtained using ten initial conditions obtained from instantaneous zero

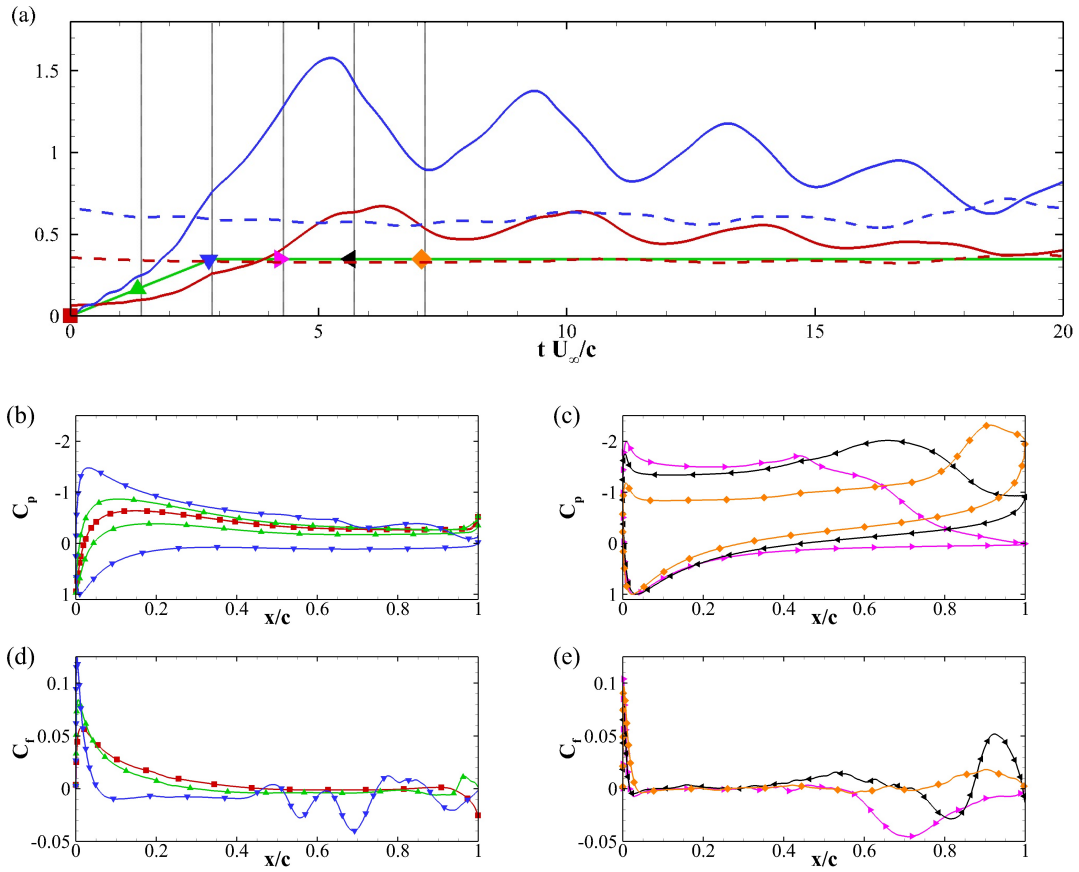

FIGURE 3.10: (a) Lift (blue line) and drag (red line) coefficient over time, with the selection of 6 particular times indicated by the dashed line and the symbols. The solid line is used for the ramp-up case, while the dashed line is for the case at $\alpha = 20^o$. (b)-(c) Pressure coefficient C_p and (d)-(e) friction coefficient C_f at the selected times.

degree flow fields sampled within two shedding cycles. Flow statistics obtained using ensemble averages and span wise planes were fairly converged.

Figure (3.10a) shows the time history of the lift and drag coefficients during the ramp-up motion (solid lines), compared to the case at fixed angle of attack $\alpha = 20^o$ (dashed lines). From the force coefficients diagram we can easily recognise the typical stages of dynamic stall, as described for example by McCroskey [63]. The lift and drag coefficients first increase until reaching maximum values after the end of the linear increase of the angle of attack. Due to the passage of a large scale vortex over the suction side of the aerofoil, the magnitude of the maxima are larger than the static stall values. As this vortex detaches, the force drops abruptly. Finally, they oscillate slowly converging towards the asymptotic static stall values. The maximum lift and drag coefficients are 1.58 and 0.67, respectively, about twice the values of the static case. In the decaying region, the amplitude of the oscillations is much higher than in the static case, while the

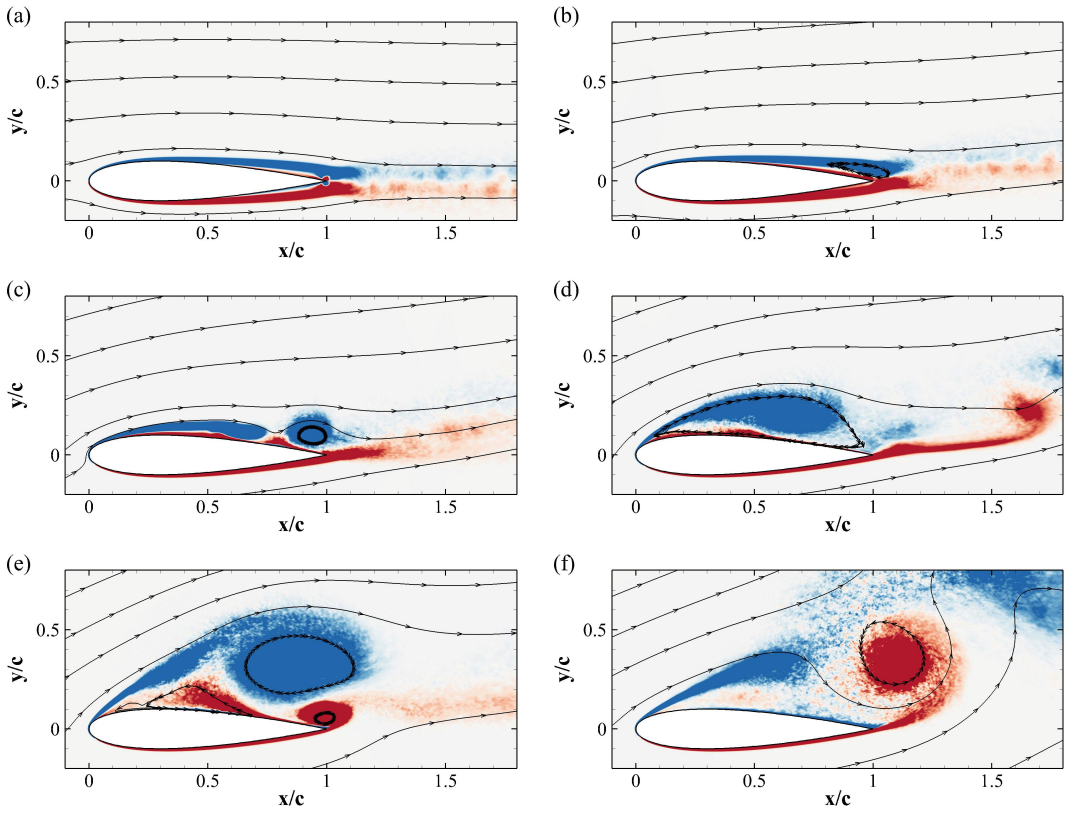

FIGURE 3.11: Contour plots of the space and ensemble average of the spanwise component of vorticity ω_z, sampled at the times given in Figure (3.10a). Blue negative vorticity, red positive ($\pm 7U_\infty/c$).

characteristic shedding frequency is lower in the ramp-up case. Those differences between the dynamic and the static cases become less accentuate approaching the asymptotic state.

Figure (3.10b-c) and Figure (3.10d-e) show the time evolution of the pressure and friction coefficients, C_p and C_f, and Figure (3.11) displays the contours of the span-wise z-component of vorticity ω_z, averaged in the span-wise homogeneous z-direction, sampled at the same six times as the corresponding C_p and C_f distributions (i.e., , the six time instants marked in Figure (3.10a)), with the first corresponding to $\alpha = 0^o$, the second to $\alpha = 10^o$, and the others to $\alpha = 20^o$. At $\alpha = 0^o$ the C_p distribution is symmetric (Figure (3.10b)), with a plateau starting at about the mid-chord position, indicating the presence of a separated region. The rightmost local minimum located by the trailing edge is induced by vortex shedding. The friction coefficient on the suction side of the aerofoil confirms the mentioned boundary layer features, displaying a peak near the leading edge, followed by a smooth decrease (Figure (3.10d)) and the presence of the separation point at about the mid-chord. The flow is symmetric over most of

the aerofoil surface (Figure (3.11a)), except at the trailing edge and in the wake, where contra-rotating vortices are shed from the suction and pressure sides of the wing. As the angle of attack reaches the value of 10^o, the pressure distribution (Figure (3.10b)) and the flow (Figure (3.11b)) are no more symmetric, and the lift starts to increase consequently. The maximum friction coefficient moves towards the leading edge, as well as the separation point (Figure (3.10d)). When the static stall angle is reached, small amplitude C_f oscillations in the trailing edge area become visible. At $\alpha = 20^o$ the lift is still increasing, consistently with the pressure decrease on the suction side (Figure (3.10b)). Also, even if the separation point has now reached the static stall value, the pressure coefficient distribution does not show the typical separation plateau. Compared to the static case, the C_f oscillations take place further upstream towards the leading edge (Figure (3.10d)). When the maximum lift coefficient is approached, the peak of the pressure near the leading-edge is still increasing, and a second peak appears around the mid-chord (Figure (3.10c)). This new peak is induced by a large vortex which has started to form on the suction side (i.e., the so called dynamic stall vortex), see Figure (3.11d). Further downstream, the pressure drops rapidly, while the friction coefficient (Figure (3.10e)) reaches a maximum negative value. During this phase, no vortices are shed from the trailing edge, as can be educed from Figure (3.11d). In later stages, as shown in Figure (3.10c) the pressure peak value at the leading edge starts to decrease, while the secondary peak intensity keeps on increasing in magnitude, moving towards the trailing edge, as the dynamic stall vortex is convected downstream. During the displacement of the dynamic stall vortex, an induced counter rotating vortex is formed at the trailing edge, see Figure (3.11e). When the dynamic stall vortex finally detaches from the aerofoil and the trailing edge vortex reaches its maximum size (Figure (3.11f)), the pressure attains an almost constant distribution indicating a fully separated flow condition (Figure (3.10c)). However, the lift will then start to increase again due to the formation of another shed vortex, whose magni-

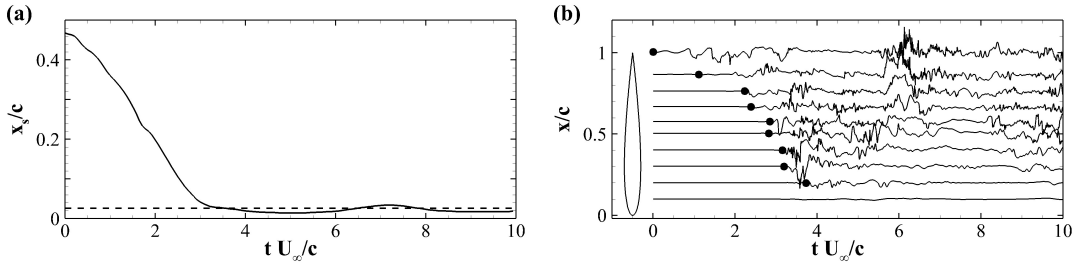

FIGURE 3.12: (a) Time evolution of the downstream separation point during the ramp-up manoeuvre (solid line). The dashed line represents the separation point at 20^o. (b) Fluctuations of the x-velocity components u' as a function of time for various points near the aerofoil surface. The fluctuations are scaled by a factor of 10 and shifted.

tude and intensity is weaker than the first one. This cyclic shedding process is damped in time with vortices of lower intensities until the static condition is asymptotically reached. The time evolution of the separation point is reported in Figure (3.12a). At $\alpha = 0^o$ the separation point is located at $x_s = 0.47c$, moving towards the leading edge as the angle of attack is increased. As already remarked, the static stall separation point $x_s = 0.025c$ is firstly reached when the ramp-up motion is finalised at $t = 3.5c/U_\infty$. In the subsequent stage, when the incidence angle is constant ($\alpha = 20^o$), the separation line moves further upstream featuring a damped oscillating trajectory around its static location.

When commenting Figure (3.10d-e), we have already highlighted the presence of some oscillations in the C_f distribution by the trailing edge region. These oscillations amplify in time affecting larger portions of the profile. The driving mechanism that trigger these oscillations is associated with a KH shear layer instability that starts at the trailing edge and propagates up-stream in time. This phenomenon is analysed in Figure (3.12b) showing the evolution over time of the fluctuations of the stream-wise velocity component at various locations along the aerofoil suction side (as shown in the figure), at a wall normal distance of $0.1c$. The bullets used in the figure indicate the time when the amplitude of the fluctuation reaches the 2.5% of the average value. From this diagram, it appears clearly that initially the x-wise velocity fluctuations are confined to the trailing edge region. Only after 2 time units the fluctuations reach the half chord location. Later on they travel slowly further upstream, but never contaminating the leading edge portion of the aerofoil. Thus, it is clear that the separated region moves upstream in time, with an initial velocity approximately equal to $0.15U_\infty$.

Next, we focus on the time evolution of the turbulent kinetic energy $k = 1/2 < u_i' u_i' >$, shown in Figure (3.13), together with the corresponding mean streaklines. At $\alpha = 0^o$ the flow accommodates smoothly around the aerofoil with low levels of turbulent kinetic energy confined in the wake behind the trailing edge. As the angle of attack is increased (Figure (3.13b-c)), a recirculation zone is formed on the suction side of the aerofoil in the trailing edge region. At later stages, a complete separation occurs affecting the whole suction side (Figure (3.13d)). The associated recirculation zone display high levels of turbulent kinetic energy. The following time frame, Figure (3.13e), shows a completely formed dynamic stall vortex that, later on, will be convected downstream towards the trailing edge. A new contra-rotating bubble is formed at the trailing edge, and other two recirculation regions appear, one at about the the mid-chord location and the other around $x = 0.15c$. Both of them finally vanish when the dynamic stall and trailing edge vortices are shed away from the aerofoil (see Figure (3.13f)).

To better understand the vortex formation and transport processes and the origin of the instabilities arising in the flow, we turn our attention to Figure (3.14) where the evolution of the FTLE σ_t^T is reported. In the figure, the frames are organised time wise, with the right column covering the same instantaneous snapshots marked in Figure (3.10), while the left column displays contours at

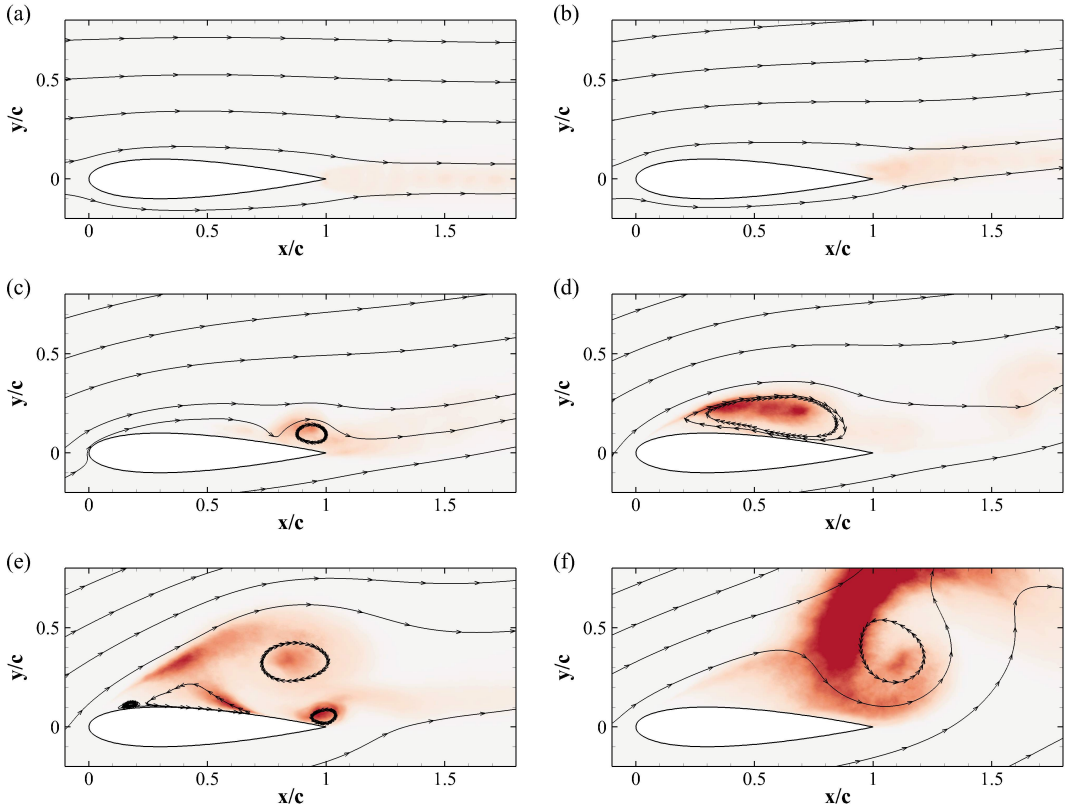

FIGURE 3.13: Contour plots of the ensemble average among solutions with different initial conditions of the turbulent kinetic energy k, averaged in the homogeneous z-direction, at the times showed in Figure (3.10). The contour level go from 0 (white) to $0.15U_\infty^2$ (red).

times sampled in-between. Figure (3.14a) corresponds to the earliest stage at $t = 0.715c/U_\infty$, when the angle of attack is $\alpha = 5^o$. Initially, in panel a, the flow is slightly asymmetric, with two shear layers developing around the mid-chord. In the next two panels (b and c), the flow on the pressure side tends to reattach, while the suction side shows an early separation with the trailing edge shear layer initiating to roll up, and shedding vortices at the trailing edge. At $\alpha = 20^o$ the shear layer rolls-up into a recirculating region that closes at around the mid-chord (Figure (3.14d)). This roll-up process continues (Figure (3.14e-f)) leading to the formation of a large scale vortical structure, i.e., the dynamic stall vortex. As already noticed, while this large scale vortex is formed, no vortices are shed from the trailing edge and an almost straight shear layer is formed. The latter is displaced towards the suction side and distorted by the clock-wise rotation of the dynamic stall vortex (Figure (3.14g)), causing its fast roll-up (Figure (3.14h)). The newly generated trailing edge vortex pushes the dynamic stall vortex upwards causing its detachment from the aerofoil while it grows in size (Figure (3.14i)). Also the

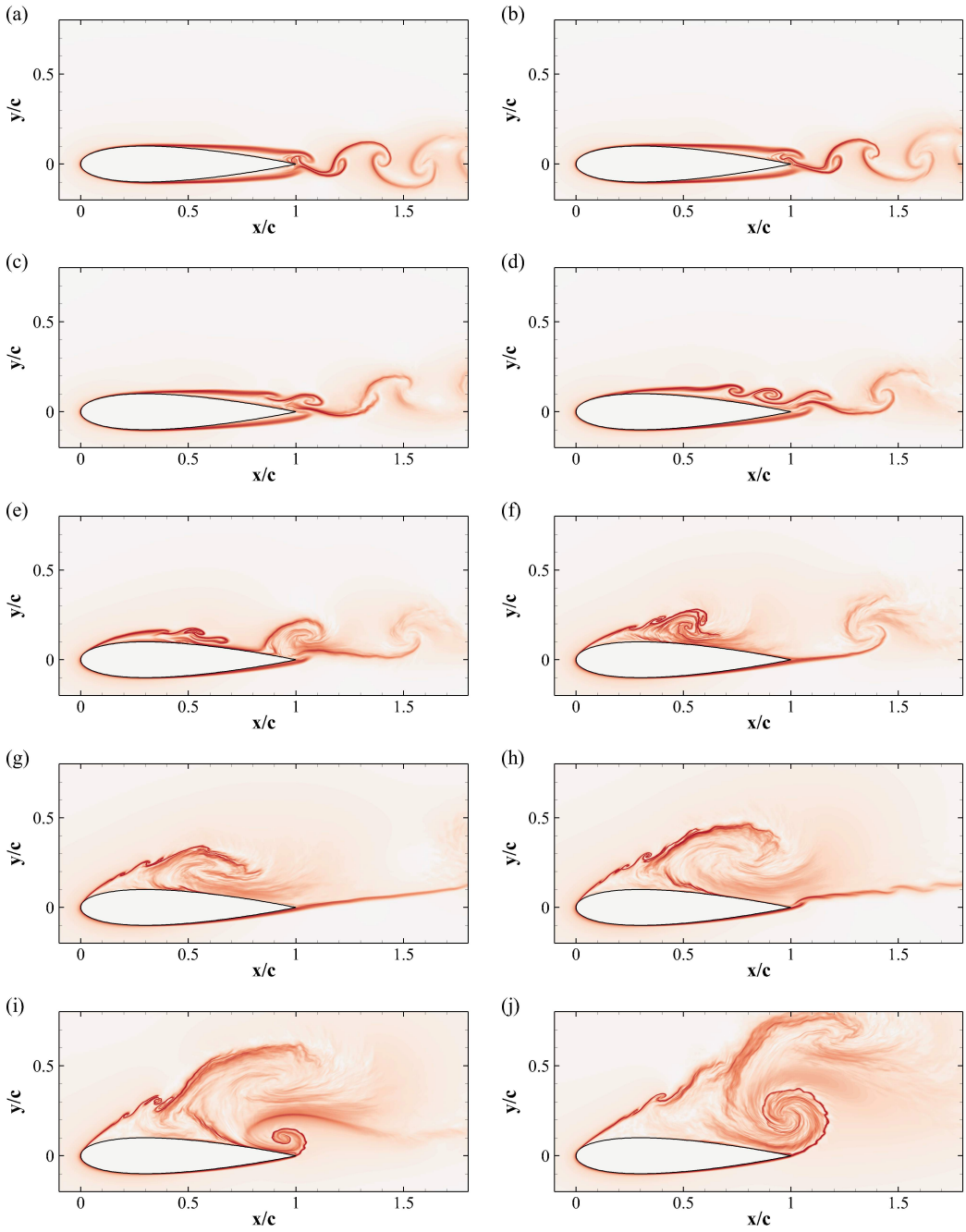

FIGURE 3.14: Contour plot of the FTLE σ^T. Time increases from left to right and from top to bottom, with a sampling time interval of $\Delta t = 0.715c/U_\infty$. The initial time (a) corresponds to $\alpha = 5^o$. The contour levels go from 0 (white) to $7U_\infty/c$ (red).

leading edge shear layer is influenced by the presence of the trailing edge vortex forming a larger angle with the chord. When the trailing edge vortex is shed, the leading edge shear layer moves again closer to the aerofoil (Figure (3.14j))

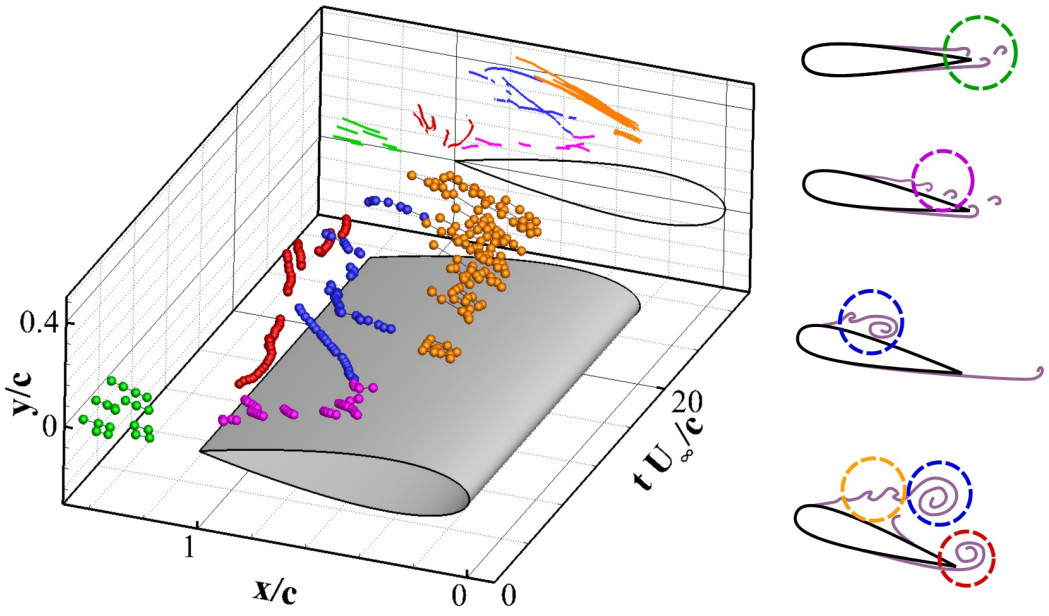

FIGURE 3.15: Vortices positions as a function of time, and sketch of the main events occurring during the dynamic stall.

and starts to roll-up forming a new vortex. This cycle is repeated for a few more times while the intensity of the vortex decays.

To better track the movement of the large scale coherent structures, we have also performed a supplementary vortex eduction study and tracked the cores of the vortices identified using the criterion proposed by Kida and Miura [51]. This methodology defines vortex cores in a two dimensional setting by checking on the correspondence of a local pressure minima and the verification of a swirl condition. In particular, the criterion on the swirl reads as $\mathcal{S} < 0$, where $\mathcal{S}$ is the discriminant of the velocity gradient tensor in the plane, i.e., $\mathcal{S} = (\partial u/\partial x - \partial v/\partial y)^2/4 + \partial u/\partial y\, \partial v/\partial x$. To eliminate the noise induced by very low intensity vortices, we have pre-filtered all the vorticity contributions with span-wise vorticity values lower than $0.01 U_\infty/c$. The evolution of the vortices trajectories, obtained by joining the space locations verifying the two criteria, are plotted in Figure (3.15). The vortices are classified into five groups, marked with different colors. At initial times, vortices are shed only at the trailing-edge (green), but as the separation point moves upstream (Figure (3.12)), vortices start also to be shed from the suction side of the aerofoil at increasingly up-stream locations (magenta). Later, at $t \approx 4c/U_\infty$, the vortices at mid-chord start to merge and the dynamic stall vortex is formed (blue). The dynamic stall vortex first remains almost stationary in its position while it is formed, while later on it is convected downstream with a phase velocity of about $0.25 U_\infty$. As the latter approaches the end of the aerofoil,

the trailing edge vortex is generated (red). This newly formed vortex is first attracted towards the dynamic stall vortex upstream, and, when it is fully formed moves away from the aerofoil surface. Meanwhile, the leading edge shear layer keeps shedding vortices (yellow) which merge into other large scale structures.

Chapter 4

Control of the flow around an aerofoil at high angle of attack

4.1 Introduction

The control of flow separation in wings at high angle of attack has been the focus of many research activities in the past. In particular, a number of biomimetic methodologies for separation control on wings in highly loaded conditions have been inspired by observing the flight or swimming characteristics of certain birds and fish (see [8, 10, 24, 3]). In particular, the idea of reproducing the pop-up of birds feathers for stall delay and control is becoming increasingly popular because of its passive but still self-adaptive character: the feathers lift up is believed to be induced by the back-flow occurring when the flow separates as a consequence of the increased angle of attack (see [10, 12, 21]).

The experimental results reported by Schatz et al. [84] show that the use of self deploying flexible flaps, mounted on the suction side of a wing (HQ17 aerofoil), can deliver an increase in lift of about 10% in nominally stalled conditions at a chord Reynolds number, $Re_c \simeq 10^6$ ($Re_c = U_\infty c/\nu$ is the Reynolds number based on the magnitude of the free stream velocity U_∞ and the aerofoil chord c). More recent experiments by Schluter [85] have also studied the effectiveness of an adaptive passive flap on a SD8020 aerofoil at moderate Reynolds number ($Re_c = 3 - 4 \times 10^4$) showing that its use promotes a lift increase in near stall conditions. Wang and Schluter [95] have extended the previous analysis to genuinely three-dimensional conditions considering the effects of a passive flap on a wing of finite span with the same aerofoil section. They found that the flap still deliver a substantial lift benefit if extending over the 80% of the wingspan leaving the tip clear. They also observed that the position and the length of the flap leading to improved aerodynamic performances were independent of the three dimensional character of the flow field. [9] have extensively investigated the effects of wing mounted movable flaps in a series of wind tunnel experiments.

Their results indicate that adaptive flaps show good aerodynamic performances on wings with a large aspect ratio by successfully suppressing flow separation that develops gradually upstream from the trailing edge. Traub and Jaybush [90] have systematically evaluated the effect of several self-actuated $3D$ spoiler geometries using wind tunnel experiments at $Re_c = 2.25 \times 10^5$ on a SD7062 profile. The best results, in terms of largest lift increase in quasi stalled conditions, were obtained when considering a square slotted spoiler. Bramesfeld and Maughmer [12] explored the effect of small, movable tabs mounted on the suction side of a S824 aerofoil in a low-speed wind tunnel experiment conducted at $Re_c \simeq 10^6$. From the surface pressure distributions they discovered that the effectors act as pressure dams that reduce the adverse effects of the separation, allowing higher pressures upstream of their location. Johnston et al. ([47] and [46]) made a comparison of the effectiveness of free-moving and fixed flaps mounted at different deployment angles over an angle of attack range from 12^o to 20^o, and found a similar behaviour in term of lift, with the maximum lift obtained for deployment angle less than 60^o. However, they found that the fixed flap produces more drag than the free-moving one. Recently, Bruecker and Weidner [17] used flexible flaps to delay the dynamic stall lift breakdown of a NACA0020 wing at moderate Reynolds number (i.e., $Re_c = 7.7 \times 10^5$) in ramp-up motion ($\alpha_0 = 0$ and $\alpha_s = 20^o$). The authors also offer a mechanistic explanation of the stall delay that would be due to a reduction of the backflow, and by a re-organisation of the shear layer roll-up process. In turns, the modified roll-up pattern would cause a delay in the onset of the non-linear growth of the shear layer via a mode-locking of the fundamental instability mode with the motion of the flaps. In disagreement with the majority of the research community, Kernstine et al. [50] found that the highest increase in lift, on separation onset, was obtained with a flap mounted in the first half of a NACA2412 aerofoil, slightly downstream of the leading edge. Very recently another parametric study on the geometry and location of the flap was performed by Altman and Allemand [4]. Their experiments could not confirm the best configuration suggested by Kernstine et al. [50]. More in general, the authors conjecture that it might not be possible to design a universal flap configuration improving post-stall performances.

Apart from the aerodynamic improvements offered by adaptive flaps in stall conditions, the use of similar devices has also been explored as a method for reducing structural vibrations in aerofoils. Liu et al. [60] and Montefort et al. [66] have investigated the effects of a single flexible, polymeric rectangular flap and of an array of small rectangular polymeric flaplets attached near the leading edge on the upper wing surface, considering a NACA0012 aerofoil and a flat-plate. They found that by manipulating the unsteady structure of the flow, these devices were able to reduce significantly wing vibrations particularly near the dominant first torsional mode.

The present contribution will just focus on the impact that self-adaptive very thin flaps have on the flow field structure around a wing at high angle of attack.

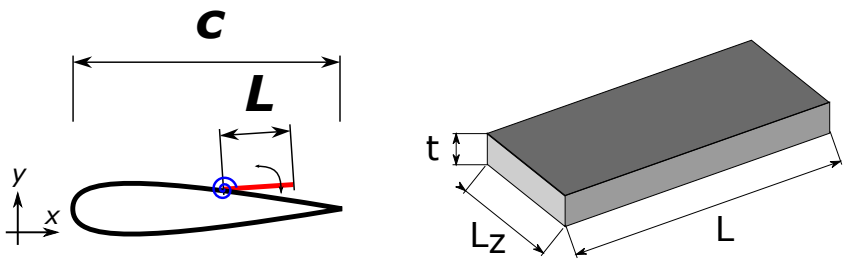

FIGURE 4.1: (a) Sketch of the flap hinged on the suction side of the aerofoil. (b) 3D sketch of the flap.

In particular, the possibility of controlling the flow around a NACA0020 aerofoil using passive, self-adaptive, almost zero-thickness flaps attached to the suction side of the aerofoil will be explored performing a series of Direct Numerical Simulation. After having reported the results of a preliminary parametric study meant to bound the characteristics of the best performing geometries and locations, the attention will move on a detailed analysis of the three-dimensional flow field generated by the wing at $\alpha = 20^o$ degrees when a quasi optimal flaplet is mounted on its suction side at $Re_c = 2 \times 10^5$. By carrying out an in-depth analysis of flow fields generated by direct numerical simulations, we will characterise the main effects induced by the presence of the flap and we will also propose a conceptual explanation of their effectiveness in delivering aerodynamic benefits in stalled configurations.

4.2 Fluid-flap interaction model

Figure (4.1a) shows the configuration that we have analysed in this study, it comprises a NACA0020 aerofoil with a rigid, very thin (in the order of the grid size) flaplet of length L mounted on the wing suction side. The flap is hinged to the surface via a torsional spring that constraints its motion to take place on the $x-y$ plane. The evolution of the flap angular displacement, $\theta(t)$ can be modeled using the canonical second order differential equation:

$$I\ddot{\theta} + C\dot{\theta} + K\theta = \mathcal{T}, \tag{4.1}$$

In equation (4.1), I is the flap moment of inertia with respect to the rotation axis (i.e., $I = mL^2/3$, m being the mass of the flap per unit spanwise length), C is an angular damping factor and K is the spring rotational stiffness (C and K are per unit spanwise length too). Finally, $\mathcal{T}$ is the total torque per unit spanwise length exerted by the fluid forces on the flap. When no damping is considered, a compact way to characterise the physical properties of the flap is based on specifying the spring stiffness K in terms of the moment of inertia I and

its natural frequency f, obtained from the solution of the homogeneous equation associated to Equation (4.1): $K = (2\pi f)^2 I$.

The motion of the flap and its interaction with the surrounding fluid are kept into account using the RKPM immersed boundary method that has been previously described in Section (2.2).

Aside from the flow field time advancement, also the position of the flap needs to be updated. Once the torque in Equation (4.1) is computed by integrating each contribution of the singular forces along the whole flap (obtained using the IB method, see Equation (2.39)), the new angular position $\theta(t)$ is found by integrating Equation (4.1) in time. Finally, all the flap Lagrangian coordinates, and their respective velocities are updated consistently with a rigid body rotation about the hinge. The global time advancement scheme finalises with the solution of a pressure Poisson equation and the final projection of the velocity field onto the consistent divergence free space.

4.3 Baseline flow characterisation

The main features of the flowfield around a NACA0020 aerofoil at 20^o angle of attack and at $Re_c = 2 \times 10^4$ that we wish to manipulate, have been already given in Chapter (3). Here, we will briefly summarise some of the results also introducing some further detail that will allow for a more exhaustive comparison with the flow field obtained when the aerofoil in the same conditions is equipped with a flap. The flow is mainly characterised by a large recirculation zone covering almost the whole suction side as shown in Figure (4.2a) [81]. Moreover, both a secondary counter rotating vortex located by the trailing edge, and another very small recirculation bubble close to the aerofoil maximum thickness can also be observed. All the mentioned spanwise vortices are enclosed within a region bounded by the two shear layers originating at the leading and trailing edges. The leading edge shear layer is induced by the early separation of the free stream laminar flow approaching the wing (see Figure (4.3)) and by the subsequent convective

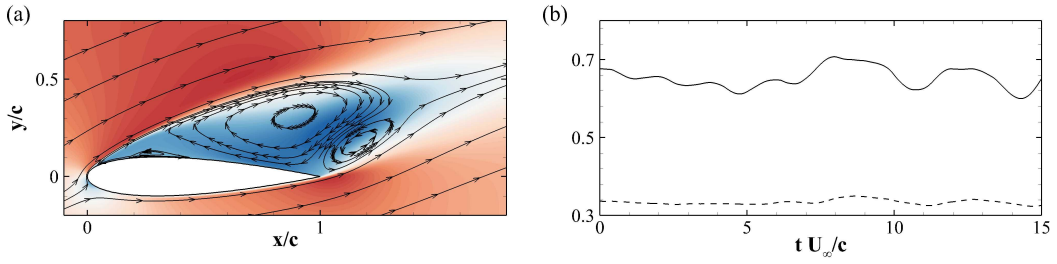

FIGURE 4.2: (a) Contours of mean flow streamwise velocity and streamlines. Contour goes from $-0.3U_\infty$ (blue) to $1.4U_\infty$ (red). (b) Instantaneous lift C_L (solid line) and drag C_D (dashed line) coefficients as a function of time.

Kelvin-Helmholtz (KH) instability that determines its downstream development eventually leading to turbulent transition. A similar behaviour is observed for the trailing edge shear layer that undergoes a KH instability too with a consequent roll up responsible for the formation of the trailing edge vortex street (Figure (4.3)). Further downstream, past the aerofoil, a large wake is formed by the joint contribution of the vorticity generated from both the leading and trailing edges. The uneven vorticity contributions from the two layers is ultimately responsible for the lack of symmetry characterising the wake topology. The global effect of the wake unsteadiness can be evinced from Figure (4.2b) showing the time evolutions of the lift and drag coefficients obtained by integrating the wall pressure and the shear stress at each time step (mean values: $C_L = 0.64$ and $C_D = 0.35$). From the figure, one can observe the presence of a dominant oscillation period clearly associated to the alternating vortex shedding in the wake, with a corresponding non dimensional frequency, in terms of Strouhal number, equal to $St = f_s c/U_\infty \approx 0.534$ [81]. The unsteady behaviour of the spanwise vorticity field, determined by the shear layers instabilities and by the mutual interaction of the vortices embedded in the wake, is the ultimate responsible of the aerodynamic response of the aerofoil to stalled conditions. For this reason, any control strategy that aims at an overall improvement of the aerodynamic efficiency must tackle the direct manipulation of the vorticity field and its unsteadiness. Along this line of thought, this work investigates on the possibility of controlling the vorticity field generated by an aerofoil at high angle of attack using a self adaptive flaplet mounted on its suction side. In particular, the objective is to find a configuration that palliates the detrimental effects of stall by producing

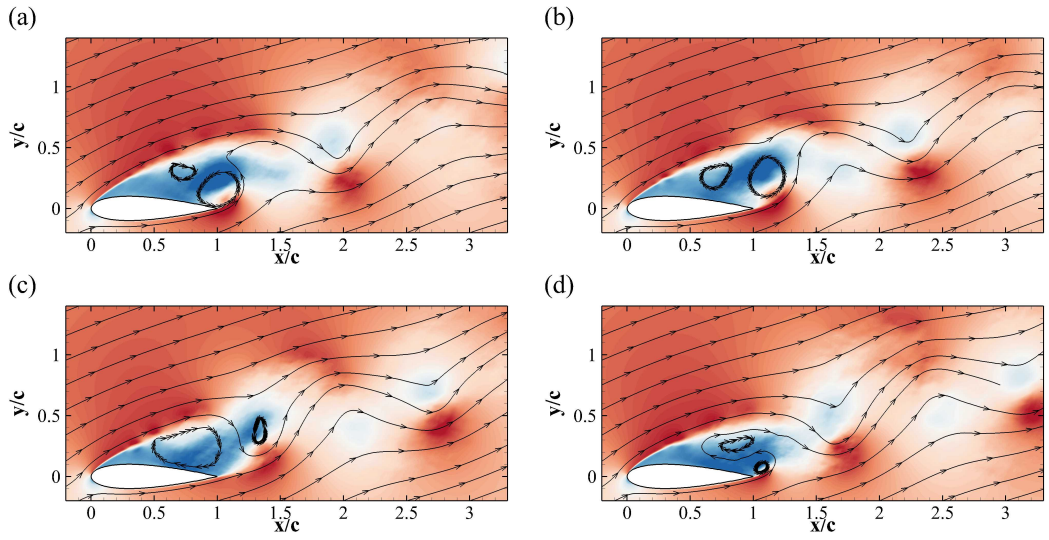

FIGURE 4.3: Contours of instantaneous flow streamwise velocity and streamlines. Contour goes from $-0.3U_\infty$ (blue) to $1.4U_\infty$ (red), and the snapshots cover a full shedding period of $1.87c/U_\infty$.

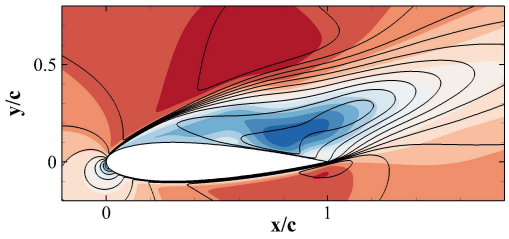

FIGURE 4.4: Contours of the mean flow x-component velocity u. The colour contour is used for the $2D$ case, and goes from $-0.4U_\infty$ (blue) to $1.2U_\infty$ (red), while the contour lines (with the same levels separated by $0.6U_\infty$) is used for the $3D$ case.

increased lift. To pursue such an objective, a parametric study covering a fully three-dimensional flow at the targeted chord Reynolds number would be computationally unrealistic. For this reason, a preliminary study on a low Reynolds number, fully laminar, two-dimensional flow has been carried out with the objective of bounding the parametric range that needs to be explored for achieving a good flap design in a realistic three dimensional scenario. Before describing the initial two-dimensional parametric study, a comparison between the two baseline cases (i.e., fully 3D case at higher Reynolds number versus the laminar case at lower Reynolds numbers) will be introduced to provide a conceptual justification of the procedure that has been followed. Figure (4.4) compares the character of the mean three dimensional $x-$wise velocity field at $Re_c = 2 \times 10^4$ and $\alpha = 20^o$

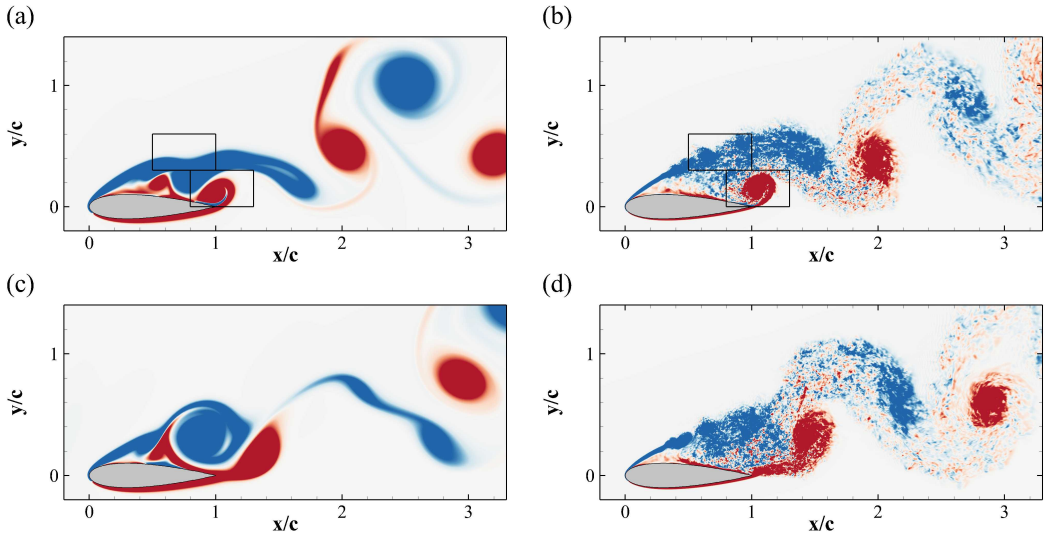

FIGURE 4.5: Contours of the instantaneous spanwise component of vorticity ω_z, corresponding with the minimum (top) and maximum (bottom) lift coefficients over one shedding period for the 2D (left) and 3D (right) cases. Blue lines used for negative, clockwise vorticity, red ones for positive values ($\pm 5U_\infty/c$).

with the two dimensional field obtained at the same angle of attack but at much lower Reynolds number, i.e., $Re_c = 2 \times 10^3$. The two velocity fields show similar qualitative features: large recirculating regions of comparable magnitude covering the whole suction side of the aerofoil (i.e., the sizes of the recirculating regions are $0.5c$ and $0.35c$ in the $2D$ and $3D$ case, respectively). In both cases, the flow separates at the leading edge ($x_s \approx 0.025$) reattaching at $x_r \approx 0.9$ in the $2D$ case, while staying detached along all the rest of the suction side for the $3D$ case. The unsteadiness of both the $2D$ and the $3D$ stalled cases is mainly determined by the presence, the interaction and the shedding of the two large counter rotating vortices that characterise the region above the aerofoil (see Figure (4.5)). The dynamic of these two large vortices governing the lift oscillations, is mainly of $2D$, laminar nature and basically involves only the interaction of the very large coherent structures embedded in the flow. Although the quantitative differences between the two-dimensional and the three-dimensional case are not negligible, the dominating effects and the events sequencing appear to be qualitatively similar. Moreover, since the self adaptive flap that we will use extends over the whole span of the wing, no significant 3D effects will be introduced by its presence as the flaplet will mainly interfere with the largest integral scales of the flow which are intrinsically two-dimensional in character.

4.4 Flaplet design in 2D

Motivated by the aforementioned considerations, we have initially focused on the geometrical properties (i.e., size and location) and the flap dynamic response (i.e., its natural frequency) that deliver an optimal condition in a two dimensional, fully laminar flow at $\alpha = 20^o$. Here, we define an optimal condition as the one that delivers the highest lift coefficient C_L, preserving or improving the aerodynamic efficiency $E = C_L/C_D$. We have started our analysis by considering the low Reynolds number (i.e., $Re_c = 2 \times 10^3$), $2D$ flow over a NACA0020 aerofoil at $\alpha = 20^o$ without any added flap. Figure (4.6) shows the time evolution of the lift

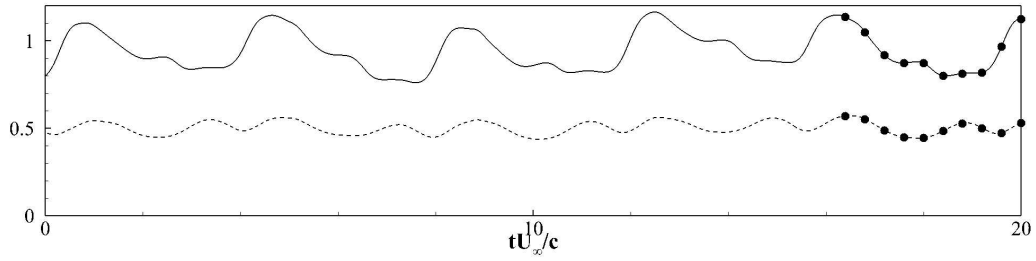

FIGURE 4.6: Instantaneous lift C_L (solid line) and drag C_D (dashed line) coefficients as a function of time. The dots indicate the selected time snapshots shown in Figure (4.7).

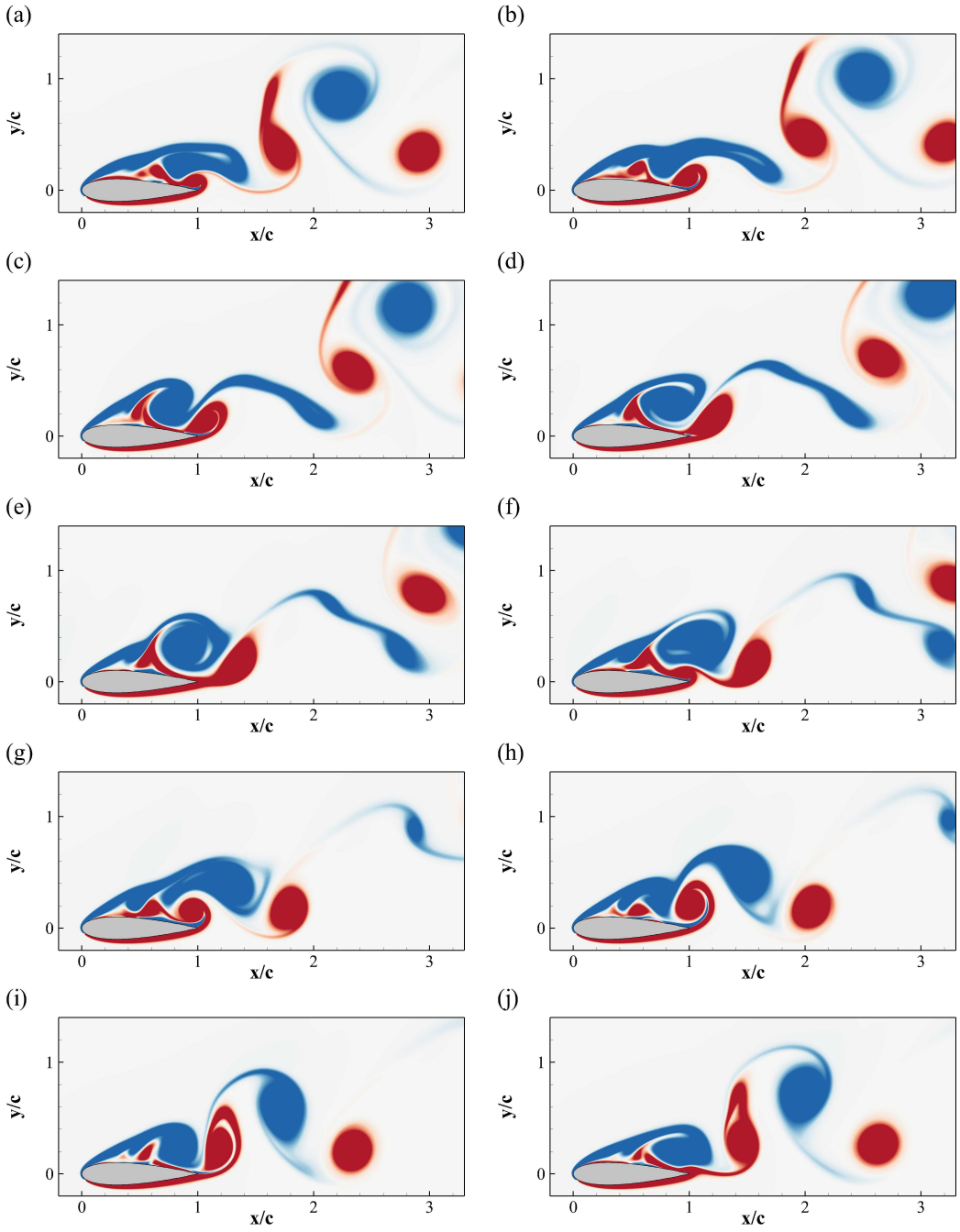

FIGURE 4.7: Contours of the instantaneous spanwise component of vorticity ω_z during two shedding cycles (corresponding to $3.247c/U_\infty$ non-dimensional time units). The snapshots correspond with the time instants marked in Figure (4.6). Blue negative (clockwise) vorticity, red positive (counter clockwise) in the range $\pm 5U_\infty/c$.

and drag coefficients for the baseline configuration. Both coefficients are characterised by periodic oscillations: every period of lift coefficient corresponds to the

TABLE 4.1: Flap configurations considered in the 2D parametric study.

Case	f/f_0	L/c	x_F/c	$K \times 10^3$	$I \times 10^3$	C_L	C_D	E
Ref	–	–	–	–	–	0.9365	0.5024	1.8641
F0.25-L0.10-X0.7	0.25	0.10	0.7	2.3461	3.3333	1.0290	0.5038	2.0424
F0.50-L0.10-X0.7	0.50	0.10	0.7	9.3847	3.3333	0.9023	0.4889	1.8457
F1.00-L0.10-X0.7	1.00	0.10	0.7	37.539	3.3333	0.9804	0.5052	1.9407
F2.00-L0.10-X0.7	2.00	0.10	0.7	150.15	3.3333	0.8815	0.4778	1.8448
F4.00-L0.10-X0.7	4.00	0.10	0.7	600.62	3.3333	0.8519	0.4779	1.7828
F0.25-L0.20-X0.7	0.25	0.20	0.7	9.3847	13.333	0.9324	0.5074	1.8376
F0.50-L0.20-X0.7	0.50	0.20	0.7	37.539	13.333	0.8292	0.4822	1.7196
F1.00-L0.20-X0.7	1.00	0.20	0.7	150.15	13.333	1.2659	0.5572	2.2718
F2.00-L0.20-X0.7	2.00	0.20	0.7	600.62	13.333	0.7800	0.4620	1.6883
F4.00-L0.20-X0.7	4.00	0.20	0.7	2402.5	13.333	0.7805	0.4620	1.6883
F0.25-L0.30-X0.7	0.25	0.30	0.7	21.115	30.000	0.7062	0.4539	1.5556
F0.50-L0.30-X0.7	0.50	0.30	0.7	84.462	30.000	0.8688	0.5140	1.6903
F1.00-L0.30-X0.7	1.00	0.30	0.7	337.85	30.000	0.8511	0.4679	1.8192
F2.00-L0.30-X0.7	2.00	0.30	0.7	1351.4	30.000	0.8538	0.4915	1.7372
F4.00-L0.30-X0.7	4.00	0.30	0.7	5405.6	30.000	0.8260	0.4844	1.7051
F1.00-L0.20-X0.6	1.00	0.20	0.6	150.15	13.333	1.1076	0.5021	1.3871
F1.00-L0.20-X0.8	1.00	0.20	0.8	150.15	13.333	0.6965	0.4424	1.5746

shedding of a vortex, at a shedding frequency equal to $f_s = 0.555U_\infty/c$. The lift coefficient evolution also shows the presence of a lower frequency $f = 0.308U_\infty/c$ (almost half the shedding frequency). The instantaneous vorticity fields ω_z over this two shedding periods are shown in Figure (4.7). The presence of two dominant vortices formed as a consequence of the leading and trailing edge shear layer instabilities characterises all the time series. In particular, their opposite circulations are responsible for the lift and downforce generated by the clockwise rotating vortex (blue), and the counter clockwise rotating one (red), respectively. The first few snapshots of the reported vorticity time series correspond to a maximum lift condition in which the leading edge vortex has already formed while the trailing edge one is rolling up, on the verge of being shed from the aerofoil (Figure (4.7a-e)). The roll up of the trailing edge vortex, corresponds to a decrease in lift that gradually disappears as the vortex is shed into the wake. In the following time instants of the sequence (Figure (4.7f-j)), another pair of vortices is formed and shed away from the aerofoil. However, the newly generated lifting vortex quickly detaches from the wing surface, thus preventing the lift to raise. As the lift vortex is shed into the wake, it starts interacting with the trailing edge vortex that rolls up increasing its size. This interaction energises the trailing edge vortex with a consequent further decrease in lift, and with an impact in determining the structure of the near-wake (see Figure (4.7e) and Figure (4.7j)). The final snapshots of the series, correspond to the end of the cycle with the generation of a new lifting vortex leading to the beginning of a new cycle.

Next, we have proceeded to perform a parametric study on the aerodynamic

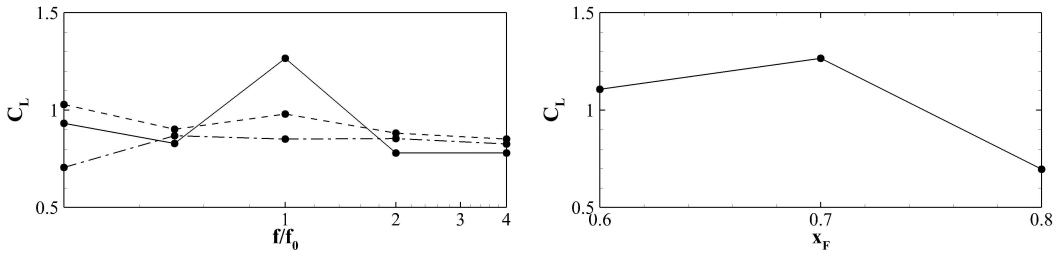

FIGURE 4.8: Mean lift C_L as a function of (a) the spring natural frequency f and of (b) the position of the hinge x_F. The dashed, solid and dash-dot lines are used for the cases with $L = 0.1c$, $L = 0.2c$ and $L = 0.3c$, respectively.

effects of the flaplet configuration. In particular, the flap reaction to the underlying unsteady flow field can be tuned by acting on various parameters: its length, position, inertia, spring stiffness and damping factor. The outcomes of the analysis conducted by varying the aforementioned parameters are summarised in Table (4.1) reporting some typical variations of the averaged aerodynamic coefficients (last three columns) when changing the flaplet characteristics (second to fifth columns). In particular, the length L of the flap was varied between $0.1c$ and $0.3c$, the position of the flap hinge x_F ranged between $0.6c$ and $0.8c$ (measured from the leading edge), the stiffness K of the spring was set such that its natural frequency f was between 1/4th and 4 times the shedding frequency f_0 of the baseline case without flap. The effects of the length and stiffness of the torsional spring on the value of the mean lift coefficient C_L are also reported graphically in Figure (4.8a). An optimum condition (i.e., maximum lift increase with respect to the baseline case) is achieved with a flaplet $0.2c$ long, resonating with the shedding frequency (flap natural frequency equal to the shedding one). Except for the cases of flaplets of very low natural frequency, if the latter doesn't match the baseline flow shedding frequency, the lift coefficient turns out to be almost unaffected by the length of the flap. On the other hand, when considering resonating conditions, the maximum lift and efficiency are achieved using a flaplet $L = 0.2c$ long, a size roughly corresponding to half the dimensions of the recirculation region. Figure (4.8b) shows how the lift coefficient changes as a function of the hinge position when considering a $L = 0.2c$ long flaplet in resonating conditions. The optimal position, in terms of maximum lift, is at about $0.7c$, where, when unlifted, the flaplet end almost reaches the trailing edge.

In summary, when a low Reynolds number, $2D$ case at an angle of attack of $\alpha = 20^o$ is considered, the flaplet configuration that maximises the mean lift features a length of $0.2c$, a hinge location at $0.7c$ and a spring stiffness leading to a flaplet natural frequency matching the shedding one. For this specific flow condition and with the mentioned configuration, the flaplet interferes actively with the unsteady vorticity field delivering a 20% increase in the average aerodynamic efficiency. The corresponding time variations of the lift C_L and drag C_D coeffi-

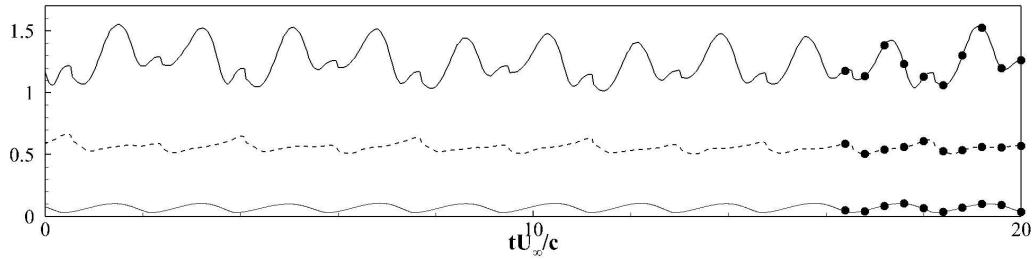

FIGURE 4.9: Optimal flaplet configuration: instantaneous lift C_L (solid line) and drag C_D (dashed line) coefficients as a function of time. The thin solid line represents the elevation y of the tip of the flap. The set of bullets on the graphs indicates the instants in time where the vorticity snapshots have been sampled, see Figure (4.10).

cients are reported in Figure (4.9) together with the elevation y of the tip of the flap from the aerofoil. The time averaged C_L is 35% higher than the case without flap (see Figure (4.6)), while the shedding frequency remains unchanged (i.e., $f_s = 0.555U_\infty/c$). However, differently from the baseline case, the presence of the flap seems to regularise the shedding pattern, with all the lift extrema attaining almost the same value at each shedding period (see Figure (4.6)). Figure (4.10) shows the spanwise vorticity over two shedding cycles at the times marked in Figure (4.9a). In the initial snapshots (Figure (4.10a-b)), when the flap is almost laying on the aerofoil surface, a first vortex detaches from the trailing edge. Subsequently, (Figure (4.10c-d)) the flap reaches its maximum elevation while a large lifting vortex is formed above the aerofoil inducing a maximum lift force. The cycle is closed by the formation of a new trailing edge vortex (Figure (4.10e-f)). The mutual interaction of the flow field with the flaplet has a strong impact on the shedding process and therefore with the structure of the wake (see Figure (4.10f) and Figure (4.10j)). The importance of the interaction is further stressed by the high correlation between the lift oscillations and the flap motion (correlation coefficient is ≈ 0.6), and in particular by the fact that the maximum lift is reached when the flap is almost at its maximum elevation (the time lag between the two functions is $\approx 0.2c/U_\infty$).

As a further measure of the effect of the flaplet on the vorticity field, we have quantified the circulations of the velocity field along two closed rectangular loops bounding the lifting vortex ($x \in [0.5, 1.0]$, $y \in [0.3, 0.6]$), and the trailing edge vortex ($x \in [0.8, 1.3]$, $y \in [0.0, 0.3]$), respectively (see Figure (4.5)). The circulation of the leading edge vortex which is responsible for the lift generation is only slightly increased by the presence of the flaplet (i.e., $\approx 3\%$), while the circulation of the trailing edge vortex, responsible for the generation of the downforce, is substantially reduced by a factor of $\approx 20\%$. Therefore, the increase in the average lift induced by the presence of the flaplet is mainly related with the reduction of the downward force induced by the trailing edge vortex.

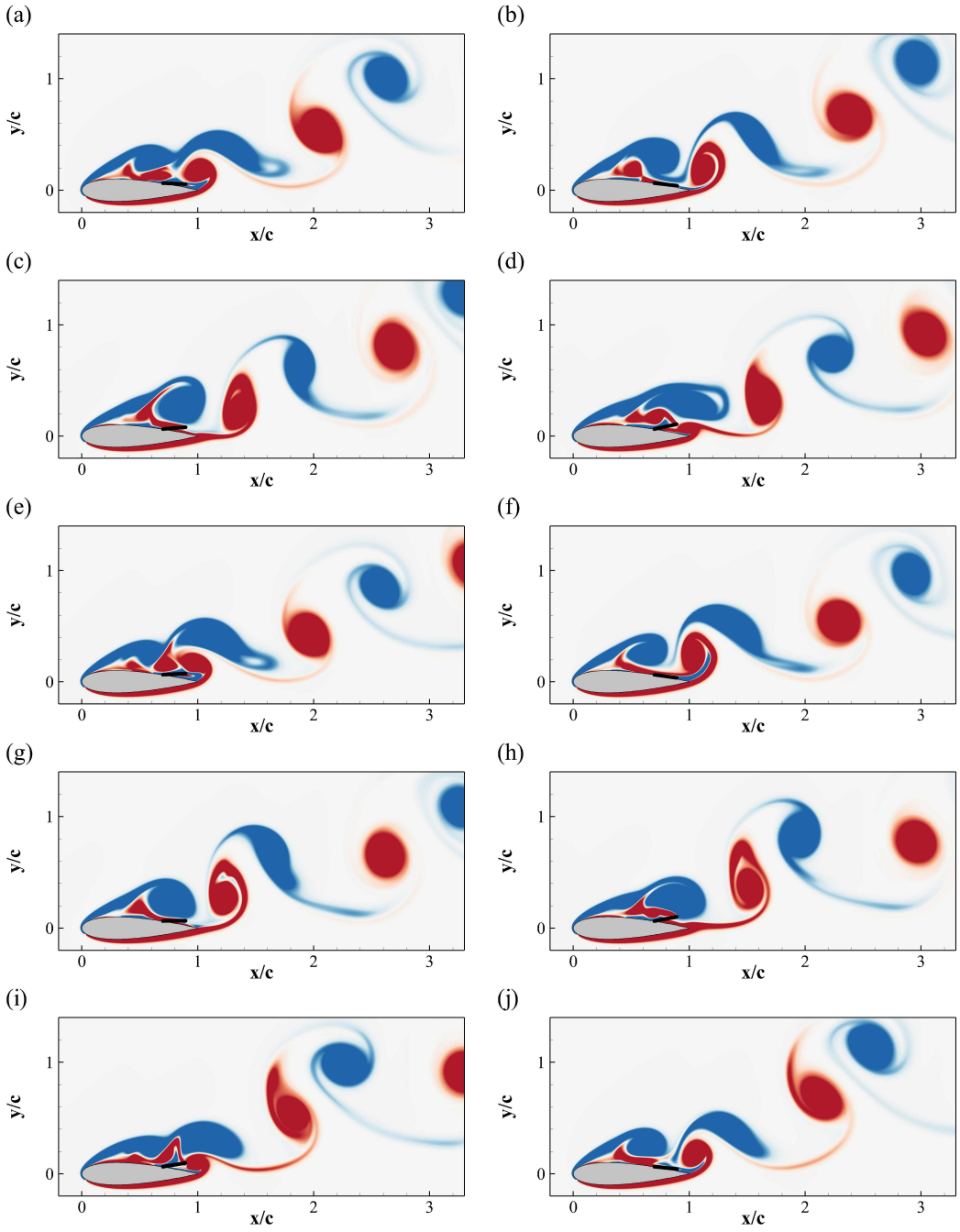

FIGURE 4.10: Optimal flaplet configuration: contours of the instantaneous spanwise vorticity ω_z, at the time instants highlighted in Figure (4.9). Blue negative vorticity (clockwise), red positive ($\pm 5U_\infty/c$).

This preliminary study conducted in a simplified $2D$, laminar scenario has allowed to determine a point in the parameters space leading to a maximum increase in both lift and aerodynamic efficiency. The analysis has also characterised

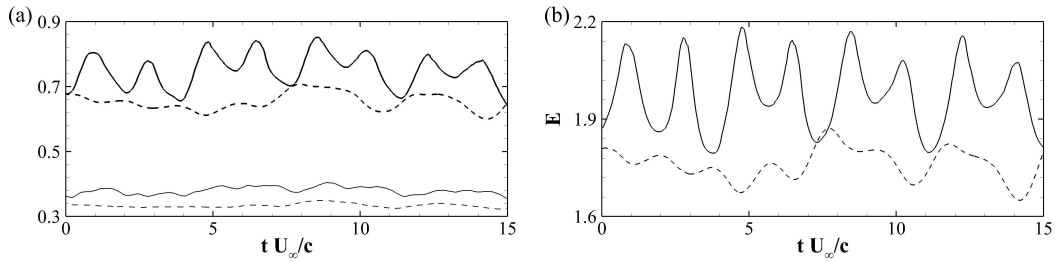

FIGURE 4.11: (a) Lift C_L (black) and drag C_D (gray) coefficients as a function of time. (b) Evolution of the aerodynamic efficiency $E = C_L/C_D$. Solid lines are used for the aerofoil with flap, while dashed lines for the reference values.

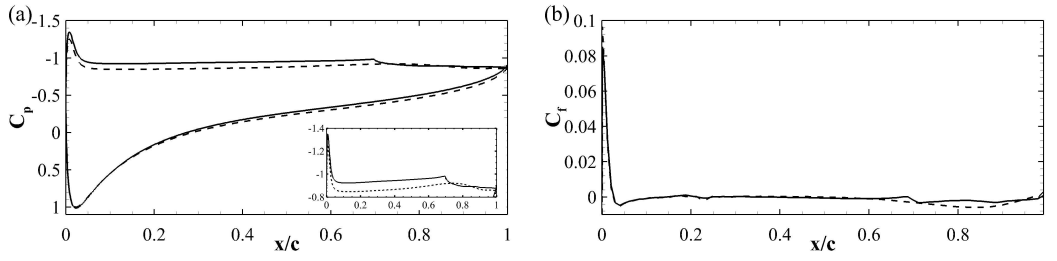

FIGURE 4.12: (a) Pressure C_P and (b) friction C_f coefficient distributions. Solid and dashed lines are used for the aerofoil with and without flap, respectively.

the features of the unsteady vorticity fields that develops when the optimal flap is used. The validity of our conjecture about the possibility of extending the results obtained with a simplified $2D$ scenario to a realistic $3D$ one will be discussed next.

4.5 Effect of the adaptive flaplet on a $3D$ aerofoil

We now compare the three-dimensional flow fields around a NACA0020 at an angle of incidence of 20^o and at $Re_c = 2 \times 10^4$, obtained when considering the unmodified aerofoil and when equipping the wing with a flaplet extending along its whole span, and featuring the optimal configuration discussed in the previous section (flap length $L = 0.2c$, hinge location at $x = 0.7c$). Furthermore, inspired by the two-dimensional results, the stiffness of the torsional spring has been set to $K = 0.150$ leading to a natural frequency that matches the shedding one of the unmodified aerofoil.

Figure (4.11a) compares the time evolution of the lift and drag coefficients of the reference case versus the ones obtained when using the flaplet. Their time averaged values are $C_L = 0.64$ and $C_D = 0.35$, for the baseline case, increasing to $C_L = 0.74$ and $C_D = 0.37$ with the flap, thus obtaining a 16% improvement in lift and a slightly augmented drag (6%). The aerodynamic efficiency, $E = C_L/C_D$

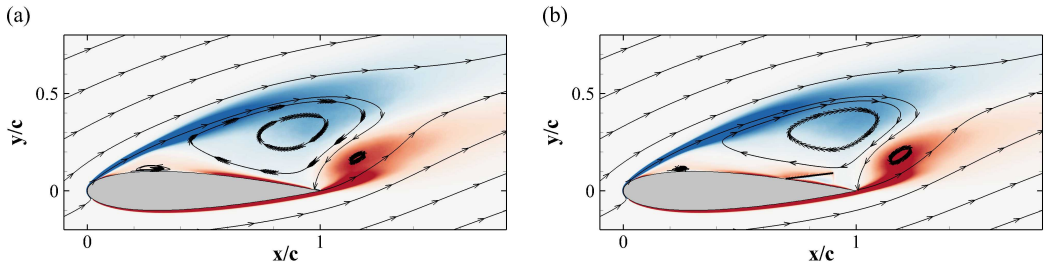

FIGURE 4.13: Contours of the mean (i.e., time and z-averaged) spanwise component of vorticity ω_z and mean streamlines of the NACA 0020 aerofoil at $\alpha = 20^o$ and $Re_c = 2 \times 10^4$. Left panel (a): results for the baseline wing; right panel (b): wing equipped with a flaplet ($L = 0.2c$, $x_F = 0.7c$, $K = 0.150$). Blue negative vorticity (clockwise), red positive ($\pm 7U_\infty/c$).

is reported in Figure (4.11b) showing a net improvement when the flaplet is introduced with a mean efficiency growth from 1.8 (baseline case) to 2.0 (i.e., 11% increase with the flap). This improvement is in good agreement with the experimental results reported by Schatz et al. [84]. Furthermore, the time evolution of the aerodynamic coefficients clearly reveals the presence of a dominant frequency that corresponds to the shedding rate of the vortices into the wake. The introduction of the flaplet does not modify the value of the associated Strouhal number $S_t = f_s c/U_\infty$ that remains fixed to $S_t = 0.534$, a value that is almost the same as the one found in the 2D case at lower Reynolds number.

When we compare the mean pressure coefficients C_p of the two configuration, as shown in Figure (4.12a), we notice that the pressure on the suction side of the aerofoil with flap is reduced upstream the flap position, thus generating a higher lift, in agreement with the results by Schatz et al. [84] and Bramesfeld and Maughmer [12], and then increases, downstream the location of its hinge. The friction coefficient C_f, reported in Figure (4.12b), shows that the two aerofoils have a similar friction profile, with an early leading edge separation located at $x \approx 0.025c$ [81], except, in the leading edge peak which is enhanced by 10% in the case with flap.

Next, we analyse the effect of the flaplet on the average fields. We start by comparing the contours of the mean spanwise component of vorticity ω_z in Figure (4.13). The figure shows that both the aerofoils are in a fully stalled condition with a large recirculation zone present on the whole suction side. Another smaller recirculation bubble is visible in both cases at about $0.25c$ from the leading edge, in proximity of the location of the aerofoil maximum thickness. The backflow region with positive vorticity (i.e., red: counter clock wise) on the suction side is clearly reduced when the flap is in use. Moreover, we can also notice that the presence of the flaplet reduces the size of the positive vorticity recirculating region by the trailing edge, also displacing the peak of positive vorticity further downstream, well beyond the trailing edge. More information on

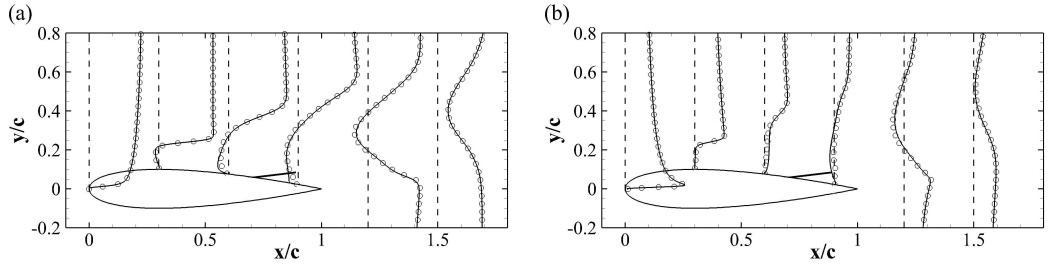

FIGURE 4.14: Mean x-wise (a) and y-wise (b) velocity components profiles over the aerofoil and in the near wake. Lines are used for the aerofoil without flap; symbols refer to aerofoil with flap.

the mean flow can be educed from the velocity profiles in Figure (4.14) where the x and y velocity components are shown. While the mean flow velocity on the pressure side is basically unaffected by the presence of the flaplet, on the suction side the velocity field changes in the region spanned by the flap movement. As compared to the baseline case, upstream of the flap location, at $x = 0.6c$, both velocity components are reduced in amplitude, with a corresponding overall reduction of reversed flow. Downstream of the flap, at $x = 0.9c$, in the region traversed by the flap oscillations, the velocity intensity is reduced because of the no-slip and no-penetration boundary condition on the flap solid surface. Finally, in the near wake region, the velocity defect is slightly enhanced in the case with flap.

The effects of the flaplet on the flow become can be seen when considering the distribution of higher order statistical quantities. Figure (4.15a), shows a comparison of the averaged turbulent kinetic energy $k = 1/2 < u_i' u_i' >$, in the controlled and uncontrolled cases. Consistently with the upstream laminar conditions, the kinetic energy is initially zero for both the aerofoils. Further downstream in the shear layer originated at the leading edge, k starts to grow similarly in both cases. On the other hand, the second shear layer formed past the trailing edge is influenced by the action of the flaplet. Its motion reduces the intensity of the velocity

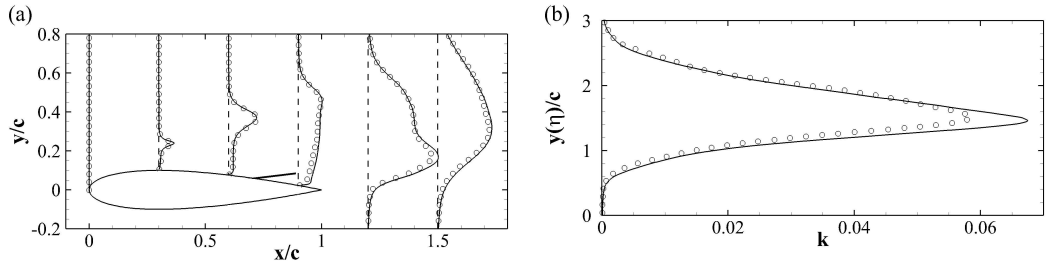

FIGURE 4.15: (a) Mean turbulent kinetic energy profiles over the aerofoil and in the near wake, and (b) further downstream at $x \approx 5.5c$. Lines are used for the aerofoil without flap; symbols refer to aerofoil with flap.

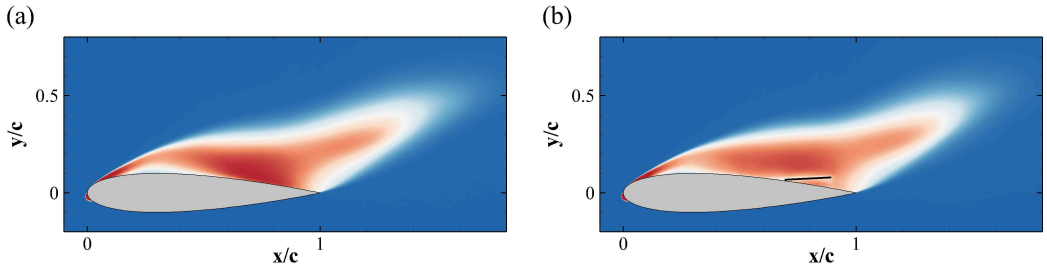

FIGURE 4.16: Intermittency factor $\mathcal{I}_- = \mathcal{P}(u < 0)$ for the reference (a) and flap (b) cases. Contour levels go from blue ($\mathcal{I}_- = 0$) to red ($\mathcal{I}_- = 1$).

fluctuations. Downstream of the aerofoil, the two shear layers merge into the wake where the reduced levels of k, due to the flaplet action, are evident. This is clearly visible from Figure (4.15b) showing the turbulent kinetic energy profile at $x \approx 5.5c$.

As previously mentioned, one of the consequences of the action of the flaplet on the flow field is the reduction in the intensity of the backflow on the aerofoil surface. To quantify this effect, in Figure (4.16) we display the probability of finding a negative streamwise velocity component $\mathcal{P}(u < 0)$ in the two cases. In both situations, this probability is obviously zero in the outer flow where the u velocity is always positive, while its value increases in the recirculating region. In the reference case, the highest probability of backflow corresponds to the region close to the trailing edge, at $x \approx 0.8$. In the case where the flaplet is active, the probability of having backflow is remarkably reduced not only in the region spanned by the flap movement but also upstream of it.

To gain further insight on the effect of the flaplet-flow interaction we have used the classical $\mathcal{Q}$-criterion. Instantaneous $\mathcal{Q}$ iso-surfaces corresponding to the case without and with flaplet are shown in Figure (4.17) and Figure (4.18). From the first figure, it appears that the action of the flap contributes to the reductions of both the backflow and the generation of turbulent structures upstream of its location. From the second figure, it is possible to recognise the principal flow features of the baseline case [81]. These are summarised hereafter to introduce the comparison with the active flaplet case. Initially, the incoming laminar flow separates at the leading edge, forming a shear layer that rolls up into Kelvin-Helmholtz (KH) vortices (see [18], [19], [100], [89] and [1]); this instability, locally, triggers the flow transition to turbulence; further downstream, the turbulent separated region appears to be characterized by fine texture, small-scale eddies, eventually merging into coherent larger structures; finally behind the aerofoil, a large turbulent wake is formed, the dynamics of which are similar to a von Karman vortex street typical of bluff body wakes. In contrast to classical vortex shedding process showing an alternately series of vortices of opposite sign and equal strength, here the wake is highly asymmetric presenting vortices of uneven strength. The loss of symmetry and the irregularity of the vortices pattern is

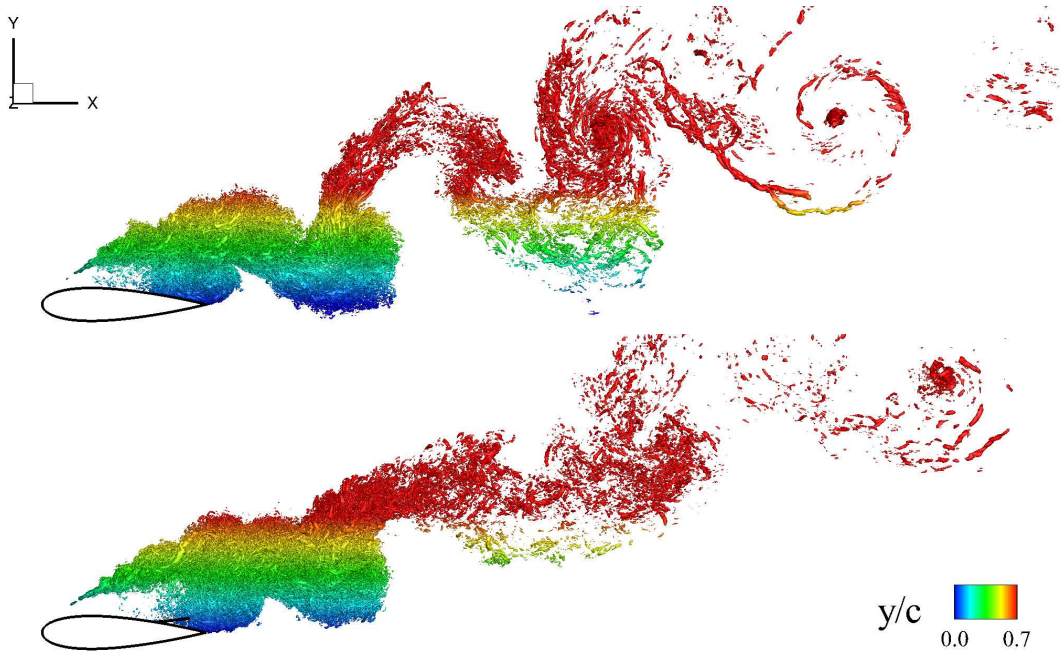

FIGURE 4.17: Visualisation of instantaneous vorticity field by means of $\mathcal{Q}$-iso-surfaces ($\mathcal{Q} = 450U_\infty^2/c^2$) coloured by the y-coordinate (distance from centerline). (a) and (b) are the cases without and with the flap, respectively.

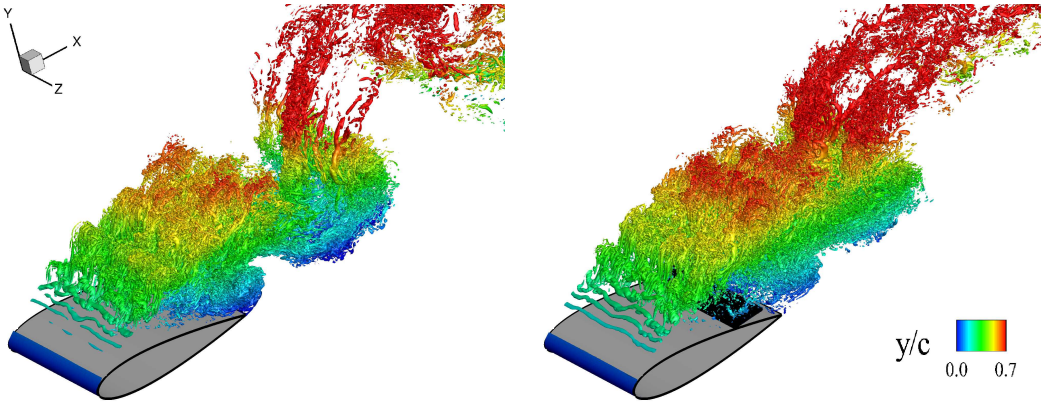

FIGURE 4.18: Visualisation of instantaneous vorticity field by means of $\mathcal{Q}$-iso-surfaces ($\mathcal{Q} = 450U_\infty^2/c^2$) coloured by the y-coordinate (distance from centerline). (a) and (b) are the cases without and with the flap, respectively.

related to the interaction between the two vortex generating mechanisms (see [14] and [13]): the vortices rolling up under the action of the KH leading edge shear layer instability and the street of vortices shedding from the trailing edge. The main features of this flow process, largely present also in the $2D$, laminar case, remain practically unaffected by the presence of the flap, except in the leading edge area, where the instability of the KH rollers is displaced downstream.

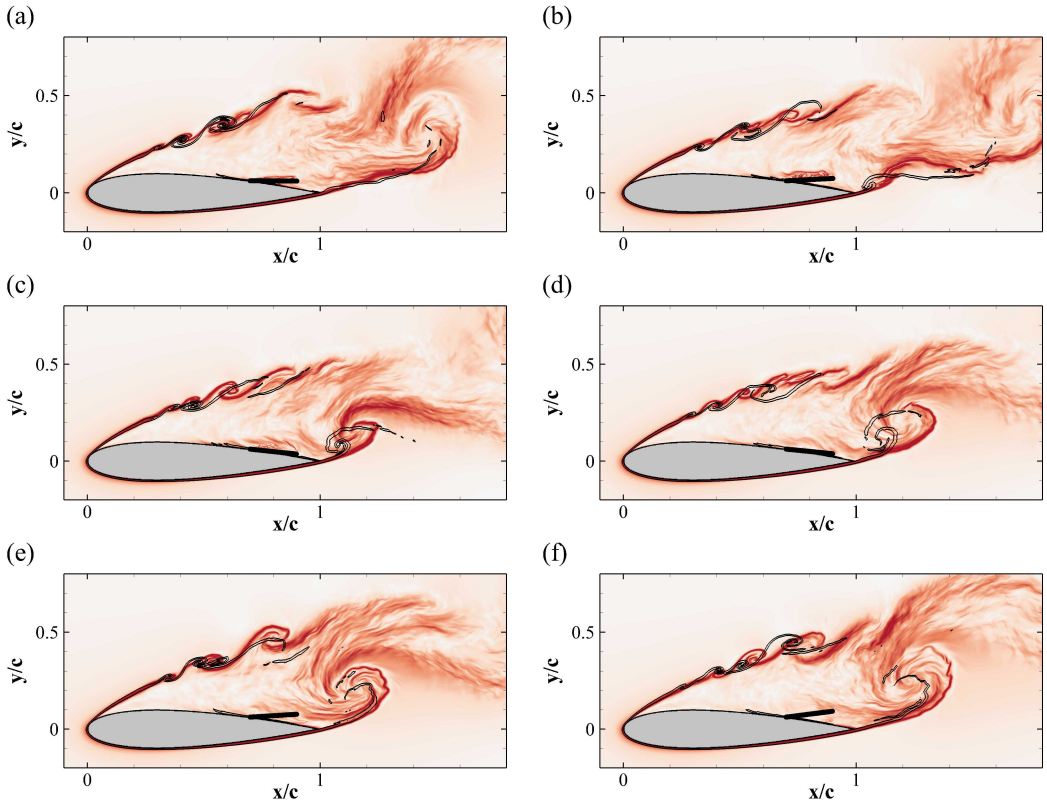

FIGURE 4.19: Istantaneous contour plot of the FTLE σ^T during a shedding period for the case with flap. The contour levels go from 0 (white) to $7U_\infty/c$ (red). The black contour lines are used for the baseline case without flap.

This feature can be observed by referring to Figure (4.19), where the Finite Time Lyapunov Exponent is used. Figure (4.19a) is the beginning of the shedding cycle, with no vortex at the trailing edge, and the leading edge shear layer rolling up under the action of a KH instability. Figure (4.19b-e) show how the trailing edge shear layer undergoes a KH instability also. The shear layer rolls up inducing the generation of a trailing edge vortex, which eventually detaches (Figure (4.19f)). It is apparent that the rolling-up of the leading edge shear layer in the case with flap (colour contours), takes place further downstream as compared to the baseline case (line contour). Also the previously described trailing edge vortex downstream displacement is evident from this figures.

By looking at the time variation of the vorticity field another important effect of the interaction between the flow and the flaplet emerges. In particular, in Figure (4.20) and Figure (4.21), we compare the evolution of the spanwise vorticity ω_z over two shedding cycles for both the cases, with and without flap. The sequence of the reference case starts with the lifting vortex recently shed, and the trailing edge vortex being freshly formed and ready to be shed (Figure (4.20a)). As the lifting vortex detaches, another one is generated above

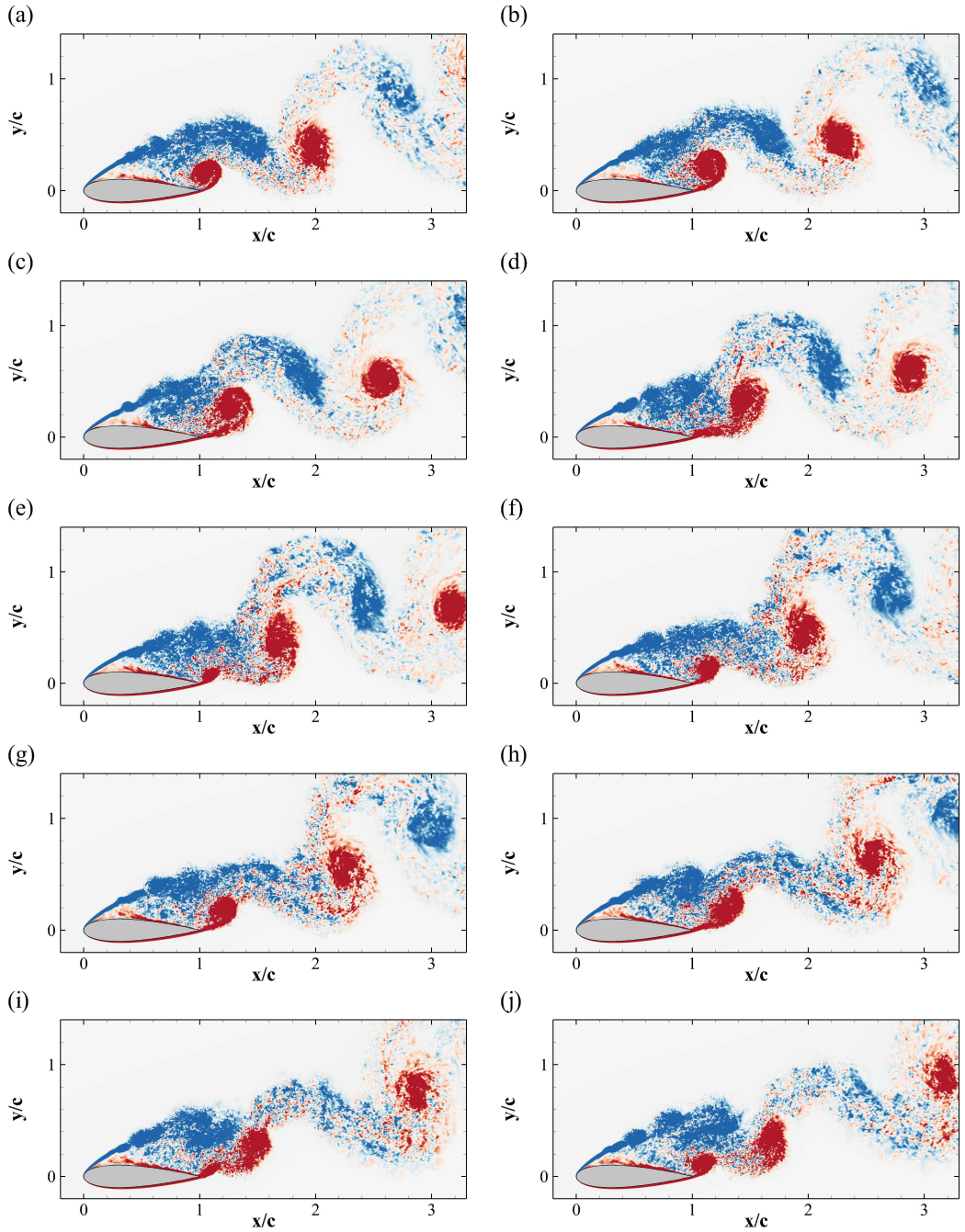

FIGURE 4.20: Baseline aerofoil: contours of the instantaneous spanwise component of vorticity ω_z, over two shedding periods. Blue negative vorticity (i.e., clockwise), red positive ($\pm 5U_\infty/c$).

the aerofoil (see Figure (4.20b-d)), and eventually shed into the wake at a later stage (see Figure (4.20e)) when the formation of the next trailing edge vortex takes place. The latter does not undergo a full evolution as it clearly appears from

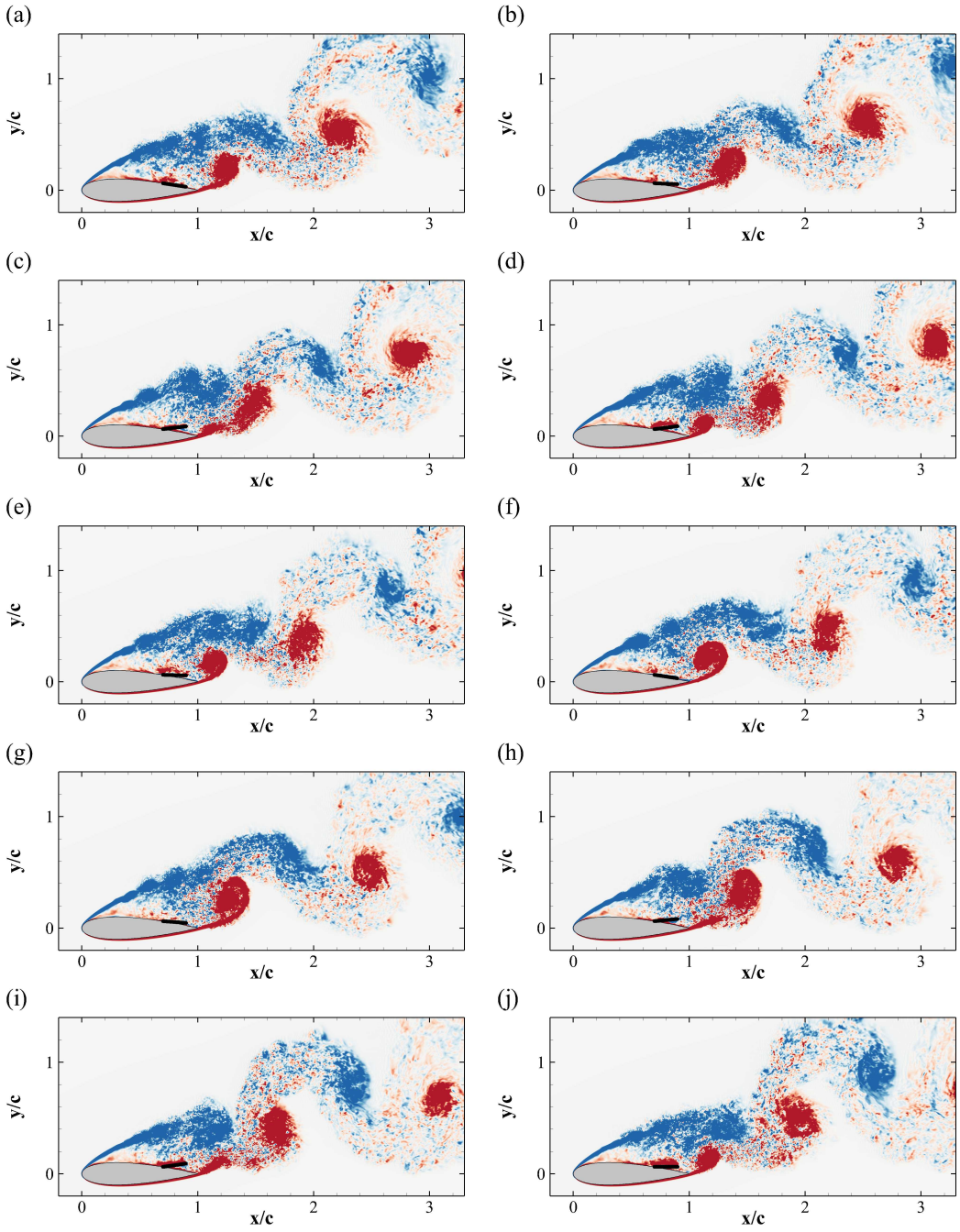

FIGURE 4.21: Aerofoil equipped with the flaplet: contours of the instantaneous spanwise component of vorticity ω_z, over a time of two shedding periods. Contours as in figure 4.20

the following snapshots. In the following shedding cycle (see Figure (4.20f-j)) the aforedescribed process almost repeats identically but with a remarkable difference: the trailing edge vortex is generated slightly more downstream than

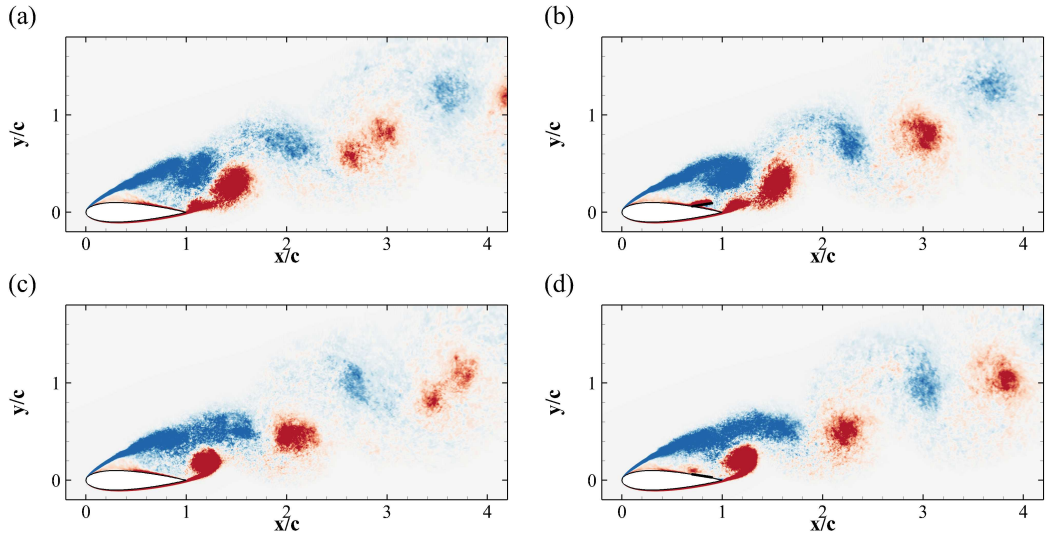

FIGURE 4.22: Contours of the conditional averaged spanwise component of vorticity ω_z, for the case with (b, d) and without (a, c) flap. Blue negative vorticity (i.e., clockwise), red positive ($\pm 5U_\infty/c$). The top and bottom rows correspond to the times of maximum and minimum lift, respectively.

the previous one, thus allowing the new lifting vortex to expand more than its predecessor (see Figure (4.20a) and Figure (4.20f)). The presence of the flaplet alters the previously described sequence. Here, the initial snapshot has been chosen to match the condition in which the flaplet lays on the aerofoil surface (Figure (4.21a)). In this situation, the trailing edge vortex has just been shed, and the lifting vortex is forming. As the flap lifts up (Figure (4.21b-c)) under the action of the pressure gradient induced by the passage of the lift vortex, a new trailing edge vortex is formed while the lifting vortex is shed away. As a consequence, the flap moves downward (Figure (4.21d-e)) under the action of the trailing edge vortex that is forming and subsequently, detaches from the trailing edge. The formation and roll up of the trailing edge vortex is conditioned by the movement of the flap that during its downward rotation generates a jet that pushes the vortex downstream. The displacement of the trailing edge vortex away from the aerofoil at every shedding cycle allows the incoming lifting vortex to grow and develop more freely without the constraint generated by the vicinity of a counter rotating vortex. The detachment of the trailing edge vortex induced by the flap generated jet has also a regularisation effect on the shedding cycle that now repeats identically with no difference between consecutive cycles. As the snapshots indicate, the position of the flap is strongly related with the passage of the lifting vortex. In particular, we have measured a correlation coefficient between the evolution of the lift and the flap position equal to 0.6. These findings are quite similar to the ones observed for the $2D$ laminar flow where the flaplet was regularising the lift/drag cycle with a movement characterised by the

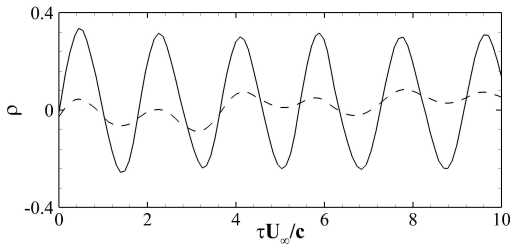

FIGURE 4.23: Time cross correlation ρ of the lift coefficient C_L and spanwise vorticity ω_z at the location $(2.0c; 0.4c)$. Solid and dashed lines are used for the case with and without flap, respectively.

same value of the lift-flap position correlation coefficient.

To gain further insight into the increased regularity of the shedding cycle, we have computed flow field averages conditioned by the value of the lift coefficient (i.e., ensemble averages between samples sharing the same phase in the shedding cycle). In particular, we averaged spanwise vorticity fields corresponding either to the maximum (Figure (4.22a-b)) or to the minimum (Figure (4.22c-d)) lift force for both the cases. For both situations of minimum and maximum lift, it is possible to notice that the positive rollers (red ones, generating downforce) are displaced to the right when the flaplet is used. Moreover, with the flap, the lift generating vortex seems to be more compact in the maximum lift condition. Concerning the wake, the vortex street generated with the flap is more regular with an almost uniform sequencing of the counter rotating vortices. The enhanced regularity of the cycle is also confirmed in Figure (4.23) showing the time cross correlation ρ of the lift coefficient C_L and the spanwise vorticity ω_z at location $(2.0c;\ 0.4c)$ (x coordinate measured from the leading edge, y from the profile chord). The cross correlation ρ is defined as follows

$$\rho(\tau) = \frac{E\left[C_L(t)\,\omega_z(t+\tau)\right]}{\sigma\left[C_L\right]\ \sigma\left[\omega_z\right]}, \tag{4.2}$$

where $E[\,]$ and $\sigma[\,]$ indicate the expected value and the standard deviation, respectively. In the case with flap, the evolution of the time cross correlation shows a clear periodic behaviour with high levels of correlations (0.35). While in the case without flap, the correlation is much lower (0.05).

Finally, as already done in the $2D$ case, to determine which mechanism is the main responsible for the increase in average lift obtained with the flap, we have computed the circulation Γ over two closed surfaces C embedding the lift and the trailing edge vortices, respectively. The former is defined over the region $x \in [0.5, 1.0]$, $y \in [0.3, 0.6]$, the latter covers the area $x \in [0.8, 1.3]$, $y \in [0.0, 0.3]$ (see Figure (4.5)).

Similarly to what we have observed for the $2D$ laminar case, the circulation of the leading edge vortex (the one that generates lift) is only slightly increased

by the flap presence ($\approx 2\%$), while the circulation of the trailing edge vortex (the one that reduces the lift, or increase the downforce) is substantially reduced by a factor of $\approx 15\%$. Therefore, we can draw the same conclusion as the one given for the $2D$ case: the increase in lift promoted by the usage of the flap is mainly due to the reduction of the intensity of the trailing edge vortex, rather than an increase in the circulation of the lifting vortex.

Chapter 5

Control of the flow around an aerofoil in ramp-up motion

5.1 Introduction

The demand for helicopters with increased performance and the quest for efficiency improvements in vertical axis wind turbines have prompted further investigations into the dynamic stall that often appears on rotors retreating blades. Dynamic stall is an unsteady phenomenon that takes place on lifting objects in response to time variations of the angle of attack, and it is responsible for dramatic changes in the aerodynamic loads, high vibration affecting the dynamic performance, and occurrence of aeroelastic instability (stall flutter). A considerable number of researches have extensively studied these phenomena in the past [38, 63, 64, 67, 68, 17]. Experimental works have mainly focused on unsteady flows over two-dimensional aerofoils undergoing prescribed pitching motions [38, 28, 29, 30, 31, 63, 64, 57, 67, 68]. McCroskey [63, 64] discovered that the stall is characterised by a lift overshoot, due to the passage of a large scale vortex over the suction side of the aerofoil, followed by a lift breakdown associated with the vortex detachment, and Shih et al. [87] suggested that the main stall vortex is induced by the early boundary layer separation near the leading-edge of the aerofoil, and that full stall occurs when the boundary layer detaches completely from the aerofoil.

High fidelity numerical simulations of dynamic stall in configuration of aeronautical interest are particularly expensive due to the broad range of time and space scales involved in the phenomenon. However, conventional turbulence models are known to fail in producing reliable solutions in such complex, out of equilibrium conditions: unsteady, recirculating and locally transitional flow. A general, but somehow outdated review on the numerical simulations of dynamic stall [83, 99, 91, 7, 96, 26, 34] can be found in the work of Ekaterinaris and Platzer [27]. Several other works have highlighted the difficulties that RANS calculations

encounter when dealing with dynamic stall. In particular, Wang et al. [96] used two variants of the $k-\omega$ model, the standard and the SST one, to simulate the flow at moderate high Reynolds number $Re_c = 10^5$. From a comparison with experimental results, they noticed that the models can not precisely capture the size and position of the dynamic stall vortex. Moreover, the quality of the predictions of the models deteriorate as the angle of attack increases. Dumlupinar and Murthy [26] further investigated the performances of various turbulence models and pointed out that different turbulence closures predict a broad range of different behaviours even in light stall cases. Recently, Rosti et al. [81] performed a DNS of flow around a NACA0020 aerofoil, with the aim of elucidating the physical mechanisms that determine the dynamic stall vortex creation, its evolution along the aerofoil and the subsequent detachment.

Because of the undesirable aerodynamic and structural consequences of dynamic stall, many researchers have focused on the development of control techniques able to palliate such adverse effects. In this framework, a number of different passive and active control techniques [58, 41, 35, 36] have been proposed in the past. More recently, researchers have been looking at biomimetic devices to control flow separation on aerofoils at high angle of attack. In particular, it has been observed that birds can overcome certain flight critical conditions, by popping up some of their feathers when flow separation starts to develop on the upper side of their wing [10, 12, 21]. It is believed that the feathers lift up may contain backflow thus preventing an abrupt breakdown of aerofoil lift typical of dynamic stall. With the aim of demonstrating the effectiveness of devices mimicking the feathers pop-up, Schatz et al. [84] have shown that a self-activated spanwise flap elastically mounted by the trailing edge of an aerofoil can enhance lift by more than 10% at a chord Reynolds number $Re_c = U_\infty c/\nu$ (U_∞ being the magnitude of the free stream velocity, c the aerofoil chord and ν the kinematic viscosity) in the range of 10^6. In a related experiment, Schluter [85] has also demonstrated that dynamic stall lift-breakdown is less severe when a similar flap is used.

More recently, Bruecker and Weidner [17] used hairy flaps (i.e., flaps with a thickness much smaller than the plant form sizes) to manipulate the dynamic stall of a wing at moderate Reynolds number $Re_c = 77000$, observing a delay of the dynamic stall. The authors claim that the delay is achieved by both the reduction of the backflow, and by regularising of the shear layer roll-up process. Moreover, they suggest that the onset of the shear layer non-linear growth is delayed via mode-locking of the fundamental instability mode with the motion of the flaps. Rosti et al. [80, 82] performed a DNS of the flow around a NACA0020 aerofoil with a flap mounted via a torsional spring on its suction side at a fixed angle of attack 20^o. They found an increase in lift by around 20% when the spring stiffness, geometry and location are properly tuned. Under these conditions, a pulsed jet induced by the flaplet oscillatory movement, that is in turn due to the periodic transit of a large recirculation bubble on the aerofoil suction side,

displaces the trailing edge vortices further downstream, away from the wing. The consequences of this downstream displacement of the trailing edge generated vortices, are: a reduction of the downforce generated by these vortices and a regularisation of the shedding cycle that reveals to be much more ordered in time and space when the flaplet is activated.

5.2 Results and discussions

To introduce the effects produced by the presence of a membrane-like flap hinged on the suction side of an aerofoil, we first briefly summarise some of the results of the baseline flow under consideration, that have been already given in Chapter (3): the flow around a NACA0020 aerofoil undergoing a ramp-up manoeuvre without the application of any control device at a chord Reynolds number fixed to the value of $Re_c = 2 \times 10^4$. In particular, the angle of attack undergoes an initial linear increase from $\alpha = 0$ to $\alpha = 20^o$ with a reduced frequency $k = 0.12U_\infty/c$ followed by a steady value of the angle at $\alpha = 20^o$. The variation of α with time matches the experimental conditions of Brucker and Weidner [17] and is also very similar to the one considered in [68].

5.2.1 Baseline flow description

All the ramp-up simulations are initialized from a fully developed, zero degree angle of attack flow condition. All averaged quantities that will be presented have been obtained employing a double averaging procedure: space averaging in the homogeneous z-direction and ensemble averaging at same time instants obtained from simulations using different initial conditions. In particular, we have considered ten realisations obtained using ten different initial conditions obtained from instantaneous zero degree flow fields sampled within two shedding cycles.

Figure (5.1a) shows the time evolution of the lift and drag coefficients during the ramp-up motion for the baseline configuration without flap (solid lines). Initially, both coefficients increase until reaching their maximum values well after the end of the linear increase of the angle of attack. At about $5tU_\infty/c$, the lift decreases abruptly while the drag starts to diminish at a later time. As it will be described later on, the drop in the force coefficients, is related to the detachment of the dynamic stall vortex from the aerofoil. At a later time, the integral forces oscillate slowly converging towards the asymptotic static-stall values, in agreement with the physical description given by McCroskey [63]. During their time evolution, the maximum values achieved by the lift and drag coefficients are $C_L = 1.58$ and $C_D = 0.67$, respectively. Both these values are about the double of the corresponding coefficients measured in the static case at $\alpha = 20^o$.

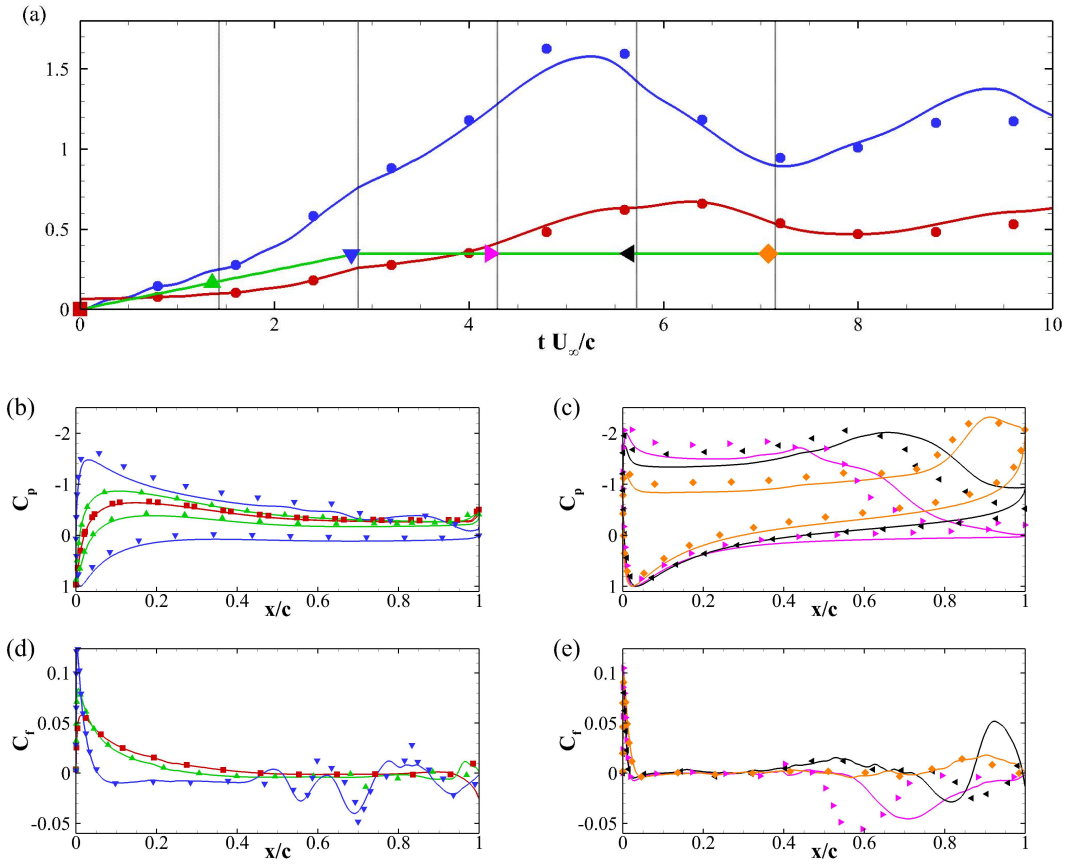

FIGURE 5.1: (a) Lift (blue line) and drag (red line) coefficients as a function of time. The green line is representative of the time variation of the angle of attack. Along this last line, the symbols indicate 6 particular time instants for which integral quantities along the aerofoil are represented in the remaining panels of the figure. In these diagrams, solid continuous lines represent the baseline cases while the symbols are for the cases of the aerofoil equipped with the flap. Also the colours indicate the time level at which the information has been extracted (consistently with the colours of the symbols of the top panel). (b)-(c) Pressure coefficient C_p and (d)-(e) friction coefficient C_f at the selected times.

The other panels of Figure (5.1) show the time evolution of the pressure coefficients C_p (b and c) and of the friction coefficients C_f (d and e). Figure (5.2) displays the contours of the span-wise, z-component of vorticity ω_z, averaged in the homogeneous z-direction at the same six times as the ones considered in Figure (5.1). In particular, the first plot corresponds to the zero degree angle of attack, the second to $\alpha = 10^o$ and the others at various time instants at $\alpha = 20^o$. Figure (5.2a) shows how the flow is mostly symmetric over the aerofoil surface when $\alpha = 0^o$. Consistently, also the C_p distribution appears to be symmetric (Figure (5.1b)), with a plateau starting at about the mid-chord position,

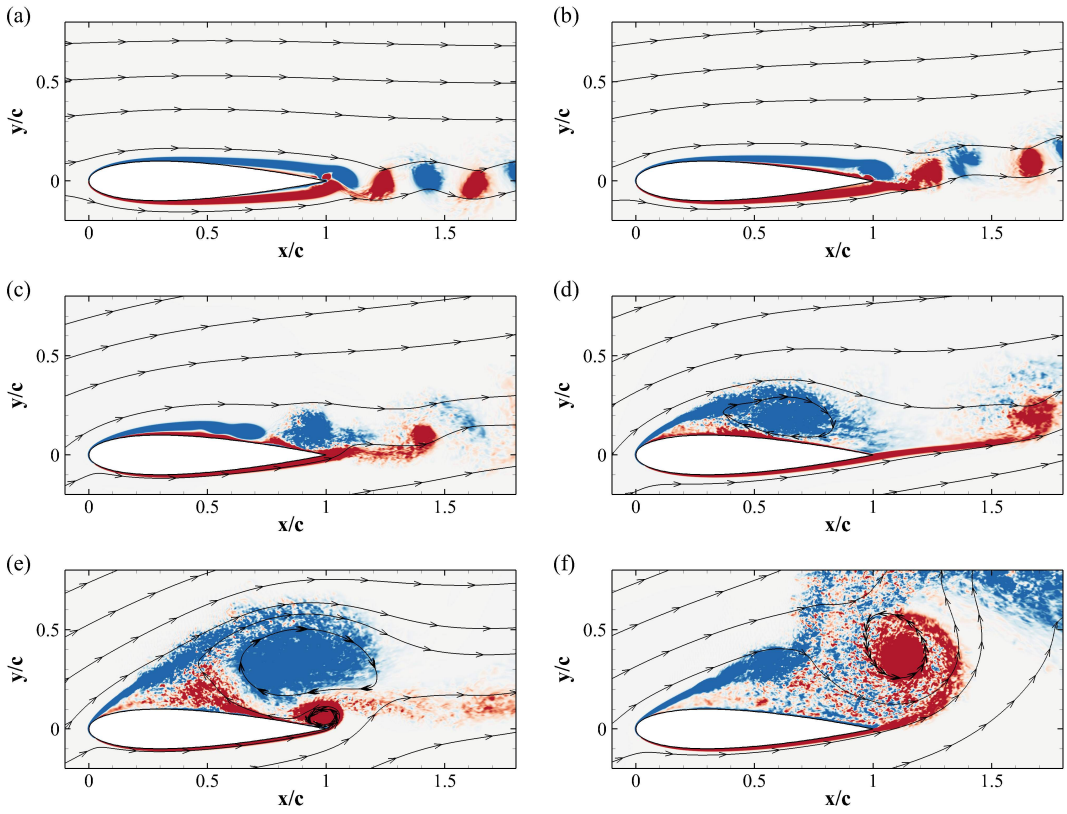

FIGURE 5.2: Contour plots of the space average of the spanwise component of vorticity ω_z of the baseline simulation. The contours plots have been obtained at the times indicated in Figure (5.1a). Blue negative vorticity, red positive ($\pm 7U_\infty/c$).

indicating the presence of a separated region. The presence of the separated flow appears clearly from the friction coefficient distribution (Figure (5.1d)) that presents a peak near the leading edge, followed by a smooth decrease and a separation point at about the mid-chord location. As the angle of attack is increased, the pressure distribution (Figure (5.1b)) and the flow field (Figure (5.2b-c)) loose their symmetry with a consequent lift increase. At increased angles of attack, the maximum friction coefficient and the separation point move towards the leading edge (Figure (5.1d)). Even after having reached the maximum incidence, the lift coefficient keeps increasing (Figure (5.1a)) with a pressure coefficient distribution that does not show the typical separation plateau. As the peak of the pressure near the leading-edge is still increasing, and a second peak appears around the mid-chord (Figure (5.1c)). The latter is the footprint of a large vortex which has started to form on the suction side (i.e., the so called dynamic stall vortex), see Figure (5.2d). It is also noted that until the maximum lift is not reached, no vortices are shed from the trailing edge as can be educed from Figure (5.2d). After its formation, the dynamic stall vortex is convected

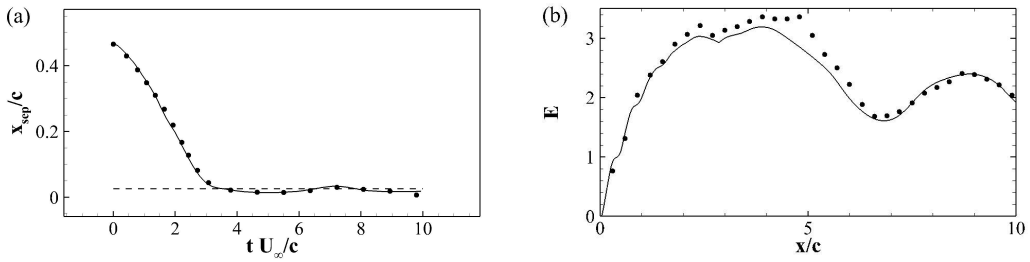

FIGURE 5.3: Time evolutions of the (a) downstream separation point and (b) aerodynamic efficiency $E = C_L/C_D$ during the ramp-up manoeuvre. Solid lines and symbols are used for the baseline and controlled cases, respectively. The dashed line in (a) represents the separation point at 20^o.

downstream towards the trailing edge (as indicated by the displacement of the second pressure peak in Figure (5.1c)), where an induced counter rotating vortex is formed, see Figure (5.2e). When the dynamic stall vortex finally detaches from the aerofoil and the trailing edge vortex reaches its maximum size (Figure (5.2f)), the pressure attains an almost constant distribution indicating a fully separated flow condition (Figure (5.1c)). The complete time evolution of the separation point is reported by the solid line in Figure (5.3a). At $\alpha = 0^o$ the separation point is located at $x_s = 0.47c$, moving towards the leading edge as the angle of attack is increased. As already remarked, the static stall separation point $x_s = 0.025c$ (dashed line) is firstly reached when the ramp-up motion is finalised at $t = 3.5c/U_\infty$. In the subsequent stage, when the incidence angle is constant ($\alpha = 20^o$), the separation line moves further upstream followed by a damped oscillating positioning around its static value.

5.2.2 Hinged flap: parametric study

We now turn our attention to the effects of a membrane-like flap mounted on the suction side of the aerofoil during the same ramp-up motion. As an initial step, we had to identify a design of the flap able to deliver substantial aerodynamic benefits during the manoeuvre. A proper design must keep into account that the flap motion and its effects on the flow field are controlled by various parameters, such as its length, inertia, position, the torsional spring stiffness and its damping factor. In the previous chapter, focusing on stall at fixed angle of attack (at $\alpha = 20^o$), we have carried out a parametric study aimed to identify an optimal control condition defined as the one that delivers the highest lift coefficient C_L while preserving or improving the aerodynamic efficiency $E = C_L/C_D$. For the present study, where the incidence varies with time, we proceed with a similar parametric study but pursuing a different aerodynamic condition. In particular, we define as a desired condition the one that maintains high efficiency during all the manoeuvre, postpones the dynamic stall, i.e., the lift breakdown, and

TABLE 5.1: Flap configurations considered in the parametric study. The aerofoil is NACA0020 and the Reynolds number is $Re_c = 20000$. The flap parameters, i.e., the ratio between the spring natural frequency and the shedding frequency f/f_0, the flap's length L, the hinge position x_F, the spring rotational stiffness K, and the moment of inertia I are provided.

Case	f/f_0	L/c	x_F/c	$K \times 10^3$	$I \times 10^3$
Ref	–	–	–	–	–
F0.25-L0.10-X0.7	0.25	0.10	0.7	2.3461	3.3333
F0.50-L0.10-X0.7	0.50	0.10	0.7	9.3847	3.3333
F1.00-L0.10-X0.7	1.00	0.10	0.7	37.539	3.3333
F2.00-L0.10-X0.7	2.00	0.10	0.7	150.15	3.3333
F4.00-L0.10-X0.7	4.00	0.10	0.7	600.62	3.3333
F0.25-L0.20-X0.7	0.25	0.20	0.7	9.3847	13.333
F0.50-L0.20-X0.7	0.50	0.20	0.7	37.539	13.333
F1.00-L0.20-X0.7	1.00	0.20	0.7	150.15	13.333
F2.00-L0.20-X0.7	2.00	0.20	0.7	600.62	13.333
F4.00-L0.20-X0.7	4.00	0.20	0.7	2402.5	13.333
F0.25-L0.30-X0.7	0.25	0.30	0.7	21.115	30.000
F0.50-L0.30-X0.7	0.50	0.30	0.7	84.462	30.000
F1.00-L0.30-X0.7	1.00	0.30	0.7	337.85	30.000
F2.00-L0.30-X0.7	2.00	0.30	0.7	1351.4	30.000
F4.00-L0.30-X0.7	4.00	0.30	0.7	5405.6	30.000

reduces the subsequent degradation rate of the lift coefficient. Table (5.1) details all the flap configurations that have been considered. In particular, apart from the baseline case without flap, we have analysed flap lengths in the range $L/c = 0.1 - 0.3$, and spring stiffnesses in the range $K = 0.037 - 0.600$. Note that the spring stiffness can be related to the natural frequency of the flap as $K = I\,(2\pi f)^2$, where I is the moment of inertia with respect to the rotation axis given by $I = mL^2/3$, (m being the mass per unit spanwise length). The chosen stiffness values correspond to flap natural frequencies ranging between the half and the double of the shedding frequency of the baseline foil at the maximum angle of attack achieved in the ramp-up motion, i.e., $f_0 = 0.58U_\infty/c$ at $\alpha = 20^o$. In the previous chapter (see also [80] and [82]), we have also analysed both the effects of the flap hinge position, and of a different configuration consisting of two flaps positioned in tandem on the suction side of the aerofoil. The effect of these parameters has not been considered in this study, since it was found that the aerodynamic performances were not very sensitive to their introduction. Having considered all the cases reported in Table (5.1), we have found that the best performance is achieved when using a flap $0.1c$ long, resonating with the shedding frequency of the uncontrolled aerofoil at an incidence of $\alpha = 20^o$. A summary of the time evolution of the lift coefficients during the ramp-up manoeuvre obtained using various flap configurations is reported in Figure (5.4) (note that, only the lift breakdown phase is shown in the figure).

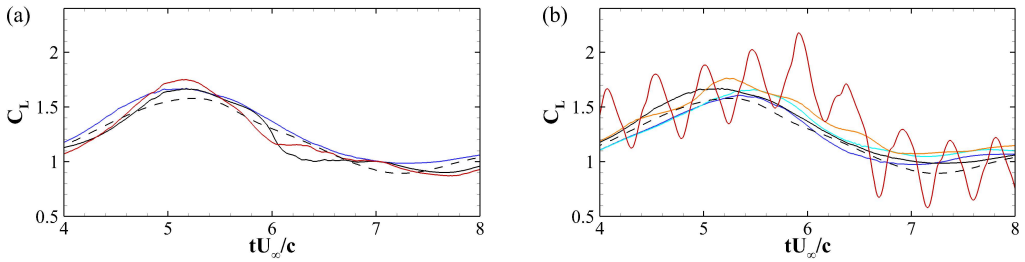

FIGURE 5.4: Evolution of the lift C_L for some of the cases considered in the parametric study. In panel (a), the length of the flap is varied, while keeping the flap natural frequency equal to the foil shedding frequency. The blue, black and red lines are used to identify the lift coefficients obtained with flap lengths equal to $L = 0.1c$, $0.2c$ and $0.3c$, respectively. In panel (b) we consider cases where the length of the flap is frozen to $L = 0.1c$, and the natural frequency of the flap is changed; the blue, light blue, black, orange and red lines are used for $f = 0.25f_0$, $0.5f_0$, $1.0f_0$, $2.0f_0$ and $4.0f_0$, respectively (f_0 being the shedding frequency of the baseline foil at 20^o incidence). The dashed line is used to indicate the reference cases.

5.2.3 Flow around the foil equipped with the selected flap

In this section we will be focusing on the aerodynamic performances and on the flow field generated around a NACA0020 aerofoil equipped with a zero thickness flap mounted on its suction side during the ramp-up motion under consideration. The chosen flap configuration corresponds to the one delivering the best performances as determined via the parametric campaign described in the previous section: flap length $0.1c$, hinged at $0.7c$, infinitely long in the spanwise direction, and with a torsional stiffness adjusted to produce a flap natural frequency matching f_0 (the shedding frequency of the baseline profile at 20^o incidence). For convenience, in what follows the aerofoil equipped with the aforementioned, quasi-optimal flap will be simply termed either as the *controlled aerofoil*, or the *aerofoil with the flap*. A comparison of the time evolution of the lift and drag coefficients of the baseline aerofoil (continuous line) versus the controlled one (dotted line) during the ramp-up motion is displayed in Figure (5.1). From the diagram, it appears that the drag coefficient C_D is only slightly influenced by the presence of the flap, while the lift coefficient C_L is increased during the initial $7tU_\infty/c$ time units, thus indicating an overall increase in aerodynamic efficiency E during the ramp-up motion. Figure (5.3b) reports the time variations of the aerodynamic efficiency E (defined as the ratio between the lift and drag coefficients, i.e., $E = C_L/C_D$). The graph shows how the controlled case presents higher values of the efficiency than the baseline one during the whole manoeuvre, with a maximum which is approximately 10% higher than in the uncontrolled case. From the figure, it also appears that higher efficiency is also maintained during the whole lift breakdown phase. Moreover, in the most critical condition, the minimum lift coefficient at the end of the lift breakdown is sensibly higher

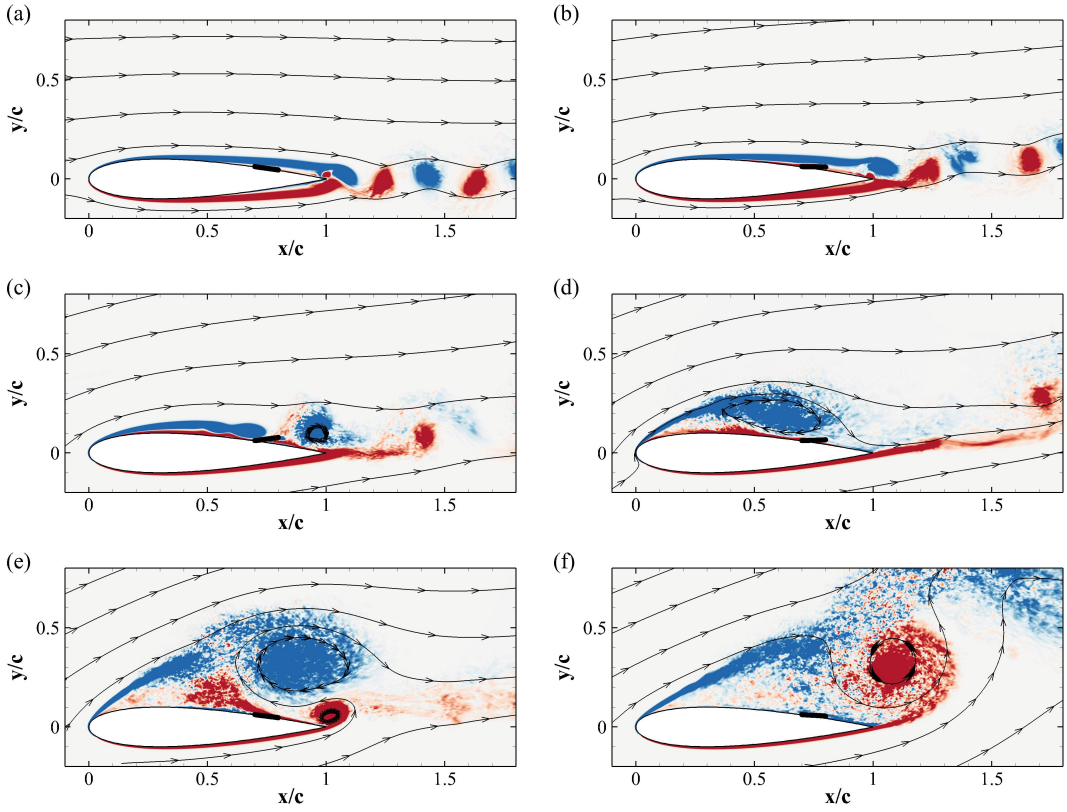

FIGURE 5.5: Contour plots of the space average of the spanwise component of vorticity ω_z for the controlled case with flap, sampled at the times given in Figure (5.1a). Blue negative vorticity, red positive ($\pm 7U_\infty/c$).

(about 12%) in the controlled case than in the uncontrolled one (i.e., with flap: $C_L^{min} = 1.0$; baseline case: $C_L^{min} = 0.89$). Thus, when the flap is used, a less severe lift deficit following the dynamic stall overshoot delivers a smoother aerodynamic response to the unsteady change of incidence. The milder aerodynamic response induced by the presence of the flap is also enhanced by the extended time interval over which the lift decreases after the first lift maximum: in the controlled case this period of time is extended by 5% as compared to the baseline case.

Figure (5.5) shows the flow evolution during the ramp-up manoeuvre in terms of spatial averaged spanwise vorticity when the flap is in use. The selected snapshots and vorticity levels correspond to the ones of the baseline case illustrated in Figure (5.2). Initially, at $\alpha = 0^o$, the flow is mostly attached to the aerofoil, and the flaplet lies tangentially on the aerofoil surface (Figure (5.5a)). As the angle of attack is increased and the separation point moves upstream (Figure (5.5b-c)), the flap starts to lift reducing the backflow advancing from the trailing edge. Within this stage, the pressure coefficient C_p (Figure (5.1b)) of the controlled

case shows a higher leading edge pressure peak. It is also noted that the presence of the flap postpones the C_f oscillations (see Figure (5.1d)). In the following stage, when the dynamic stall vortex is forming and maximum lift is almost reached (Figure (5.5c-e)), the flap reverses his movement, now directing towards the wing surface. The flap downward motion generates a jet that displaces the forming trailing edge vortex downstream. This flap-flow interaction process delays the detachment of the dynamic stall vortex, resulting in a higher maximum lift value (maximum value in the controlled case: $C_L^{max} = 1.68$), and in a milder lift breakdown. A footprint of the same process can also be observed in the C_p and C_f distributions in Figure (5.1c,e) that show how the second pressure peak and the friction oscillations due the movement of the dynamic stall vortex occur at a chord location closer to the leading edge. Differently from the previous magnitudes, the time displacement of the mean separation point over the suction side, shown in Figure (5.3a), is only slightly altered by the presence of the flap.

When describing Figure (5.1d-e), we have already highlighted the presence of some oscillations in the C_f distribution by the trailing edge region. These oscillations amplify in time thus affecting larger portions of the foil. The physical mechanism responsible for these oscillations is a shear layer instability of Kelvin-Helmholtz type that originates from the trailing edge and propagates upstream in time. The time-space propagation of this instability is analysed in Figure (5.6a) that shows the evolution over time of the fluctuations of the stream-wise velocity component at various x locations at a wall normal distance of $0.1c$ above the aerofoil suction side. The red and blue curves are used for the baseline and controlled cases, respectively. The symbols in the same figure indicate the time when the amplitude of the fluctuation reaches 2.5% of the averaged streamwise velocity value. In this diagram it is clear that in the baseline case initially the x-wise velocity fluctuations are confined to the trailing edge region and that only after 2 time units the fluctuations reach the half chord location. At a later stage, the fluctuations travel slowly further upstream, but never contaminating the leading edge portion of the aerofoil. This behaviour proves that in the baseline case, during the ramp-up motion, the separated region travels upstream from the trailing edge. When the flap is considered, the situation is quite different. In this case, the locations upstream of the flap hinge are reached by the perturbations with a slight time delay, while the the fluctuations downstream of the hinge are strongly reduced in amplitude and postponed in time. Table (5.2) confirms the aforementioned effect of the flap in reducing the velocity fluctuations in the rear part of the aerofoil (by approximately 10%) while leaving the intensity of the fluctuations almost unchanged in the front part.

Figure (5.6b) and Table (5.2) also illustrate the behaviour of the pressure fluctuations that further highlights the difference between the two cases with a maximum reduction of pressure rms of about 25% at 80% of the chord.

Further insight into the physical processes taking place during the ramp-up motion can be gained by analysing the time emergence of coherent structures,

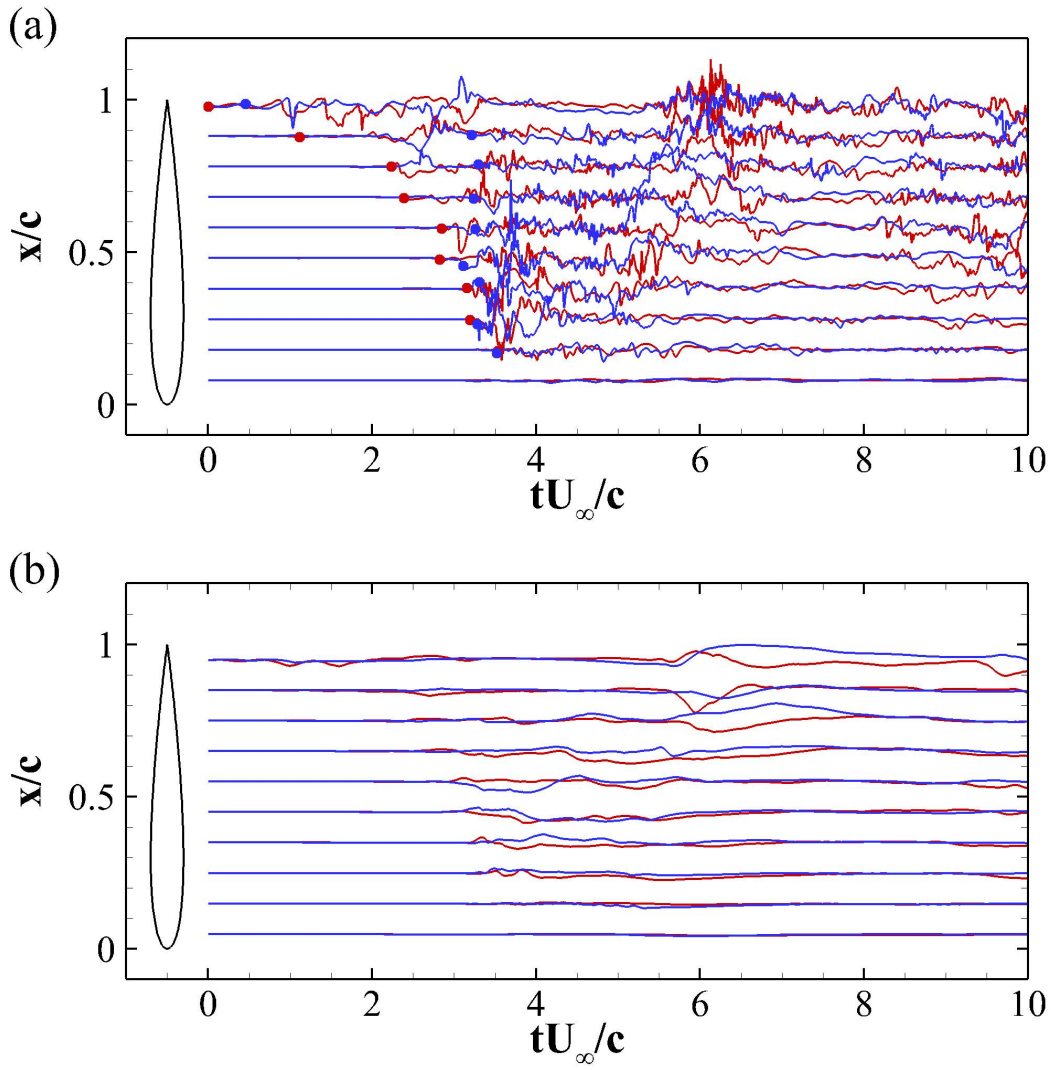

FIGURE 5.6: Fluctuations of the (a) x-velocity components u' and (b) pressure p as a function of time for various points near the aerofoil surface. For clarity, the fluctuations are shifted according to the chord location where they were measured. Red lines are for the baseline case, blue lines are for the aerofoil with the flap. For further explanations see the text

their mutual interactions and the generation of the wake. In particular, vortical coherent structures have been identified using the $\mathcal{Q}$-criterion. Instantaneous $\mathcal{Q}$ iso-surfaces are shown in Figure (5.7). The left column corresponds to the baseline profile, while the right one presents the case of the aerofoil with the flap. The rows in the figure have been captured at the same time after the beginning of the ramp-up motion. Panels in the first row (a and b) correspond to the earliest stages at $t = 1.45c/U_\infty$, when the angle of attack is $\alpha = 10^o$. The flow is very similar in the two cases presenting a slight asymmetry, with coherent structures

TABLE 5.2: Percentage variations of the r.m.s. values of the streamwise velocity component and pressure fluctuations in the aerofoil with flap with respect to the baseline foil. The locations x/c are the same as the ones Figure (5.6)

x/c	0.1	0.2	0.3	0.4	0.5	0.6	0.7	0.8	0.9	1.0
$u'\%$	0	0	-1	-1	-1	-6	-10	-10	-12	-8
$p'\%$	3	2	2	1	0	-5	-15	-25	-21	-20

generated only past the trailing edge area of the suction side. At $\alpha = 20^o$ (panels c and d), the shear layer rolls-up into a recirculating region that closes at about the mid-chord location. However, the size and intensity of the large roller is strongly reduced when the flap is in use. Moreover in the controlled case, the whole shear layer instability and the consequent roll-up appear to be shifted downstream indicating a time delay in the whole instability process. The next panels (e, f and g and h) show how the roll-up process continues to develop leading to the formation of a very large recirculating zone (i.e., the dynamic stall vortex) that basically covers all the foil suction side. Again, the recirculating region and its intensity seem to be diminished by the action of the flap that also delays the process in time. In the same panels, it is also possible to observe the presence of a trailing edge vortex that interacts with the dynamic stall vortex inducing an upward displacement of the latter. As compared to the baseline case, in the controlled case, the trailing edge vortex is also displaced downstream. When the trailing edge vortex is shed, the leading edge shear layer starts to roll-up again forming a new vortex (see panels i and j). The whole process is then cyclically repeated in time with the intensity of the fluctuations slowly damped out to reach asymptotically the final stationary stalled condition.

A further analysis that allows to better understand the unsteady vortex formation, the associated transport processes and the origin of the instabilities arising in the flow is based on the study of the evolution of the Finite-Time Lyapunov Exponents (FTLE). Figure (5.8) shows contours of the FTLE during a time period equal to the one considered in Figure (5.1). The frames are organised chronologically, with the left and right columns corresponding to the baseline and controlled cases, respectively. Starting from $t = 1.45c/U_\infty$, the snapshots have been extracted at the same time instants as the ones marked in Figure (5.1). In panels a and b, the corresponding flow field is slightly asymmetric with two shear layers originating from the mid-chord region. The next two panels (b and c), show how the flow on the pressure side of the foil tends to reattach, while on the suction side an early separation is visible. Also, the shear layer at the trailing edge starts to roll up. As the shear layer roll-up process continues, a recirculation region is progressively built up on the foil suction side (see panel e and f), ultimately leading to the formation of a large scale vortical structure, i.e., the dynamic stall

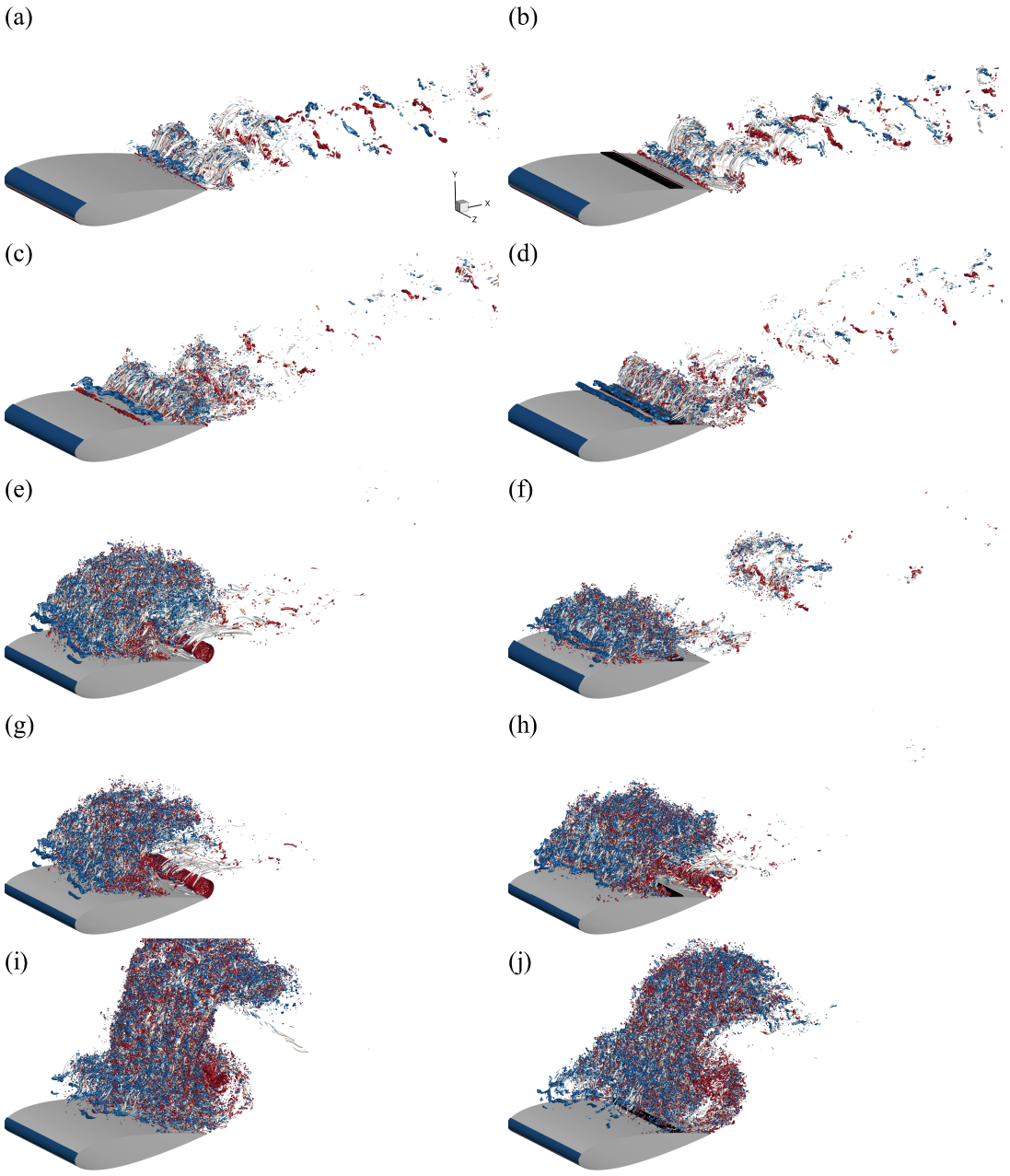

FIGURE 5.7: Visualisation of instantaneous vorticity field by means of $\mathcal{Q}$-iso-surfaces ($\mathcal{Q} = 500U_\infty^2/c^2$ for a-f a,d and $\mathcal{Q} = 1000U_\infty^2/c^2$ for g-j) coloured by the instantaneous spanwise component of the vorticity $\omega_z = \pm 40$ (red positive, blue negative). The left and right columns are used for the baseline and controlled cases, respectively.

vortex. As already remarked when analysing Figure (5.7), the sequence of panels a-c-e and b-d-f show again that the action of the flap retards the roll up of the shear layers. It is also highlighted that, while the large scale, dynamic stall vor-

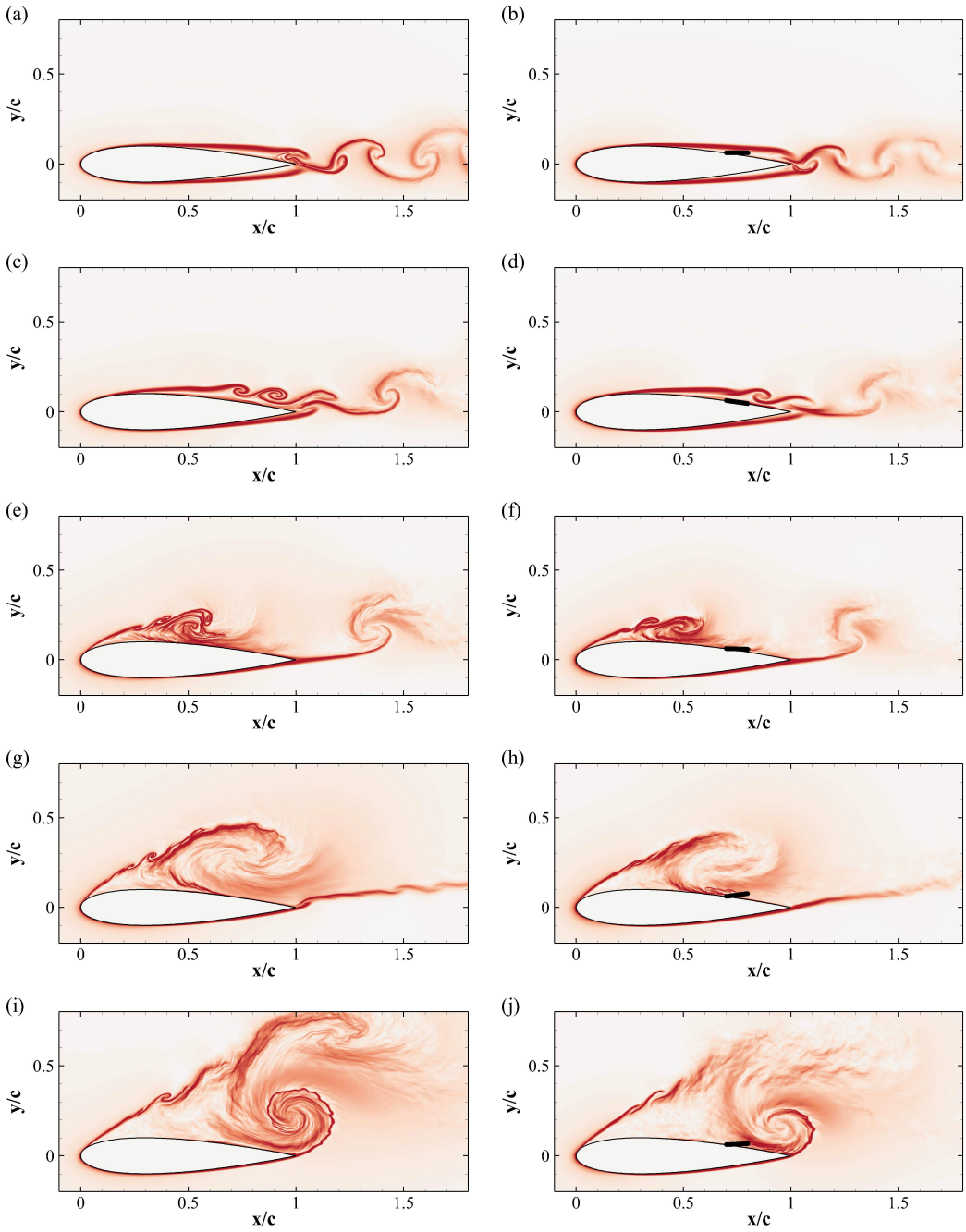

FIGURE 5.8: Contour plot of the FTLE σ^T. Time increases from top to bottom, with a sampling time interval of $\Delta t = 1.45c/U_\infty$. The initial time (a-b) corresponds to $\alpha = 10^o$. The contour levels go from 0 (white) to $7U_\infty/c$ (red). The left and right columns are used for the baseline and controlled cases, respectively.

tex is formed, no vortices are shed from the trailing edge and an almost stable straight shear layer develops from it. The last two panels (i and j) show how

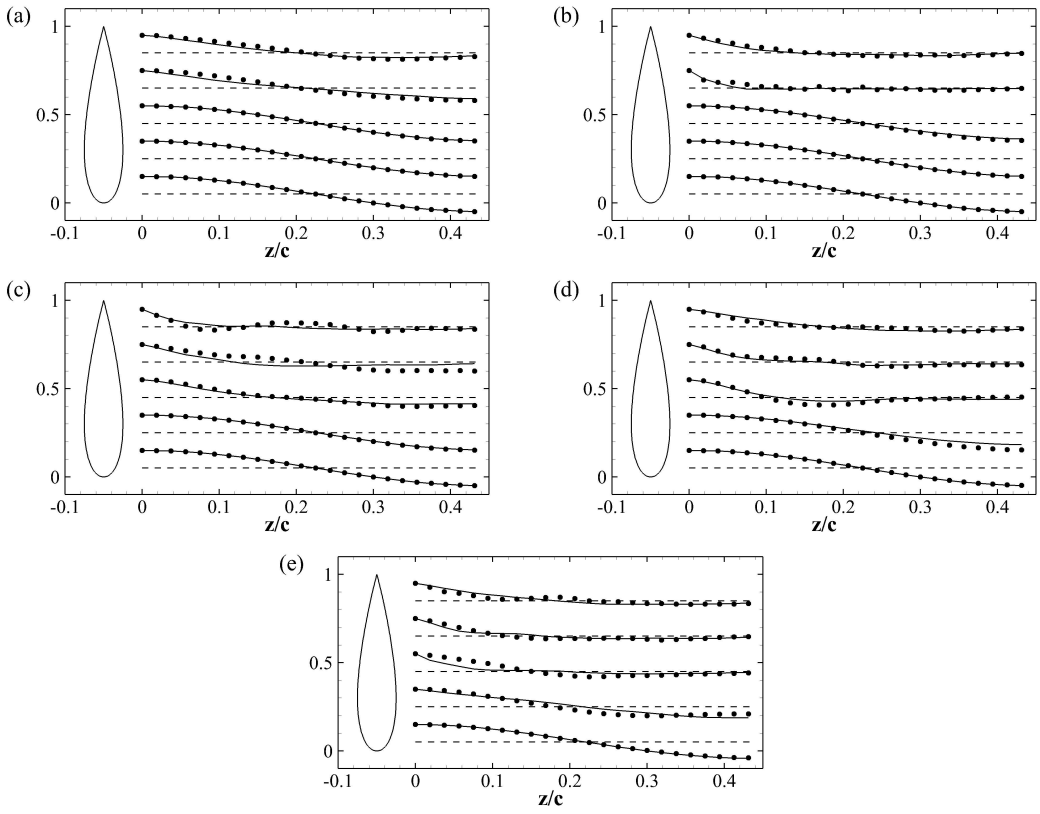

FIGURE 5.9: Spanwise pressure autocorrelation at various locations along the aerofoil suction side, computed at a distance of $0.1c$ from the wall. Time snapshots correspond to the ones given in Figure (5.1a). Solid line is the baseline case while symbols are for the case with flap.

the trailing edge shear layer rolls-up forming a fresh trailing edge vortex which pushes the dynamic stall vortex upwards causing its detachment. From panel j it also appears that the action of the flap strongly delays the formation of the trailing edge vortex.

Finally, we analyse the spanwise two-point pressure autocorrelation R_{pp} at various xy coordinates. The autocorrelation is defined as

$$R_{pp}(z,r) = \frac{\overline{p'(z)p'(z+r)}}{\overline{p'^2(z)}}, \tag{5.1}$$

where the bar denotes the double average over time and along the homogeneous direction z. The pressure autocorrelation snapshots shown in Figure (5.9) have been extracted at the same time instants as those shown in Figure (5.1) that, in turn, correspond to the panels of Figure (5.7) and Figure (5.8). All the represented values have been obtained at a distance of $0.1c$ from the wall. In the first panel of Figure (5.9), the flow is mostly attached to the aerofoil, and all the

points are in the laminar region. A wake induced, low amplitude pressure wave (amplitude $\sim 0.3\%$ of the mean value) is visible at all the selected locations in panels a and b. In panel a, the controlled case shows the same behaviour except at the trailing edge, where the correlation reaches higher negative values. A more clear difference between the two cases is visible in panel b, that corresponds to the moment in which the angle of attack has reached 20^o, and the separation point has moved upstream as shown in Figure (5.3a). In the baseline case the correlation rapidly goes to zero for all the points in the rear part of the aerofoil, indicating transition to turbulence. Differently, the case with flap maintains higher values of the autocorrelation function in all the region covered by the flap motion. In later stages (panels c and d), when the trailing edge vortex is starting to roll up, the baseline case takes on a higher value of the correlation function (see Figure (5.7e)). The lower value in the controlled case is due to the action of the flap that delays the formation of the trailing edge vortex. Finally in panel e, most of the correlation values are quite low, except in the region spanned by the flap motion (in the controlled case), where the correlation seems to grow again because of the coherent local flow motion induced by the flap movement.

Chapter 6

Conclusions

We have carried out a number of direct numerical simulations of the flow around a NACA 0020 aerofoil at a chord Reynolds number of $Re_c = 20000$, subject to variations of the incidence angle. After describing and validating the numerical approach with results from the literature, the flow around the aerofoil has been simulated in both a static stall condition at 20^o and during a ramp-up manoeuvre leading to a a dynamic stall condition (i.e., the angle of attack varying linearly from 0^o to 20^o at a non-dimensional rate of $\dot{\alpha}_{\mathrm{rad}} = 0.12U_\infty/c$).

In the static stall case, the mean flow is dominated by a large recirculation zone present on the whole suction side, with a secondary smaller recirculation bubble located in correspondence of the aerofoil maximum thickness. The instantaneous behaviour highlights the presence of a shear layer formed at the leading edge that undergoes a convective Kelvin-Helmholtz instability. On the other hand, while from the trailing edge the separated flow rolls-up and generates a large vortex which has a blocking effect on structures originated at the leading edge. Behind the aerofoil a large wake is formed, mainly due to flow separation at the trailing edge of the aerofoil, and with a smaller contribution from the shear layer formed at the leading edge. The different contributions of these two regions are responsible for the wake lack of symmetry. The breaking of the symmetry also manifests when considering the spectra of the time autocorrelation of the velocity computed in the leading edge shear layer and near the trailing edge. Both the spectra show a clear peak corresponding to the principal wake shedding frequency, while only the leading edge spectrum shows a smooth peak at higher frequency, corresponding to the vortex generation induced by the Kelvin-Helmholtz shear layer instability. Also, in the same spectrum, a low frequency peak appears at approximately half the shedding frequency. This peak corresponds to the flapping motion of the shear layer.

In the ramp-up case, the lift force initially increases monotonically in time even after having attained the maximum incidence angle. Subsequently, it drops dramatically eventually converging towards the static stall values. During the linear growth of the angle of incidence, the separation point moves from the trail-

ing edge towards the leading edge. The backward displacement of the separation line is associated with the formation of a large scale vortex on the suction side of the aerofoil. The unsteady evolution of this vortex, usually termed as dynamic stall vortex, is ultimately responsible for time variations of the aerodynamic force coefficients. As the separation line moves upstream along the suction side, vortices generate, merge and eventually coalesce into one large dynamic stall vortex. This mechanism is mainly driven by the Kelvin-Helmholtz instability generated at the leading edge. Indeed, the convective KH instability associated with the leading edge generated shear layer, continuously produce fine grain vorticity that merges generating spanwise oriented large scale structures.

The second part of the thesis work has focused on the use of passive, self actuated flaps to be used as lift enhancement devices in nominally stalled conditions. The main objective was to discover how the mutual interaction between these self deployable devices and the unsteady flow field generated by a foil at high angle of attack can improve the aerodynamic efficiency of stalled wings. Although the design of optimal flaps (i.e., delivering maximum lift increase) was not a primary objective of this work, we had to carry out a preliminary selection study to determine the characteristics (i.e., size, location and natural frequency) of a self-adaptive flaplet able to deliver substantial aerodynamic benefits in a stalled condition. This initial study has been conducted on a baseline NACA0020 aerofoil at 20^o degrees angle of attack at low (fully laminar) chord Reynolds number (i.e., $Re_c = 2 \times 10^3$). The impact on the aerodynamic performance of a rigid, thin flap hinged with a torsional spring on the aerofoil suction side has been analysed via a parametric study involving the size of the flap, the hinge location and the spring stiffness. It has been found that, in order to obtain effective flow manipulations, it is of fundamental importance to lock-in the flap oscillation frequency with the foil Strouhal number. When operating in resonating conditions, the aerodynamic forces become quite sensitive to the geometric properties of the flap. In particular, optimal performances (i.e., $\approx 20\%$ increase in lift) are achieved with a flap length of one fifth of the chord hinged at about 70% of the aerofoil. Once the geometric and physical characteristics of an aerodynamically efficient flaplet have been determined, we turned our attention to the understanding of the flow-flap interaction mechanisms responsible for the improved foil performances at high angle of attack. To this end, we have carried out Direct Numerical Simulations of the flow past a NACA0020 aerofoil at 20^o angle of attack at a chord Reynolds number of 2×10^4 considering both the baseline wing and the wing equipped with the optimal flaplet as determined in the $2D$ parametric campaign. Initially, considering the baseline wing, it has been observed the main flow mechanisms taking place in the fully three-dimensional scenario, involving a laminar separation, a subsequent reattachment and a laminar-turbulent transition, determine a flow behaviour that is qualitatively similar to the two dimensional case used for the preliminary design study. The reasons for this similarity are related with the common laminar separation, and the convective inviscid instability of the leading

edge shear layer responsible for the roll up of the large recirculation bubble on the aerofoil. In a second phase, we have systematically compared the flow fields generated with and without the flap. Although the mean velocity fields and the mean kinetic energy are very similar, the optimal flaplet has a very strong impact in manipulating the unsteady character of the vorticity field. In particular, the flap is popped up by the passage of the lift vortex and when relaxing back to the equilibrium position generates a jet almost tangent to the wing surface, directed towards the trailing edge. This jet detaches the vortex street generated by the trailing edge shear layer instability away from the aerofoil. The displacement of the trailing edge vortices has a twofold effect. On one hand, there is a net decrease in the downforce that is directly generated by these vortices leading to a global increase of the lift. On the other hand, the displacement of the trailing edge vortex allow for a complete evolution of the leading edge generated vortex that now does not interact directly with the trailing edge vortices. As a consequence, the periodic character of the wake is now mainly controlled by the shedding of the leading edge vorticity into the wake. The decoupling of the two main vorticity layers regularises the shedding cycle also promoting a much more ordered wake topology.

In the final stage of the present thesis, we have considered the use of a similar flaplet as a control device able to mitigate the severe consequences of dynamic stall. In particular, we have considered the same NACA0020 aerofoil undergoing a ramp-up manoeuvre (i.e., incidence angle α initially increasing linearly from 0^o to 20^o with a reduced frequency of $0.12U_\infty/c$, followed by a plateau at $\alpha = 20^o$) at a chord Reynolds number of 2×10^4. After having conducted a detailed analysis of the baseline flow without flap, a number of different flap configurations have been considered having set as an aerodynamic objective one that: *i)* postpones the dynamic stall, *ii)* reduces the subsequent lift coefficient degradation rate and *iii)* delivers a high efficiency throughout the whole manoeuvre. Similarly to the static case, we have considered a family of rigid, membrane-like flaps hinged at the same location on the foil suction side (i.e., 70% of the chord) via a torsional spring. Each different flap configuration, obtained by modifying the flap natural frequency (i.e., spring stiffness) and its length, has been evaluated in terms of the aforementioned criteria. Finally, it has been found that a flap measuring 10% of the chord (thus shorter than the optimal flap found for the static case), with a natural frequency matching the shedding frequency of the baseline foil at $\alpha = 20^o$ (in steady stalled conditions) delivers the best performances in term of the desired aerodynamic objectives. To better understand some light on the physical mechanisms that improve the time evolution of the lift coefficient during the ramp-up motion, we have also systematically analysed the flow topology and its variations when the flap interacts with the flow field. It has been observed that already from the beginning of the linear increase of the incidence angle, the presence of the flap appears to delay the whole dynamic stall process. In particular, its action retards the initial roll up process associated with the vorticity

generated by the shear layer instability originating at the leading edge. This delay is also accompanied by a decreases of the generated dynamic stall vortex intensity. The passage of this dominant vortex, lifts up the flap partially inhibiting the interaction between the vortex advected along the suction side of the foil and the trailing edge shear layer that also appears to be stabilised by the flap action. The final flap downward motion also contributes to delay and to diminish the intensity of the trailing edge vortex. The described stages constitute a cycle that repeats in time slowly reducing in intensity until the transient is completed and the steady angle of attack cyclic condition is recovered.

This thesis has probably just scratched the surface of a novel methodologies for flow control based on adaptive but passive control devices. These devices can achieve profound fluid dynamic modifications taking advantage of fluid-structure interaction processes. Techniques based on wide range of compliant elements, ranging from elastic flaps to dense poro-elastic carpets can open new horizons in the manipulation of different time and length scales of a flow field. Those manipulations can target a number of objectives not only related with wing aerodynamics. Enhanced mass and heat transfer, skin friction drag reduction and energy harvesting are just few examples of the potential applications of technologies based on a smart exploitation of fluid-structure interaction.

Appendix A

Pitching aerofoil

In this section, we present an ongoing research that extends the investigation carried out for the ramp-up manoeuvre to pitching cases. Research on pitching aerofoils is a crucial need in wind turbines aerodynamics and in rotorcraft dynamics. Even though an exhaustive study of this manouvre goes beyond the scope of the thesis, we have decided to include some preliminary results, because obtained in the same generated context of the present thesis. In particular, we have started by considering the flow around a NACA0020 aerofoil undergoing a pitching motion at a chord Reynolds number fixed to the value of $Re_c = 2 \times 10^4$. The angle of attack is varied sinusoidally around $\alpha_0 = 0^o$, with a maximum angle of $\alpha_A = 20^o$, at reduced frequency of $k = \pi f U_\infty / c = 0.27$ (the angle of attack grows from 0^o to 20^o in the same time interval as the ramp-up simulations presented in the previous chapters)

$$\alpha(t) = \alpha_0 + \alpha_A \sin(2\pi f t). \tag{A.1}$$

The simulation is initialized from a fully developed, zero degree angle of attack flow condition. All averaged quantities that will be presented have been obtained employing a double averaging procedure: space averaging in the homogeneous z-direction and phase averaging. The phase average covers ten cycles, after three initial transient cycles that have been discarded. The simulation was still undergoing at the time this section has been written.

Figure (A.1a) shows the time evolution of the lift and drag coefficients during the pitching motion. Initially, while the angle of attack is increased, both coefficients increase, and their maximum values are reached when the angle is already decreasing. After half cycle the angle of attack is null again, then the drag starts to increase again, while the lift coefficient becomes negative and has the same behaviour of the first half cycle but with negative values. As it will be described later on, the increase and drop in the force coefficients, are related to the formation and detachment of the dynamic stall vortex from the aerofoil, in agreement with the physical description given by McCroskey [63]. During their time evolution, the maximum values achieved by the lift and drag coefficients are

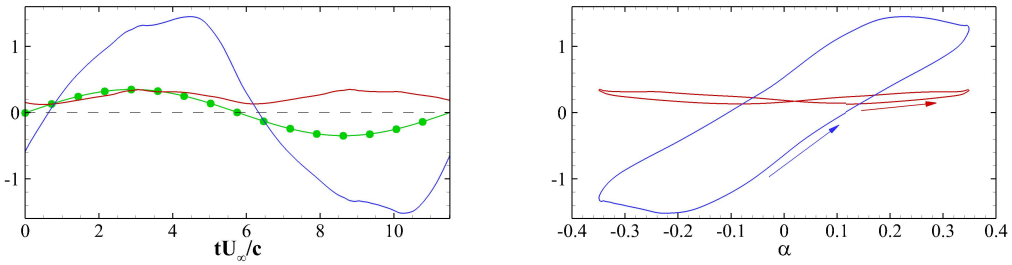

FIGURE A.1: Lift (blue line) and drag (red line) coefficients as a function of (a) time and (b) angle of attack. The green line in (a) is representative of the time variation of the angle of attack. Along this last line, the symbols indicate 16 particular time instants for which integral quantities along the aerofoil are represented in the other figures.

$C_L = 1.45$ and $C_D = 0.34$, respectively. Note that, when the angle of attack is equal to zero, the lift and drag coefficients have different values depending on the phase. This is due to the hysteresis cycle, clearly shown in Figure (A.1b), where the force coefficients are shown as a function of the angle of attack.

Figure (A.2) and Figure (A.3) display the contours of the span-wise, component of vorticity ω_z, averaged in the homogeneous z-direction at the same sixteen times as the ones considered in Figure (A.1). In particular, the first plot corresponds to the zero degree phase, the second to $\phi = 22.5^o$ and so on. Figure (A.2a) shows how the flow is not completely symmetric over the aerofoil surface when $\phi = 0^o$, as already noted. Indeed, during the upstroke the separation point is on the suction side of the aerofoil, and the wake is tilted upward. As the phase angle is increased, the flow fields (Figure (A.2b-d)) completely loose their symmetry with a consequent lift increase, and the separation point keeps moving towards the leading edge. A large vortex has started to form on the suction side (i.e., the so called dynamic stall vortex), as the result of the roll-up process of smaller scale vortices (Figure (A.2b)). It is also noted that, until the maximum lift is not reached, no vortices are shed from the trailing edge as can be educed from Figure (A.2d). After its formation, the dynamic stall vortex is convected downstream towards the trailing edge, where an induced counter rotating vortex is formed, see Figure (A.2e), when the downstroke motion has just started, but the lift is still growing. When the dynamic stall vortex finally detaches from the aerofoil and the trailing edge vortex reaches its maximum size (Figure (A.2f)), a fully separated flow condition is reached, and the lift coefficient finally decreases. As the phase angle approaches 0^o again (Figure (A.2g-h)), the dynamic and trailing edge vortices are convected downstream, and the separation point moves downstream towards the trailing edge. From the phase $\phi = 180^o$ onwards, shown in Figure (A.3), the same process is repeated with the pressure and suction side inverted.

A more detatiled analysis and the effects that an elastically mounted flap can

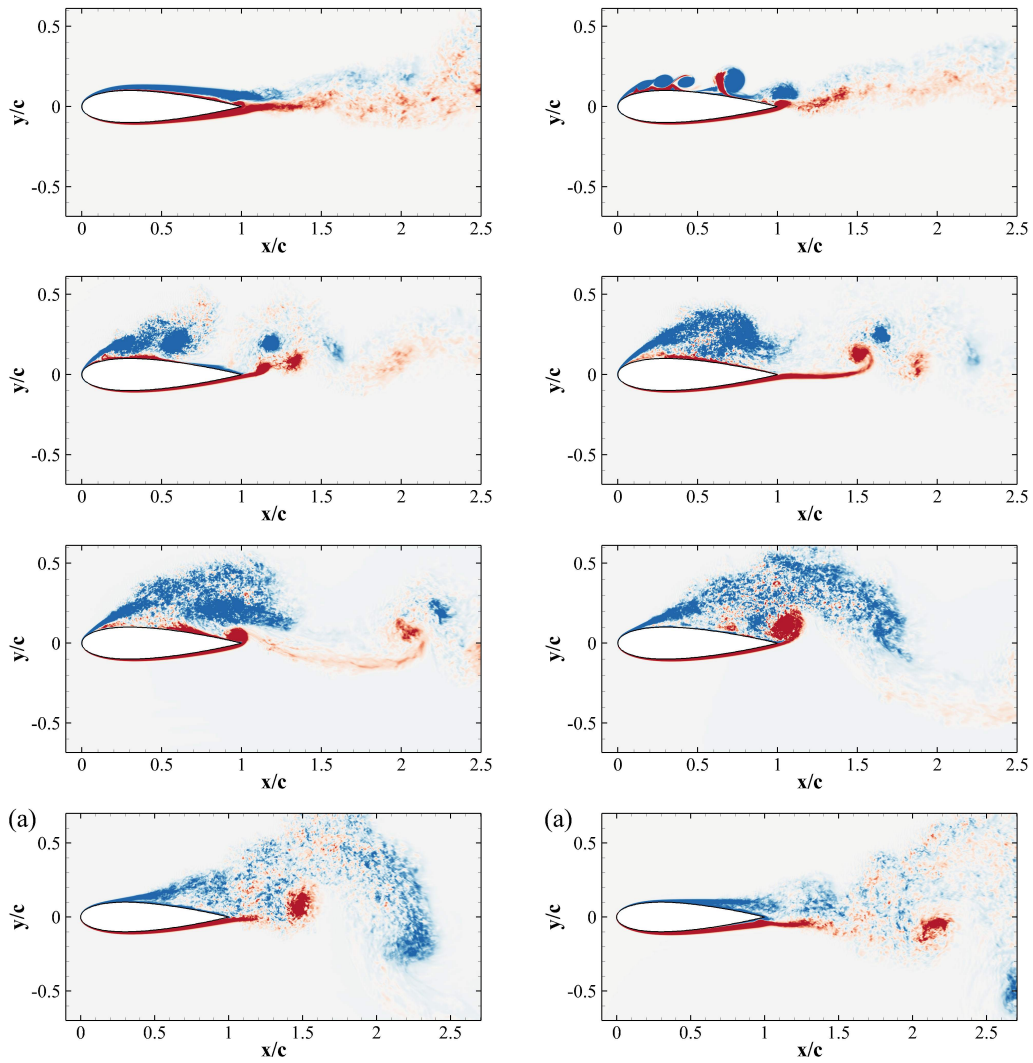

FIGURE A.2: Contour plots of the space and phase average of the spanwise component of vorticity ω_z, sampled at the times given in Figure (A.1). Blue negative vorticity, red positive ($\pm 7U_\infty/c$).

have on the unsteady flow field will be the subjects of future publications.

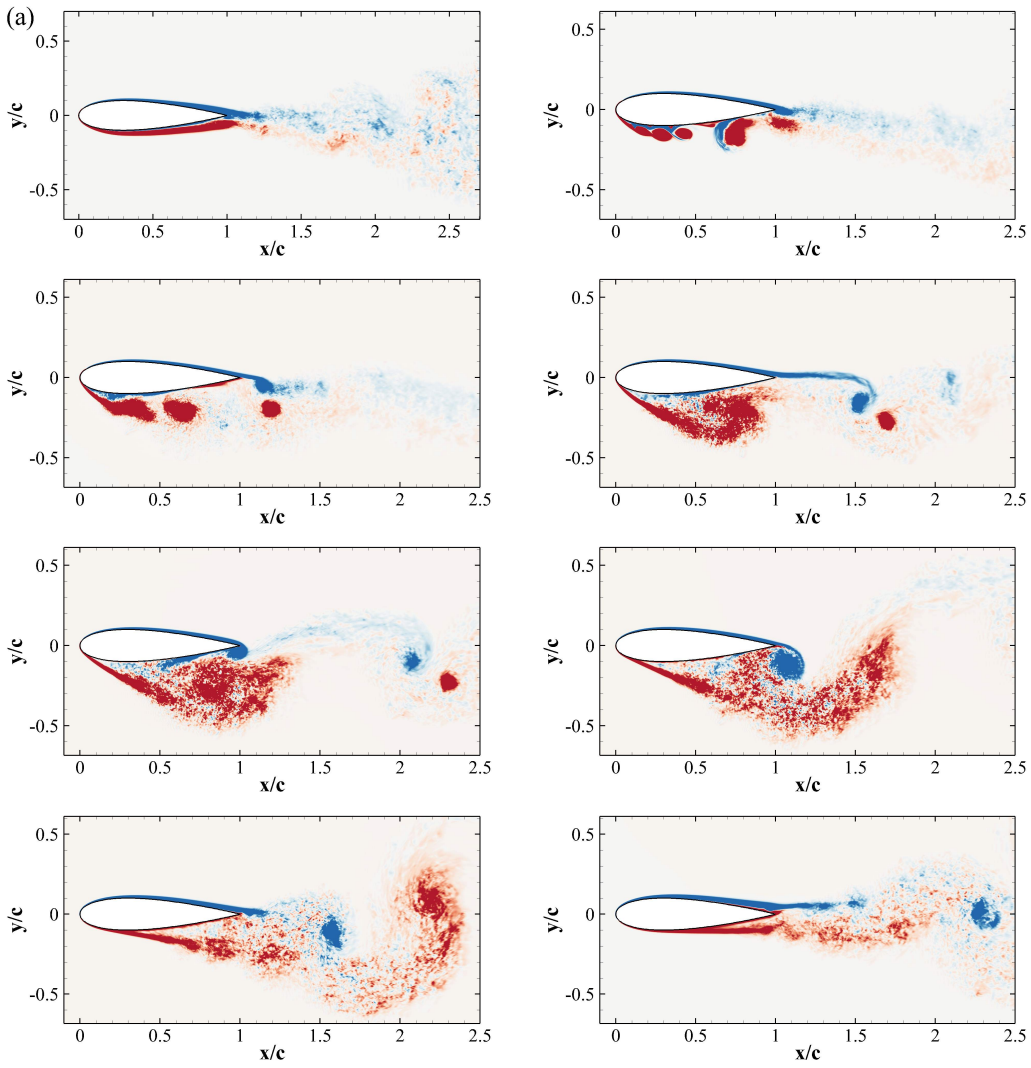

FIGURE A.3: Same as Figure (A.2)

Bibliography

[1] I E Abdalla and Z Yang. Numerical study of the instability mechanism in transitional separating–reattaching flow. *International Journal of Heat and Fluid Flow*, 25(4):593–605, 2004.

[2] M Acharya and M H Metwally. Unsteady pressure field and vorticity production over a pitching airfoil. *AIAA Journal*, 30(2):403–411, 1992.

[3] M A Aldheeb, W Asrar, E Sulaeman, and A A Omar. A review on aerodynamics of non-flapping bird wings. *Journal of Aerospace Technology and Management*, 8(1):7–17, 2016.

[4] A Altman and G Allemand. Post-stall performance improvement through bio-inspired passive covert feathers. In *54th AIAA Aerospace Sciences Meeting*, page 2042, 2016.

[5] S Bagheri, A Mazzino, and A Bottaro. Spontaneous symmetry breaking of a hinged flapping filament generates lift. *Physical Review Letters*, 109(15):154502, 2012.

[6] S Balay, S Abhyankar, M Adams, J Brown, P Brune, K Buschelman, L Dalcin, V Eijkhout, W Gropp, D Kaushik, M Knepley, L C McInnes, K Rupp, B Smith, S Zampini, and H Zhang. PETSc Web page, 2015. http://www.mcs.anl.gov/petsc.

[7] G N Barakos and D Drikakis. Computational study of unsteady turbulent flows around oscillating and ramping aerofoils. *International Journal for Numerical Methods in Fluids*, 42(2):163–186, 2003.

[8] D W Bechert, M Bruse, W Hage, and R Meyer. Biological surfaces and their technological application—laboratory and flight experiments on drag reduction and separation control. *AIAA Paper*, 1960, 1997.

[9] D W Bechert, W Hage, and R Meyer. Self-actuating flaps on bird-and aircraft-wings. *Flow Phenomena in Nature: Inspiration, Learning and Applications 2 (design and nature)*, pages 435–446, 2006.

[10] DW Bechert, M Bruse, W Hage, and R Meyer. Fluid mechanics of biological surfaces and their technological application. *Naturwissenschaften*, 87(4):157–171, 2000.

[11] K Böhmer, P W Hemker, and H J Stetter. The defect correction approach. In *Defect correction methods*, pages 1–32. Springer, 1984.

[12] G Bramesfeld and M D Maughmer. Experimental investigation of self-actuating, upper-surface, high-lift-enhancing effectors. *Journal of Aircraft*, 39(1):120–124, 2002.

[13] M Breuer and N Jovicic. An les investigation of the separated flow past an airfoil at high angle of attack. In *Direct and Large-Eddy Simulation IV*, pages 165–172. Springer, 2001.

[14] M Breuer and N Jovicic. Separated flow around a flat plate at high incidence: an les investigation. *J. Turbul*, 2(1):N18, 2001.

[15] A P Broeren and M B Bragg. Low-frequency flowfield unsteadiness during airfoil stall and the influence of stall type. *AIAA Paper*, 2517:15–18, 1998.

[16] C Bruecker. Interaction of near-wall turbulence with flexible hairs. *Journal of Physics: Condensed Matter*, 23:18–29, 2011.

[17] C Bruecker and C Weidner. Influence of self-adaptive hairy flaps on the stall delay of an airfoil in ramp-up motion. *Journal of Fluids and Structures*, 47:31–40, 2014.

[18] S Burgmann, J Dannemann, and W Schröder. Time-resolved and volumetric piv measurements of a transitional separation bubble on an sd7003 airfoil. *Experiments in Fluids*, 44(4):609–622, 2008.

[19] S Burgmann and W Schröder. Investigation of the vortex induced unsteadiness of a separation bubble via time-resolved and scanning piv measurements. *Experiments in Fluids*, 45(4):675–691, 2008.

[20] C Canuto, M Y Hussaini, A M Quarteroni, and T A Zang. *Spectral methods in fluid dynamics*. Springer Science & Business Media, 2012.

[21] A C Carruthers, A L R Thomas, and G K Taylor. Automatic aeroelastic devices in the wings of a steppe eagle aquila nipalensis. *Journal of Experimental Biology*, 210(23):4136–4149, 2007.

[22] I P Castro and A Haque. The structure of a turbulent shear layer bounding a separation region. *Journal of Fluid Mechanics*, 179:439–468, 1987.

[23] N J Cherry, R Hillier, and M E M P Latour. The unsteady structure of two-dimensional separated-and-reattaching flows. *Journal of Wind Engineering and Industrial Aerodynamics*, 11(1):95–105, 1983.

[24] H Choi, H Park, W Sagong, and S Lee. Biomimetic flow control based on morphological features of living creaturesa). *Physics of Fluids (1994-present)*, 24(12):121302, 2012.

[25] A J Chorin. Numerical solution of the Navier-Stokes equations. *Mathematics of Computation*, 22(104):745–762, 1968.

[26] E Dumlupinar and V R Murthy. Investigation of dynamic stall of airfoils and wings by cfd. In *29th AIAA Applied Aerodynamics Conference*, pages 27–30. Curran, 2011.

[27] J A Ekaterinaris and M F Platzer. Computational prediction of airfoil dynamic stall. *Progress in Aerospace Sciences*, 33(11):759–846, 1998.

[28] L E Ericsson and J P Reding. Fluid dynamics of unsteady separated flow. part i. bodies of revolution. *Progress in Aerospace Sciences*, 23(1):1–84, 1986.

[29] L E Ericsson and J P Reding. Fluid dynamics of unsteady separated flow. part ii. lifting surfaces. *Progress in Aerospace Sciences*, 24(4):249–356, 1987.

[30] L E Ericsson and J P Reding. Fluid mechanics of dynamic stall part i. unsteady flow concepts. *Journal of Fluids and Structures*, 2(1):1–33, 1988.

[31] L E Ericsson and J P Reding. Fluid mechanics of dynamic stall part ii. prediction of full scale characteristics. *Journal of Fluids and Structures*, 2(2):113–143, 1988.

[32] J Favier, A Dauptain, D Basso, and A Bottaro. Passive separation control using a self-adaptive hairy coating. *Journal of Fluid Mechanics*, 627:451–483, 2009.

[33] J H Ferziger and M Peric. *Computational methods for fluid dynamics*. Springer Science & Business Media, 2012.

[34] K Gharali and D A Johnson. Dynamic stall simulation of a pitching airfoil under unsteady freestream velocity. *Journal of Fluids and Structures*, 42:228–244, 2013.

[35] D Greenblatt and I Wygnanski. Dynamic stall control by periodic excitation, part 1: Naca 0015 parametric study. *Journal of Aircraft*, 38(3):430–438, 2001.

[36] D Greenblatt and I Wygnanski. Effect of leading-edge curvature and slot geometry on dynamic stall control. *AIAA Paper*, 3271:2002, 2002.

[37] E Guilmineau and P Queutey. A numerical simulation of vortex shedding from an oscillating circular cylinder. *Journal of Fluids and Structures*, 16(6):773–794, 2002.

[38] R L Halfman, H C Johnson, and S M Haley. Evaluation of high-angle-of-attack aerodynamic-derivative data and stall-flutter prediction techniques. Technical report, DTIC Document, 1951.

[39] G Haller. Distinguished material surfaces and coherent structures in three-dimensional fluid flows. *Physica D: Nonlinear Phenomena*, 149(4):248–277, 2001.

[40] G Haller. Lagrangian structures and the rate of strain in a partition of two-dimensional turbulence. *Physics of Fluids (1994-present)*, 13(11):3365–3385, 2001.

[41] B Heine, K Mulleners, G Joubert, and M Raffel. Dynamic stall control by passive disturbance generators. *AIAA Journal*, 51(9):2086–2097, 2013.

[42] V E Henson and U M Yang. Boomeramg: a parallel algebraic multigrid solver and preconditioner. *Applied Numerical Mathematics*, 41(1):155–177, 2002.

[43] J L Hess and A M O Smith. Calculation of potential flow about arbitrary bodies. *Progress in Aerospace Sciences*, 8:1–138, 1967.

[44] L M Hudy, A M Naguib, and W M Humphreys Jr. Wall-pressure-array measurements beneath a separating/reattaching flow region. *Physics of Fluids (1994-present)*, 15(3):706–717, 2003.

[45] J C R Hunt, A A Wray, and P Moin. Eddies, stream, and convergence zones in turbulent flows. *Center for Turbulence Research Report CTR-S88*, pages 193–208, 1988.

[46] J Johnston and A Gopalarathnam. Investigation of a bio-inspired lift-enhancing effector on a 2d airfoil. *Bioinspiration & Biomimetics*, 7(3):036003, 2012.

[47] J M Johnston, A Gopalarathnam, and J Edward. *Experimental investigation of bio-inspired high lift effectors on a 2-D airfoil*. North Carolina State University, 2011.

[48] B M Jones et al. An experimental study of the stalling of wings. *Aeronautical Research Committee Reports and Memoranda*, 1588, 1933.

[49] L Kamps, F Hegner, D Hess, and C Bruecker. Volumetric velocimetry study in a transitional wall jet flow with passive flow control via flaps. In *International Symposium on Applications of Laser Techniques to Fluid Mechanics*, 2014.

[50] K H Kernstine, C J Moore, A Cutler, and R Mittal. Initial characterization of self-activated movable flaps,"pop-up feathers". *AIAA Paper*, 369, 2008.

[51] S Kida and H Miura. Identification and analysis of vortical structures. *European Journal of Mechanics-B/Fluids*, 17(4):471–488, 1998.

[52] J Kim and P Moin. Application of a fractional-step method to incompressible Navier-Stokes equations. *Journal of Computational Physics*, 59(2):308–323, 1985.

[53] J Kim, P Moin, and R Moser. Turbulence statistics in fully developed channel flow at low reynolds number. *Journal of Fluid Mechanics*, 177:133–166, 1987.

[54] M Kiya and K Sasaki. Structure of a turbulent separation bubble. *Journal of Fluid Mechanics*, 137:83–113, 1983.

[55] C W Knisely. Strouhal numbers of rectangular cylinders at incidence: a review and new data. *Journal of Fluids and Structures*, 4(4):371–393, 1990.

[56] S Kunze and C Bruecker. Control of vortex shedding on a circular cylinder using self-adaptive hairy-flaps. *Comptes Rendus Mécanique*, 340(1):41–56, 2012.

[57] T Lee and P Gerontakos. Investigation of flow over an oscillating airfoil. *Journal of Fluid Mechanics*, 512:313–341, 2004.

[58] T Lee and P Gerontakos. Dynamic stall flow control via a trailing-edge flap. *AIAA Journal*, 44(3):469–480, 2006.

[59] O Lehmkuhl, A Baez, I Rodríguez, and C D Perez-Segarra. Direct numerical simulation and large-eddy simulations of the turbulent flow around a naca-0012 airfoil. In *7th International Conference on Computational Heat and Mass Transfer*, pages 1–8. Begell House, 2011.

[60] T Liu, J Montefort, and S Pantula. Effects of flexible fin on low-frequency oscillation in post-stalled flows. *AIAA Journal*, 48(6):1235–1247, 2010.

[61] W K Liu, Y Chen, R A Uras, and C T Chang. Generalized multiple scale reproducing kernel particle methods. *Computer Methods in Applied Mechanics and Engineering*, 139(1):91–157, 1996.

[62] W K Liu, S Jun, and Y F Zhang. Reproducing kernel particle methods. *International Journal for Numerical Methods in Fluids*, 20(8-9):1081–1106, 1995.

[63] W J McCroskey. The phenomenon of dynamic stall. Technical report, DTIC Document, 1981.

[64] W J McCroskey. Unsteady airfoils. *Annual Review of Fluid Mechanics*, 14(1):285–311, 1982.

[65] G B Mccullough and D E Gault. Examples of three representative types of airfoil-section stall at low speed. 1951.

[66] J Montefort, N Pohl, T Liu, J Gregory, and J Crafton. Thin-wing vibration control using flexible fins. *AIAA Journal*, 51(9):2218–2230, 2013.

[67] K Mulleners and M Raffel. The onset of dynamic stall revisited. *Experiments in Fluids*, 52(3):779–793, 2012.

[68] K Mulleners and M Raffel. Dynamic stall development. *Experiments in Fluids*, 54(2):1–9, 2013.

[69] S Muzaferija. *Adaptive Finite Volume method for flow prediction using unstructured meshes and multigrid approach*. PhD thesis, University of London UK, 1994.

[70] M Omidyeganeh and U Piomelli. Large-eddy simulation of two-dimensional dunes in a steady, unidirectional flow. *Journal of Turbulence*, (12):N42, 2011.

[71] M Omidyeganeh and U Piomelli. Large-eddy simulation of three-dimensional dunes in a steady, unidirectional flow. Part 1. Turbulence statistics. *Journal of Fluid Mechanics*, 721:454–483, 2013.

[72] M Omidyeganeh and U Piomelli. Large-eddy simulation of three-dimensional dunes in a steady, unidirectional flow. Part 2. Flow structures. *Journal of Fluid Mechanics*, 734:509–534, 2013.

[73] C S Peskin. Flow patterns around heart valves: a numerical method. *Journal of Computational Physics*, 10(2):252–271, 1972.

[74] A Pinelli, I Z Naqavi, U Piomelli, and J Favier. Immersed-boundary methods for general finite-difference and finite-volume Navier–Stokes solvers. *Journal of Computational Physics*, 229(24):9073–9091, 2010.

[75] POINTWISE Web page. http://www.pointwise.com/.

[76] B Ponitz, A Schmitz, D Fischer, Ht Bleckmann, and C Bruecker. Diving-flight aerodynamics of a peregrine falcon (falco peregrinus). *PLoS ONE 9(2): e86506*, 2014.

[77] C M Rhie and W L Chow. Numerical study of the turbulent flow past an airfoil with trailing edge separation. *AIAA Journal*, 21(11):1525–1532, 1983.

[78] I Rodríguez, O Lehmkuhl, R Borrell, and A Oliva. Direct numerical simulation of a naca0012 in full stall. *International Journal of Heat and Fluid Flow*, 43:194–203, 2013.

[79] A M Roma, C S Peskin, and M J Berger. An adaptive version of the immersed boundary method. *Journal of Computational Physics*, 153(2):509–534, 1999.

[80] M E Rosti, L Kamps, C Bruecker, M Omidyeganeh, and A Pinelli. The pelskin project - part v - towards the control of the flow around aerofoils at high angle of attack using a self-activated deployable flap. *Meccanica*, under review.

[81] M E Rosti, M Omidyeganeh, and A Pinelli. Direct numerical simulation of the flow around an aerofoil in ramp-up motion. *Physics of Fluids*, 28(2), 2016.

[82] M E Rosti, M Omidyeganeh, and A Pinelli. Passive control of the flow around an aerofoil using a flexible, self adaptive flaplet. *Journal of Fluid Mechanics*, under review.

[83] N L Sankar and W Tang. Numerical solution of unsteady viscous flow past rotor sections. *AIAA Paper*, 85(0129):5, 1985.

[84] M Schatz, T Knacke, F Thiele, R Meyer, W Hage, and D W Bechert. Separation control by self-activated movable flaps. *AIAA Paper*, 1243:2004, 2004.

[85] J U Schluter. Lift enhancement at low reynolds numbers using self-activated movable flaps. *Journal of Aircraft*, 47(1):348–351, 2010.

[86] S C Shadden, F Lekien, and J E Marsden. Definition and properties of lagrangian coherent structures from finite-time lyapunov exponents in two-dimensional aperiodic flows. *Physica D: Nonlinear Phenomena*, 212(3):271–304, 2005.

[87] C Shih, L Lourenco, L Van Dommelen, and A Krothapalli. Unsteady flow past an airfoil pitching at a constant rate. *AIAA Journal*, 30(5):1153–1161, 1992.

[88] A Skillen, A Revell, A Pinelli, U Piomelli, and J Favier. Flow over a wing with leading-edge undulations. *AIAA Journal*, 53(2):464–472, 2014.

[89] P R Spalart and M K Strelets. Mechanisms of transition and heat transfer in a separation bubble. *Journal of Fluid Mechanics*, 403:329–349, 2000.

[90] L W Traub and L Jaybush. Experimental investigation of separation control using upper-surface spoilers. *Journal of Aircraft*, 47(2):714–718, 2010.

[91] I H Tuncer, J C Wu, and C M Wang. Theoretical and numerical studies of oscillating airfoils. *AIAA Journal*, 28(9):1615–1624, 1990.

[92] D Venkataraman and A Bottaro. Numerical modeling of flow control on a symmetric aerofoil via a porous, compliant coating. *Physics of Fluids (1994-present)*, 24(9):093601, 2012.

[93] M R Visbal. High-fidelity simulation of transitional flows past a plunging airfoil. *AIAA Journal*, 47(11):2685–2697, 2009.

[94] M R Visbal. Numerical investigation of deep dynamic stall of a plunging airfoil. *AIAA Journal*, 49(10):2152–2170, 2011.

[95] C H John Wang and J Schluter. Stall control with feathers: Self-activated flaps on finite wings at low reynolds numbers. *Comptes Rendus Mécanique*, 340(1):57–66, 2012.

[96] S Wang, D B Ingham, L Ma, M Pourkashanian, and Z Tao. Numerical investigations on dynamic stall of low reynolds number flow around oscillating airfoils. *Computers & Fluids*, 39(9):1529–1541, 2010.

[97] C H K Williamson. Vortex dynamics in the cylinder wake. *Annual Review of Fluid Mechanics*, 28(1):477–539, 1996.

[98] J G Wong, A Mohebbian, J Kriegseis, and D E Rival. Rapid flow separation for transient inflow conditions versus accelerating bodies: An investigation into their equivalency. *Journal of Fluids and Structures*, 40:257–268, 2013.

[99] J C Wu. *A study of unsteady turbulent flow past airfoils*. PhD thesis, Georgia Institute of Technology, 1988.

[100] Z Yang and P R Voke. Large-eddy simulation of boundary-layer separation and transition at a change of surface curvature. *Journal of Fluid Mechanics*, 439:305–333, 2001.

[101] L Zhang, A Gerstenberger, X Wang, and W K Liu. Immersed finite element method. *Computer Methods in Applied Mechanics and Engineering*, 193(21):2051–2067, 2004.